Design, Modeling and Fabrication of Microhotplate for Gas Sensing Applications

A
Thesis Submitted
in Partial Fulfillment of the Requirements
for the Degree of
DOCTOR OF PHILOSOPHY
By

Gaurav Saxena

Department of Electronics and Electrical Engineering
Indian Institute of Technology Guwahati
August, 2014

Declaration

This is to certify that the thesis entitled "**Design, Modeling and Fabrication of Microhotplate for Gas Sensing Applications**", submitted by me to the *Indian Institute of Technology Guwahati*, for the award of the degree of Doctor of Philosophy, is a bonafide work carried out by me under the supervision of Prof. Roy Paily. The content of this thesis, in full or in parts, have not been submitted to any other University or Institute for the award of any degree or diploma.

Signed: _____

Gaurav Saxena
Department of Electronics and Electrical Engineering,
Indian Institute of Technology Guwahati,
Guwahati-781039, Assam, India.

Date: _____

Dedicated to

अयं निजः परो वेति गणना लघुचेतसाम् ।
उदारचरितानां तु वसुधैव कुटुम्बकम् ।।

My Family

अनतं संसार समुद्रतार
नौकायिताभ्यां गुरुभक्तिदाभ्याम् ।
वैराग्य साम्राज्य पूजनाभ्याम् ।
नमो नमः श्री गुरु पादुकाभ्याम् ।।

My GuruJi's and Gurumata's

शुचित्वं त्यागिता शौर्यं सामान्यं सुखदुःखयोः ।
दाक्षिण्यञ्चानुरञ्जिग्तश्च सत्यता च सुहृद्गुणाः ।।

My Friends

Certificate

This is to certify that the thesis entitled "**Design, Modeling and Fabrication of Microhotplate for Gas Sensing Applications**", submitted by Gaurav Saxena (09610206), a research scholar in the *Department of Electronics and Electrical Engineering*, *Indian Institute of Technology Guwahati*, for the award of the degree of Doctor of Philosophy, is a record of an original research work carried out by him under my supervision and guidance. The thesis has fulfilled all requirements as per the regulations of the institute and in my opinion has reached the standard needed for submission. The results embodied in this thesis have not been submitted to any other University or Institute for the award of any degree or diploma.

Signed: _____

Supervisor: Prof. Roy Paily.
Department of Electronics and Electrical Engineering,
Indian Institute of Technology Guwahati,
Guwahati-781039, Assam, India.

Date: _____

Acknowledgements

"If you haven't failed, you're not trying hard enough."

— *Trust Me on This: Jennifer Crusie*

I could not be at this stage without the support of many wonderful Guru's (family, teachers and friends) in my life. Before I acknowledge anyone else, I, first and foremost acknowledge my parents. Parents are my first Guru's who taught me the basic but powerful life principles. Without them I can't imagine, what I did was possible for me. Next, I deeply acknowledge all who helped me learn and I would like to apologies in advance, if I forget to mention someone.

I would like to thank my PhD supervisor, **Prof. Roy Paily** for his excellent guidance throughout my study. I thank him for his enormous patience and kindness shown to me during our discussions or while evaluating a manuscript. Through his invaluable suggestions, work-ethics, I have learned about the various aspects in the execution and presentation of a research work. I would also like to acknowledge my doctoral committee members **Prof. Pratima Agrawal**, **Prof. Harshal Nemade** and **Dr. K. R. Singh**, for devoting their valuable time and constantly steering my research work in the positive direction.

I was inspired towards the field of research from my first degree itself and I would like to thank many Dr. who have constantly encouraged me through their words and work, **Dr. Gargi Khanna**, my supervisor at National Institute of Technology Hamirpur, **Dr. G Eranna**, **Dr. Ajay Agarwal**, scientists at CEERI Pilani. My seniors at IIT Guwahati, **Dr. N. Ramakrishnan** and **Dr. Dilip Kumar Singh**.

I would like to acknowledge my friends for their unwavering support and confidence in me, Mr. **Himanshu Shekhar Jha**, Mr. **Vijay Kumar**, Thakur **Vijayendra Singh**, Thakur **Dushyant Singh Raghuvanshi**, Mr. **Vijay Shantaram Duryodhan**, Mr. **Yashwant Gangwar**, Mr. **Gyan Chandra**, Mr. **Harihar Shrivastava**. I would especially like to mention my best friend Mr. **Rahul Shrestha**, for his frank and unconditional support. Apart from providing the scholarship for six years, I would like to acknowledge **Government of India** (GOI) for **Indian Nano User Program** (INUP) and **National Program on Micro and Smart Systems** (NPMASS) program.

Lastly, I would like to acknowledge the **Reader** of this page and hopefully thesis, for their patience and good wishes. I have tried to condense the thesis work in limited number of pages so that the reader spend less time reading and more time in exploring this area. I hope this effort will be useful for some.

Sincerely
Gaurav Saxena

Abstract

A microhotplate is comprised of three main components, which are microheater, support platform and insulation layer. Each component directly affects the overall performance of the microhotplate, and designers have control over certain parameters such as type, dimensions or material, which can be used to fine-tune the performance of the system. This thesis aims at the design, modeling and fabrication of microhotplate while improving its efficiency by identifying the various tradeoffs that exist among the performance parameters.

Though some reviews on microhotplates have been reported for a variety of applications, a systematic review, summarizing the progress made in microhotplates design and realization is presented in this thesis. In the review work, suggestion is made regarding the definition of a standard figure of merit (FOM) for obtaining a more accurate microhotplates performance evaluation. The reported figure of merit i.e., Power Per Active Area (PPAA) could include other interlinked performance parameters such as membrane to heater ratio, temperature uniformity, time response etc. Further, FOM could be made more versatile by making it temperature independent, thereby, it can compare the performance of any microhotplate, operating not necessarily at identical temperatures.

Often an insulation layer is deposited over microheater to separate the thermal domain (microhotplate) from its application domains such as gas sensor. Enhancing the performance of microhotplate by the optimization of insulation layer area, especially in terms of power and temperature uniformity aspects, had not been explored yet. The strength of this approach lies in its simplicity and cost effectiveness, as this method will not add any new process step to the existing fabrication steps. An analytical model is developed for the optimization of the insulation nitride area and it is utilized for determining microhotplates temperature profile and power consumption. Moreover, because of the modular nature of the developed model, the thermal losses in the insulation layer could be estimated separately.

In the initial investigation, we utilized silicon nitride insulation layer and with an 8 μm thick nitride layer, a temperature uniformity of $0.18\frac{\mathrm{K}}{\mu\mathrm{m}}$ is achieved. However, deposition time for this thick silicon nitride is large. With the aim of reducing the insulation layer

thickness, we investigated two methods. First method utilizes a material having thermal conductivity higher than silicon nitride. Separate simulation studies are carried out where silicon carbide was employed as insulation layer material. The study reveals that only an 1.5μm thick silicon carbide layer is required to achieve a temperature uniformity of $0.18\frac{\mathrm{K}}{\mu\mathrm{m}}$. Therefore, the deposition time for the whole process will be significantly reduced. Second method use the combination of suitable heater geometry and optimized insulation layer dimensions. Simulation study reveals that this method can reduce the silicon nitride thickness requirement by as much as 50%, i.e., only a 4 μm nitride layer will be required to achieve the targeted temperature uniformity. Whereas, for SiC as insulation layer, the thickness requirement has reduced from 1.5μm to 0.8 μm.

In modeling, it is a common practice to make assumptions regarding the area of membrane. The inaccuracy in membrane area estimations are directly reflected in modeling accuracy. In order to approximate the membrane area more closely, a triangular approach, in which the membrane is divided into 8 symmetrical triangles, is suggested. The membrane area error with triangular approximation is within 0.8% which is better compared to other approximation approaches.

The process steps for the wafer level fabrication of a simple square microhotplate are documented. The fabricated microhotplate was characterized with a simple test setup. With an applied power of 306mW (with 9V), a temperature of 379K is achieved. When the microhotplate is directly probed with higher currents, a temperature >694K is obtained.

Finally, choosing gas sensing as a microhotplate application area, a modeling approach for n-type nanowire transistor based gas sensor has been presented. The model matches closely with the experimentally reported current characteristics of single ZnO nanowire FET.

Contents

List of Figures

List of Tables

1

Introduction

MICROHOTPLATE is an enabling device for a wide variety of sensors or actuators and a microhotplate is comprised of three main components, which are microheater, support platform and insulation layer. Each component directly affects the overall performance of the microhotplate, and designers have control over certain parameters such as type, dimensions or material, which can be used to fine-tune the performance of the system. Microhotplate find their usefulness in application area such as thermal sensors, gas detectors, microscopic thermal infrared emitters, microthrusters, display packaging, micro/nanofludics and microcalorimeters. Fig. 1.1 illustrates, few major microhotplate applications along with their prime performance requirements.

Low power consumption, high temperature uniformity, scalability, quick thermal response, ease of fabrication, reliability and mechanical stability are some of the important

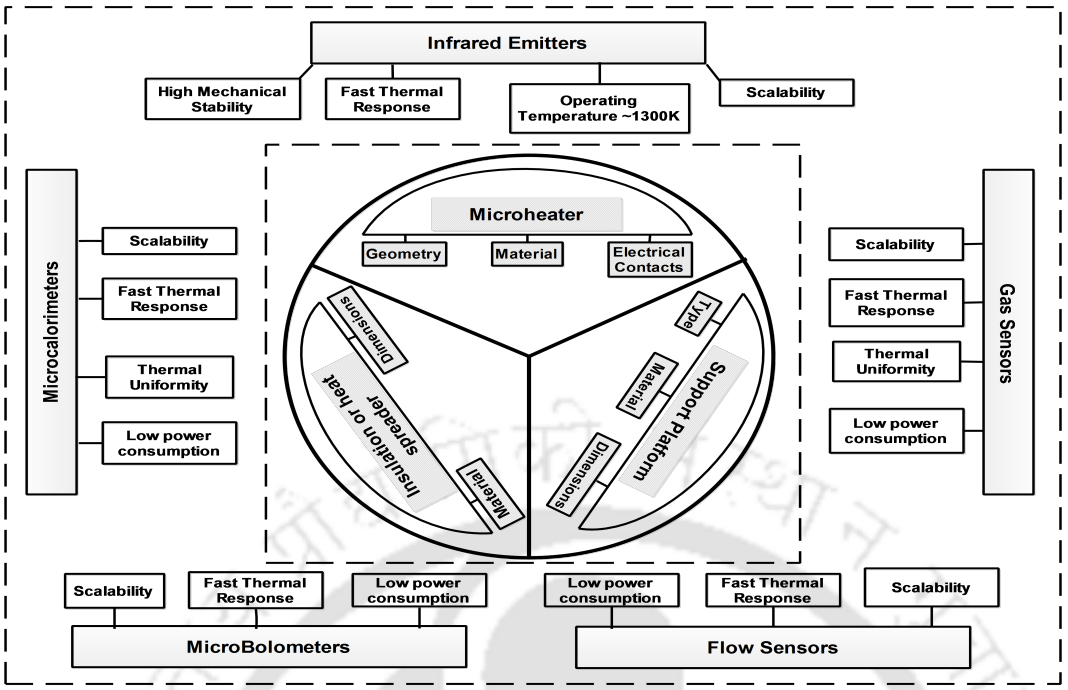

FIGURE 1.1: Few applications where a microhotplate is often employed. Three components of a microhotplate are shown at the center along with their specific design parameters.

characteristics of an efficient microhotplate. Some of these performance parameters will be crucial to a specific application domain. A microhotplate designer is limited with choice of materials and control of their dimensions, and is often confronted with interdependencies among parameters, while evaluating the technological and performance tradeoffs. To illustrate this interdependency, an example could be taken from gas sensing applications which frequently employs microhotplates for improving its response time. The improvement in response time is because, at high temperatures, gas sensors parameters such as adsorption energy and desorption rate decrease, whereas adsorption rate increases, resulting in an improvement in response time [26]. Therefore, response time of the application also depends on the thermal response time of the microhotplates. In addition, an improvement in response time also benefits the pulse mode applications such as Lower Explosive Limit (LEL) sensors and Infrared (IR) sources [16]. The response time of microhotplate can be improved by reducing its thermal resistance. However, a decrease in thermal resistance adversely affects the power consumption of the microhotplate. Therefore, a tradeoff exists between the thermal time response and the power consumption. The other parameters also have a similar interdependencies among them. For example, reliability is also a key feature that needs to be considered in the design

phase of a microhotplate. Gas sensors deployed to perform in harsh environment, like in an automotive industry, are expected to have long life expectancy [9]. The reliability of microhotplate is affected by factors such as thermally induced stress and electromigration effect. Both thermal stress and the electromigration can limit the scalability and the highest achievable temperature of the microhotplates. The electromigration can be dealt by judicial design and material selection with a goal of keeping the current densities under check. The typical values of current densities for electromigration effect to take place in a metals are in the range of 10^5 – $10^7 \frac{\mathrm{A}}{\mathrm{cm}^2}$ [27]. Mechanical stability issue arises because of the thermal stress [28]. This stress causes buckling in the membrane and in turn poses a threat of crack/peel off in the membrane or discontinuity of the microheater geometry. Apart from the microhotplate performance parameters, fabrication cost, technological limitation, material availability/compatibility etc. are other factors which need to be considered during the design phase.

The thesis begins with a systematic review of microhotplate. The review identifies three major component of microhotplate and the designers choices which can be directly related to these components. The review work also briefly covers the various method of modeling and characterization. While reviewing the microhotplate characterization methods, we highlighted the need of a flexible figure of merit and a standard method for timing measurement. In order to design an efficient microhotplate, we have first fine-tuned the performance parameters using simulation studies. These optimized parameters were then utilized while developing analytical models which are further verified with FEM (Finite Element Method) simulations or experimental results. The first simulation study is carried out to identify the contribution of conduction, convection and radiation, individually to the total power losses. This information will help us in choosing a particular loss component while developing subsequent simulation or analytical studies. In an another simulation study, we studied the Membrane to Heater Ratio (MHR), which is an important design parameter. An investigation is carried out to find the optimum MHR value, after considering various tradeoffs. This value is then used consistently throughout the thesis, unless otherwise specified.

While investigating the microhotplate design, it has been found that it is a common practice to blanket deposit an insulation layer. The insulation layer is deposited to provide

the electrical insulation. However, blanket deposition degrades the microhotplate performance. Therefore, an optimized dimensions of insulation layer will not only provide electrical insulation but will also improve other performance parameters, especially thermal uniformity. An analytical model is developed for the quick optimization of insulation layer dimensions. With optimized insulation layer though the uniformity is improved, the thermal response time is affected. We have developed a lumped element model for the transient analysis and it is verified with FEM simulation results. In order to subdue the effect of increased thermal mass, investigation with high-thermal-conductive insulation materials is carried out.

For simplifying the modeling, the membrane area often needs to be approximated. One of such approximation methods includes strip approximation where four rectangular strips of membrane are held accountable for heat losses. In an another method, a square membrane is approximated as circular shape. These approximations either overestimates or underestimates the membrane area and may add inaccuracy to the modeling results. In order to reduce the area approximation error, a triangular approximation approach is developed. The method is validated with experimental and FEM simulation results. Finally, a square microhotplate is fabricated and the detailed process steps of the square microhotplate are documented. A brief discussion on the characterization setup, its validation with simulation and model is also presented.

Gas sensors widely employ microhotplates to improve sensor responses by promoting the chemical reaction between the sensing film and the gas species [29]. Fig. 1.2, shows a typical example of gas sensing device, where a microheater provides the elevated temperature suitable for reaction. The sensing device in Fig. 1.2 consists of a support platform over which a microheater is patterned to provide the local heating, over this microheater, a gas sensitive layer is deposited for sensing purpose. It may be noted that, in order to insulate the microheater and sensing layer an insulation layer is deposited.

As a microhotplate application area we have chosen gas sensors, in which we have identified the various approaches for modeling the gas sensor response and by employing one of them, an analytical model is developed which unifies the effect of gas interaction on

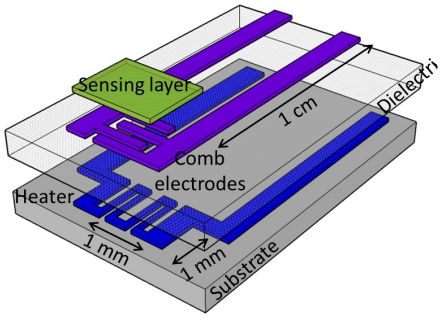

FIGURE 1.2: A gas sensing device using microhotplate. [1]

semiconductor surface to the device electrical response. The developed model is verified with the experimental results reported elsewhere.

1.1 Problem Definition

This thesis aims at the design, modeling and fabrication of microhotplate while improving its performance by identifying the various tradeoffs that exist among the performance parameters. Among the different microhotplate application areas, we have restricted our-self to the gas sensing area and targeted an analytical model for sensor design and performance analysis.

1.2 Major Contributions

A brief description of some major contribution is as follows;

- **Review of microhotplates:** A systematic review of the progress made so far is presented. The three major microhotplate components, its performance parameters and tradeoff among them is identified. In the review work, suggestion is made regarding the definition of a standard figure of merit for obtaining a more accurate microhotplates performance evaluation.

- **Optimized insulation layer area:** We have identified that by optimizing the dimension of an existing layer, one can achieve significant performance improvement. The main advantage of this method lies in it simplicity and cost effectiveness

because of which it does not burden the existing process step. An analytical model is developed for the area optimization and the developed model will also help in reducing the optimization time.

- **Membrane area error reduction:** While developing an analytical model for insulation area optimization, we have identified that the existing methods employed for the area approximation lead to significant area error. A triangular approach is suggested which has considerably reduced the error. The method is verified with the experimental and simulation results.

- **Wafer level fabrication of square microhotplates and its characterization:** A simple square microhotplate is fabricated and detailed fabrication steps are documented. The performance of fabricated microhotplate is evaluated using a simple measurement setup.

- **Unified model for gas sensor analysis:** A system level modeling approach for field effect based sensor is developed where the effect of gas exposure on the gas sensor surface and its effect on the device response is unified. The model is verified with experimental results reported elsewhere. The developed model will aid sensor designers in design optimization and to predict the sensitivity and selectivity with respect to different gases.

1.3 Outline of the Thesis

The organization of thesis is as follows; chapter II present the three important components of a microhotplate, along with the review of modeling and various performance evaluation methods. Chapter III presents the various model and simulation studies developed. Fabrication and characterization method of a simple microhotplate is documented in chapter IV. The analytical model developed for the sensitivity and selectivity analysis is presented in chapter V. Finally, conclusion and possible future directions are presented.

1.4 Summary

In this chapter, a brief overview and the relevance of microhotplates is presented along with the major contributions and thesis outline.

2

Review of Literature

MANY application areas employ microhotplate, as it aid in significant performance improvements. For example, in a microcalorimeter application, microhotplates help to achieve small sample volume, fast response and high sensitivity [30]. In chemical sensors, microhotplates improve the sensor responses by promoting the chemical reaction between the sensing film and the gas species [31]. The efficiency of thermal infrared emitters can be improved by enhancing the performance of the microhotplates [28]. In Piezo-actuated display package (PADP), use of microhotplates reduces the dependencies on surrounding temperature [32]. The microthruster or micropropulsion system utilizes microhotplates as microigniters [33]. In the lab on chips application area, microhotplates has improved the response of biological reactions, without damaging the sample [10, 11, 34–36]. Silicon photonics is an another important application area which widely employs microhotplates to efficiently tune photonic devices with negligible insertion loss [37].

Various books, review articles and book chapters targeting a specific microhotplate applications (for example, Infrared emitters, Microbolometer, Gas sensors, Flow sensors etc.) have been published in recent years [38–47]. Simon et al., have dedicated a significant portion in reviewing the microhotplate structures, materials, modeling etc., [39] in their article on gas sensors. This chapter referred majority of the literature in which the microhotplates are designed for gas sensing application. Therefore, by giving prime emphasis on microhotplates for gas sensing application, we attempted to answer the key questions such as: how factors such as heater design, materials choices, insulation layer, membrane type etc., affects the performance of a microhotplate?, what are the tradeoffs involved with each design choice?, what are the various characterization methods? The topic covered in this chapter could aid a potential microhotplate designer to realize a high performance microhotplate for gas sensing application.

2.1 Microheater

Among the three main components, microheater is the heart of a microhotplate and it works on the principle of joule heating. Various performance parameters such as power, temperature uniformity and operating temperature can be tuned by its careful design. The three designer choices (heater geometry, heater material and electrical contacts) are discussed in this section.

2.1.1 Heater Geometry

Various heater geometries such as Meander [5, 14, 26, 28, 30, 48–51], Double Spiral [4, 17, 50, 52], Parallel Meander [7], Double Meander [9], Circular or concentric Rings [53, 54], S Shape [6], Line [12, 36, 55], Square Ring [3], Single Ring [10], Fan Shape, Honeycomb [5], Drive wheel [5] and R-Shape [8] are reported in literature.

Meander is the most commonly reported heater geometry because of its simple design. All the above mentioned microheater geometries have some degrees of temperature non-uniformity, however, meander heater suffers from hotspot formation in center [56, 57].

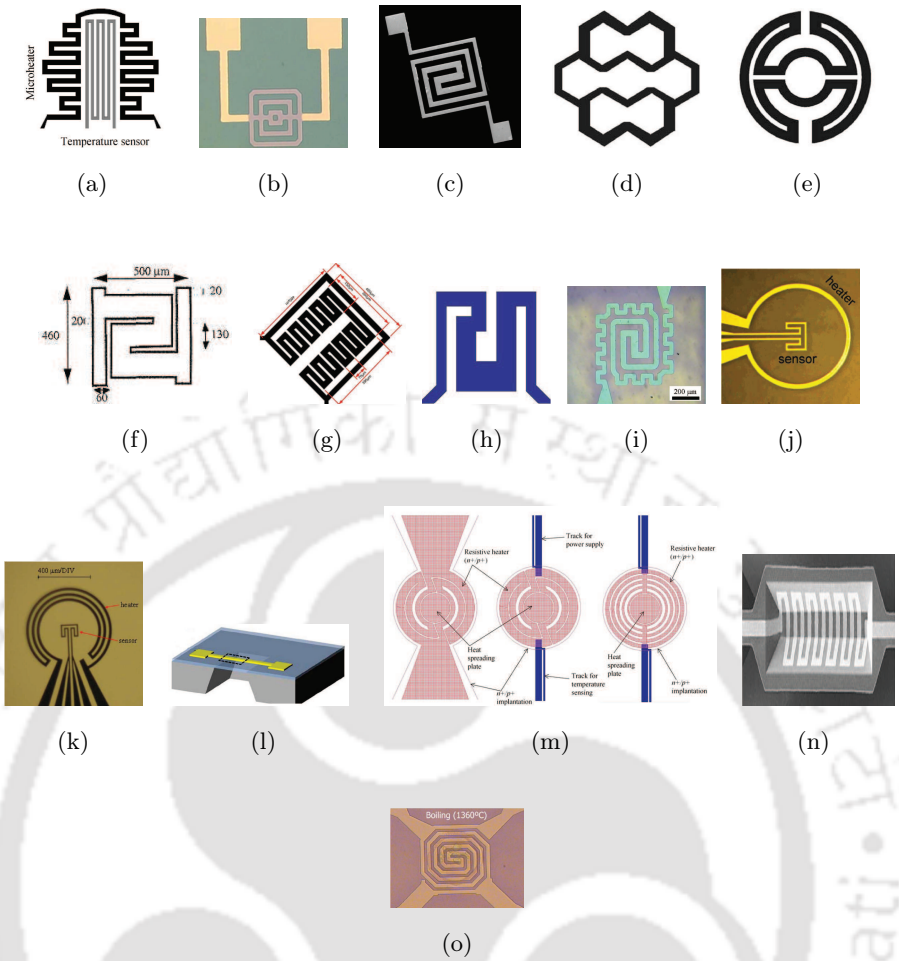

(a) (b) (c) (d) (e)

(f) (g) (h) (i) (j)

(k) (l) (m) (n)

(o)

FIGURE 2.1: Various microheater geometries reported in literature (a) [2], (b) Square Rings [3], (c) Double Spiral [4], (d) Honeycomb [5], (e) Drive-wheel [5], (f) S shape [6], (g) Parallel-Meander [7], (h) R-Shape [8], (i) Double Meander [9], (j) Single Ring [10], (k) [11], (l) Line [12], (m) Concentric Ring [13], (n) Meander [14] , (o) Meander spiral [15]

The primary reason for this is the thermal losses from its peripheral parts to the membrane. Since the meander has constant power per active area, these losses result in a significant temperature difference between the center and the edges, leading to a hotspot [58]. The temperature non-uniformity due to thermal losses are affected by various parameters such as microhotplate dimensions and membrane material [56]. To solve the hotspot formation issue, the geometries are often designed with variable track width in the microheater [9, 17, 56], and some of these reported geometries are shown in Fig. 2.1.

In-order to compensate for the thermal losses from the peripheral parts of microheater, Hille and Strack in [58], employed an additional co-centric heater, which is later adopted in [13, 59]. However, deciding the dimension of this additional ring is not a trivial task

because of its dependency on the membrane type, dimensions, material composition etc. FEM simulations can be used for such optimization, but these simulations are time consuming. Recently, Khan and Falconi presented an analytical methodology which can be employed for the designs of such co-centric heater [57, 60]. In a different heat management approach specifically to cope with the heat losses from the heater circumference, spiral heaters have been designed with different line width. Baroncini et al. designed their Spiral heater geometry with variable line width [17]. This design technique has decreased the temperature non-uniformity in the spiral heater from 13% to 4% [56]. In order to systematically decide upon the variation in line width of a double spiral design, Velmathi et al. establishes a ratio of inner to outer heater line width [4]. Double meander heater is an another heater geometry that results from the line width variation. Courbat et al. designed the double meander heater [9] by keeping the width of the heater wider in the center. Whereas, by meandering the track, Laconte et al. designed a loop-shaped-meander structure to achieve the temperature uniformity, designing a meander in a loop shape increases the resistance of heater. Moreover, this heater design may also be advantageous for co-planer applications [61]. Summarizing from the various heater geometries, the temperature uniformity of heater can be ensured by judicially designing the lines width in heater and managing the current densities. This helps in managing joule heating to compensate for the thermal losses.

2.1.2 Heater Materials

The choice of heater material depends on various factors most importantly the targeted operating temperature and cost of fabrication. Based on these factor different materials have been reported in literature for realizing microheaters. Some of these materials are Platinum [14, 51, 53], Aluminum [2], n^+/p^+ Silicon [13, 30, 62], Polysilicon [6, 61, 63], Titanium [3, 55], Titanium nitride [64], Molybdenum [15], Tungsten [65, 66], $SnO_2 : Sb$ and HfB_2 [67]. The wide spectrum of materials summarized in Fig. 2.2a shows the popularity of various heater materials.

Platinum is the most commonly used heating material [9, 16, 68–71] because of its; high melting point, high resistance to oxidation, ability to work at high temperatures

without structural deformation, ability to handle large current densities, stable temperature coefficient of resistance, good linearity, good chemical and thermal durability, faster change in resistance compared with the polysilicon [49] and high thermal reliability [13]. However, platinum metal suffers from poor adhesion problem and it needs an adhesion layer which again increases the fabrication complexity [15, 16, 72]. Also, at temperatures above 650°C, platinum shows a drift in its resistivity values [64].

Molybdenum is a CMOS compatible material i.e., easy integration and ease of patterning, as an additional advantages Molybdenum also has high melting point, low resistance drift at temperature higher than 700°C [15, 73]. On the other hand, Tungsten is already employed as CMOS interconnects. And it can withstand high temperature and is not prone to electromigration effect [65, 66]. However, tungsten and molybdenum forms their oxide below 400°C [74]. Therefore, they need a protective layer over them.

Integration of other CMOS compatible materials such as polysilicon and aluminum is less expensive. However, polysilicon based heater suffers from long-term drift of electrical resistance because of the grain instability above 550°C [66, 75, 76]. Whereas, Aluminum is not suitable for high working temperatures because of its low melting temperature. Also, at high temperatures, electromigration effect in aluminum heaters becomes rampant [13]. Another CMOS compatible material is silicon which is utilized as heating material because of its ease of fabrication. Moreover, silicon heater can be employed to achieve temperature as high as 800°C [77]. However, for achieving low noise, rapid heating and high thermal sensitivity, it requires degenerate doping of silicon [13, 30, 78]. Also a point to look out for when opting for silicon heaters is their possibility of contamination during the wet etching process [79]. Moreover, at high operating temperatures, rapid oxidation of silicon limits its operation. Silicon oxidation can be avoided by the deposition of a silicon nitride layer over the microheater. Fabrication of silicon heater is eased by using Silicon on Insulator (SOI) wafer. Apart from silicon, an another choice of semiconductor heater material is heavily antimony doped tin dioxide ($SnO_2 : Sb$) [80]. Spannhake et al. have reported microhotplates with $SnO_2 : Sb$ heater elements which can perform up to ~1000°C temperatures [80].

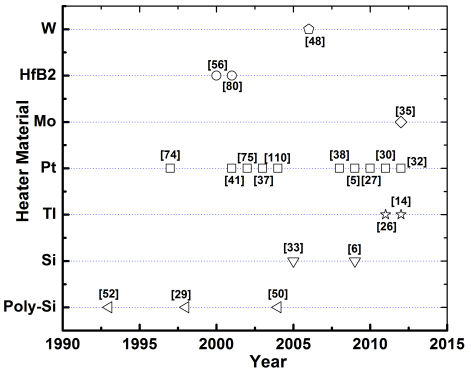

(a)

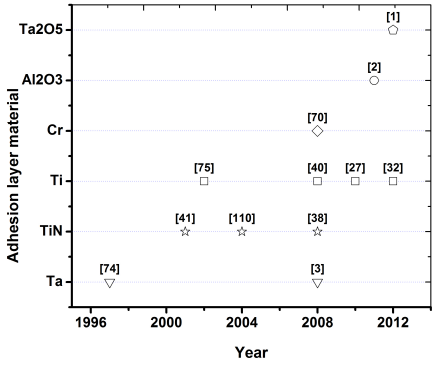

(b)

FIGURE 2.2: (a) Reported heater materials (b) Summary of adhesion layers employed for platinum. It may be noted that the number in the parentheses indicates the reference number.

Adhesion Layers

When employing platinum as an heating material, often a thin layer of refractory metal (such as Cr, Ti or Ir) is deposited first to improve the adhesion of platinum over the membrane. Fig. 2.2b, summarizes the different adhesion layer materials employed for platinum metal. During high temperature annealing process, adhesive layer often diffuses into platinum. Diffusion of some adhesion layer materials is found favorable, whereas, some brings reliability issues. Iridium diffusion into the grain boundaries of platinum increases the microheater resistance by 74% [9] and chromium diffusion leads to 14% increase in resistance [81]. Use of IrPtTa lessens the electromigration effect in the microheaters, because of the diffusion of iridium and tantalum into the grain boundaries of

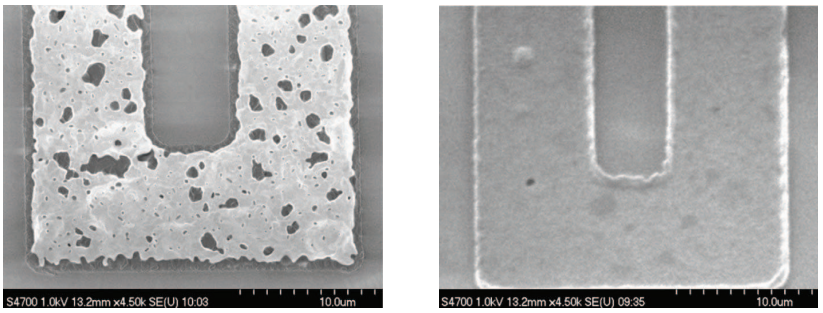

(a) (b)

FIGURE 2.3: (a) Pt heater with Ti adhesion layer heated at 600°C for 1 hour (b) Al_2O_3 adhesion layer heated at 600°C for 1 hour [16]

platinum. However, such diffusion reduces the microhotplates reliability [9]. Adhesion layer also affects the lifetime and performance of the microheaters. During annealing process, Tantalum forms its oxides, resulting in the failure of either the microhotplate or the wire bonding. Courbat et al. have overcome this by using Tantalum Silicide layer [9]. Another parameter of adhesion layer which affects the microheaters performance is its thickness. Firebaugh et al. have studied the effect of adhesion layer thickness and found that in thick adhesion layer, the resistivity of microheater increases due to the nucleation and the growth process developed during Si_3N_4 deposition [69]. Though, they suggested to have further investigations, in this case, it appears that a thin adhesion layer does not affect the resistivity. Tantalum Silicide, Titanium and Tantalum Pentoxide have also been used as an adhesion layer on nitride microhotplates [26]. Xu et al. have used Al_2O_3 adhesion layer and compared its reliability with Ti adhesion layer. While the Pt heater with Ti as adhesion layer develops micro holes (see Fig. 2.3) when heated at 600°C, Al_2O_3 adhesion layer has no such problem at same temperature (600°C) and time (1-hour). However, Al_2O_3 layer needs careful fabrication, since the alkaline solution, which is generally used to release the membrane, also attacks the Al_2O_3 layer [16].

2.1.3 Electrical Contacts

Electrical contact provide the connection between microheater and contact pads. The shape and width of the electrical contacts influence the microhotplates power consumption [61]. As a word of caution, the improvement in the power consumption resulting from the down-scaling of microhotplate dimensions will be squandered by the major heat

losses through unoptimized electrical contacts [52]. Since, microheaters work on joule heating effect, the design goal is to maximize the heat in the heater area and minimize it in the electrical contacts. For improving the temperature uniformity, Courbat et al. suggested to increase the ratio of heater resistance to electrical contacts resistance [52, 61]. This can be realized by keeping smaller line width in heater design and this in-turn results in an increased heater resistance. However, electromigration effect and fabrication technology limit the minimum heater line width. Whereas, a wider electrical contact will result in low contact resistance, enabling to have more voltage drop across the heater. Nevertheless, electrical contacts also act as a heat sink and the thermal losses because of their this nature depends directly on the size of these contacts. Hence, thermal losses in wide electrical contacts will be higher. In contrast, narrow electrical contacts decrease the thermal losses and hence the voltage drop across the heater as well as the temperature attained will be less. Therefore, while designing electrical contacts line width and shape, designer has to consider the minimum wire bonding area, electromigration effect and heat sinking effect. In an investigation reported by Courbat et al. in [52], tapered metal contacts and optimized line width has resulted in power saving of 20%. Recently, Khan et al. has presented a systematic approach, which can be employed to decide the contact width [57]. In a different approach for achieving high heater to electrical contact resistance ratio which will maximize the operating temperature with same applied power, Iwaki et al. used separate materials for electrical contacts and heater, for minimizing the electrical contacts resistance [13].

To quickly summarize some of the key microheater design aspects, high temperature uniformity can be achieved by employing optimized microheater geometrical parameters such as number of tracks, shape and width. Similarly, electrical contact width and shape also need to be designed in-order to achieve a high heater to contact resistance ratio. As for the heater material, the appropriate material can be chosen according to the desired operating temperature. If the fabrication costs permits, platinum can be used for applications where temperatures within $< 600°C$ are desired. Aluminum and polysilicon are other attractive inexpensive materials for very low temperature range. Antimony doped tin oxide ($SnO_2 : Sb$), mono crystalline silicon and molybdenum are the proven materials, for temperatures higher than 600°C.

2.2 Support Platform

The design of a suitable platform for the microheater geometries, affects various microhotplate performance parameters such as temperature uniformity, thermal time response, mechanical stability, scalability, operating temperature, power consumption. The support platform can be subcategories on the basis of their shape such as, bulk, closed type membranes and open type membranes. Among these three types, bulk type platforms does not employes any form of micromachining technique, rather, the microheater is patterned directly over a bulk substrate. Though the fabrication process is relatively simple, the large thermal mass of the bulk substrate, results in a higher thermal losses to the substrate which directly affects the highest achievable temperatures. In addition, the thermal diffusion through the bulk influences functioning of on-chip electronic circuitry. Therefore, for high performance microhotplates, a bulk platform is not a wise choice. Nevertheless, because of their small cost and fabrication complexities, some application areas such as microfluidics [55] and biomedical [10, 11, 36] often uses bulk substrate. To overcome the disadvantages of the bulk substrate, microhotplates are often fabricated on suspended membranes, which have reduced thermal mass.

Reducing the thermal mass of the support platform improves the scalability and power consumption, because of the confinement of heat in the membrane area [52, 82]. With an increase in thermal confinement, the highest achievable temperature in the active area also increases, for the same applied bias as in bulk [62]. Swart et al. found that for micro-bridge structures, the scaling of the heater and the cavity dimensions by a factor α results in an improvement of α^2 in the response time [83]. Suspended structures also help to isolate the high temperature microhotplate from the rest of the substrate. Reduction in thermal crosstalk and feasibility of associated electronics helps in realizing the System on Chip (SOC) designs [29]. This is because the System on Chip designs will require integration of the driving circuitry on the same substrate along with a microhotplate.

2.2.1 Type

Suspended structures are realized by utilizing bulk and/or surface micromachining.

The method of micromachining employed results in two types of suspended structures. Which are, the closed type (membrane type) where the rims of the substrate supports the thin membrane [6, 9, 17, 48, 53], and suspended structure (open type) where the supporting arms hold the membrane. Both types of suspended structures lay over an etched cavity. Closed type structures employs etching from back side for defining cavity and the depth of etching defines the membrane thickness. Open type membranes realize the cavity by employing the top or front side etching and the membrane thickness is independent of the depth of etching. However, open type membrane are also reported where substrate is etched-through by combining bulk and surface micromachining techniques [52, 84]. Closed type membranes often need double side polished substrates and double sided alignment for bulk micromachining [84]. Pike et al., Baroncini et al. and Iwaki et al., utilize rectangular [85], square [17] and circular [79] respectively as closed type membrane shape. Among the three, circular membrane are mechanically more robust [13, 66].

Open type structures may have various supporting arms such as, spider membrane with four (or more) supporting arms [30, 49, 50, 52, 63, 86], microbridge with two arms structure [14, 16] or a cantilever structure with single supporting arm [51]. The number of supporting arms defines the mechanical stability and the thermal resistance of the membrane. Compared with four arm membrane, cantilever has lowest thermal mass, therefore less thermal losses. However, the mechanical stability of a four-armed membrane is higher than a cantilever structure.

In an open type membrane, one of the design aspect which needs designers attention is the supporting arms corner joints. This is because during the operation of open type membrane, thermal stress is accumulated at the corner joints of supporting arms and at the edge of the membrane, creating mechanical stability concerns. In one of the method to cope with these stresses, designers may employ corner compensation method in which joints are realized by avoiding sharp edges, convex and concave corners. Corner compensation method requires careful mask designing, knowledge of undercutting ratios and its dependence on the etchant [87, 88]. The advantage of this method is evident from [16], where corner compensation results in about 80% reduction in thermal stress.

Courbat et al. compares the performance of the bulk, closed and open type membranes for reaching a temperature of 300°C in [52]. The lower thermal mass of open type membranes as compared with closed or bulk substrate results in best power consumption [52]. Even-though the thermal mass of closed type membranes is higher than open type, closed membranes are equally relevant because of their less fabrication complexities, mechanical stability and better yield.

2.2.2 Choice of Membrane Materials

Materials used in membrane plays a significant role in the microhotplates performance. Various materials such as Silicon dioxide [48, 51, 66], Silicon Nitride [9, 12, 17, 26], Silicon Nitride/Silicon dioxide [3, 4, 7, 13, 14], Oxide/Nitride/Oxide [53, 54], Silicon/Silicon dioxide [6, 28], Polyimide (PI) [52, 81, 89], Porous Silicon (PS) [49, 84, 90], AlGaAs/GaAs [50], Aluminum Nitride (AlN)/Silicon Carbide (SiC) [68], Silicon Carbide (SiC) [91], Alumina [92] and Low Temperature Co-fired Ceramics (LTCC) [93, 94] have been used as membrane.

A single material or a composite membrane usually employs silicon, silicon dioxide and silicon nitride because of their CMOS compatibility. Silicon membrane is easy to fabricate but because of its high thermal conductivity, it has large thermal losses. The power consumption of a 1μm thick SiO_2 membrane is 75% less than that of a 1μm thick Si membrane for the same maximum temperature limit [95]. In contrast, SiO_2 and Si_3N_4 membranes can better confine the thermal energy in the membrane region only because of their low thermal conductivities. Compared to Si_3N_4, SiO_2 has smaller thermal diffusivity, and the maximum temperature reached with SiO_2 membrane is higher than Si_3N_4 membrane under same applied electrical power [48]. The problem with these single material membranes arises because of their poor mechanical stability [96]. The internal stress in a Si_3N_4 or a SiO_2 layer is above 0.1 GPa and it could lead to the buckling of the membrane [82]. These buckling causes reliability problems in microheater and results in membrane damage by peel off or fracture/microcracks. Silicon nitride layers have large tensile stress and silicon dioxide layers have compressive stress [82]. Therefore by choosing a suitable thickness of Si_3N_4 and SiO_2 layers to form a Si_3N_4/SiO_2

composite membrane, the internal stress can be balanced [16, 84]. With the goal of achieving stress balance, some authors have also reported the use of $Si_3N_4/SiO_2/Si_3N_4$ composite membranes [62, 96]. Besides, in these composite membranes, intrinsic stress of the silicon nitride can be tuned by using silicon rich nitride [82]. For ensuring a good mechanical stability in microhotplates, designer may decide on the individual layers thickness in the composite membrane by keeping the total residual stress in the range of $-0.1\text{GPa} < \sigma_{\text{res}} < +0.1\text{GPa}$ [82].

Microhotplates on Gallium Arsenide (GaAs) substrate provide solutions for micro - optoelectronic, RF-MEMS and optical telecommunication applications [50]. GaAs substrate also simplifies on-chip integration of driving circuitry and MEMS devices [50]. The drawback of using GaAs for MEMS would be the cost of fabrication compared with the already matured low cost CMOS silicon processes. Polymeric substrates are alternative for low power MEMS because of the advantages such as flexibility and less complex, low cost fabrication steps. Ease of integration of microheaters on these membranes enables their applications in various fields such as micro-fluidics, gas sensors, flow sensors and thermal actuators [89]. A low conduction losses in the membrane or substrate can be ensured by employing PI substrates, this is because of their low thermal conductivity (0.15 - 0.28W/mK [89, 97]), as compared to inorganic materials such as silicon dioxide, silicon nitride. Power saving offered by PI substrate can be maximized further by employing a cantilever or spider membrane. With the PI membranes, Courbat et al. achieves a temperature of 300°C with just 6 mW power [52]. Moreover, owing to its low thermal conductivity, better mechanical stability and yield is possible by using thick PI membranes. However, the plastic deformation and change in the microheater resistance, limit its application to low temperature regime (< 400°C) [89, 97]. Because of the matured CMOS technology the oxy-nitride membrane could be as thin as 530nm [85], whereas, PI membranes of $1 - 10\mu$m thickness are only so far realized [97]. Compared to the reported, 1μm thick PI membrane, this corresponds to ∼2 times scaling down of oxy-nitride membrane thickness. Nevertheless, as a non-CMOS material, research with thinner PI membrane can bring potential advantages.

Inorganic material membranes can work in wide temperature range when compared with polymeric membranes. However, materials like Si_3N_4, SiO_2, Si and combinations of

the same, usually need a thin membrane because of their high thermal conductivity. Reducing the thickness improves the power consumption but can lead to mechanical instability [98]. In this regards, Porous Silicon (PS) has attracted the attention because of its low thermal conductivity [49, 90, 99–102]. Both closed and open type membrane have been fabricated with PS. Compared to thin SiO_2 or Si_3N_4 membranes, low thermal conductivity of PS helps in achieving similar or even lower power consumption with thicker membranes. Compatibility of PS material with CMOS technology is also an additional advantage which eases its integration to the process flow [99, 101].

For the applications involving harsh environmental conditions which include high temperature and gaseous atmosphere, Silicon Carbide (SiC) or ceramic substrates are good choices. SiC displays chemical stability and works well in high temperature surroundings [67, 103]. However, its fabrication is complex due to its high chemical stability. Ceramic substrates such as Al_2O_3 and LTCC are other material choices, especially for harsh environment conditions. Ceramic materials possess favorable properties such as high thermal stability, low thermal conductivity and high mechanical stability. Moreover, ceramic materials are good candidates for inexpensive middle scale production, as the clean-room production is not a necessity [92–94]. However, for ceramic technology, miniaturization and hence, power consumption is an area where further improvements are needed. Table 2.1, summarizes the advantages and disadvantages of different reported materials.

2.2.3 Dimensions of Membrane and Supporting Arms

For close type membranes, Membrane to Heater Ratio (MHR) can be defined as ratio of membrane side length to the heater side length. A large MHR means a larger distance between the heater and membrane edge and this distance influences the power consumption, temperature uniformity, time response, mechanical stability and device density. When MHR is increased, while keeping membrane thickness and materials constant, it results in an increased thermal resistance between the heater and membrane edges. An increased thermal resistance leads to an improvement in power consumption and temperature uniformity of the microhotplate. However, an increased thermal resistance degrades the thermal time response. In addition, a large MHR also adversely affects the

TABLE 2.1: Summary of membrane materials employed in microhotplates

Year	Material	Advantage	Disadvantage	Affiliation, Ref.
2011	Glass	Less fabrication complexity	Higher thermal losses	SKLTT-China, [55]
2009	Si/SiO_2	CMOS compatible, reproducible	High thermal conductivity of Si	Fraunhofer IWM, Germany, [28]
2011	SiO_2/Si_3N_4	CMOS compatible, minimum residual stress, reproducible	Thin membranes is required for optimum performance	SKLTT-China, [14]
2008	$SiO_2/Si_3N_4/SiO_2$	CMOS compatible, minimum residual stress, robust, reproducible	Thin membrane is required for optimum performance	ETRI, South Korea, [54]
2008	Porous Silicon (PS)	CMOS compatible materials, low thermal conductivity, mechanical stability	Commercial availability, reproducibility issues	NCSR ''Demokritos'', Greece, [99]
2008	Polyimide (PI)	Simple fabrication steps, flexible, low thermal conductivity, mechanical stability	Not CMOS compatible, failure at high temperatures, reproducibility issues	SAMLAB, EPFL, [52]
2008	Alumina (Al_2O_3)	CMOS compatible, immune to high temperature, inexpensive fabrication, low thermal conductivity, mechanical stability	Scalability and power consumption issues	University Rovira i Virgili, DEEEA, Spain, [92]
2001	SiC	Immune to high temperature and harsh chemical environments	Not CMOS compatible, reproducibility issues	First sensor technology GmbH, Germany, [103]

mechanical stability and device density [28, 52, 104]. Therefore, an efficient microhotplate needs a careful selection of MHR value. Finding an optimum MHR value is also important because it has been found experimentally that the power saving offered by a very large MHR practically saturates after a certain value. Courbat et al. experimentally studied the effect of polyimide membrane area, and found that beyond 200 μm$\times$200 μm [52], power saving is saturated. Similar results are obtained by Gotz et al. [105] where the power consumption for a 350°C temperature does not improve beyond a MHR value of 1.4. Similar experimental findings are reported by Simon et al. in their review [39]. Ali et al. have related the membrane and active area with power consumption, on the basis of a figure of merit term which evaluates the power consumption per unit active area [65]. The advantage of such figure of merit is that it allows a direct comparison of microhotplates with different membrane material and thickness. Moreover, such figure of merit enables a direct comparison of both closed and open type membranes.

The membrane thickness directly affects the power consumption of the microhotplate and the fabrication limits sets the minimum thickness of membrane. Besides power, final thickness of membrane should also consider the mechanical stability aspects of the membrane. Gotz et al. report the yield of square membrane dimensions. A 100 nm thick Si_3N_4 membrane provided the lowest power consumption but its yield, for all the three membrane sizes (700 μm$\times$700 μm, 900 μm$\times$900 μm and 1100 μm$\times$1100 μm) is the lowest. Among membranes of thickness ranging from 1.1 μm to 3 μm, larger area membranes have the lowest yield [105]. Astie et al. report similar results, where, for a lower membrane thickness of 1.5 μm, the yield is less than 40% [6]. While designing suspended structures such as bridge, spider and cantilevers, tradeoff that exists between power and response time has to be taken into account. For this purpose, an optimized dimensions of supporting beam can be employed [30]. The underlying principle behind these optimizations comes from the fact that the power consumption can be decreased by increasing the thermal resistance (either by thinning of membrane, using low thermal conductivity material or by increasing distance between heat source/sink) and the thermal response is improved by reducing the thermal resistance [80]. Nevertheless, increasing the supporting beam length, raises the risk of membrane buckling [28, 77]. Membrane buckling and its effect can be alleviated by judicially choosing membrane materials, shape of support beams and its compositions. The dimensions of supporting arm can be varied for finding a balance between mechanical stability, power consumption and thermal response time.

In summary, while one way of achieving temperature uniformity and improving other microhotplate's performance parameters (such as operating temperature, power consumption, reliability and scalability) is by judicially designing microheater geometries, another approach for improving performance, is by reducing the thermal losses to the membrane, by wisely choosing the appropriate membrane type, dimensions, material compositions, and by keeping in mind factors such as the fabrication complexities and feasibility etc. Ideally, the cantilever design is a best fit for high performance, due to its lowest thermal mass. However, practical aspects such as thermal stress related mechanical stability issue, buckling due to residual stress of materials and fabrication complexities make microbridge and spider membranes a viable choice. On the other hand, better yield, mechanical stability and lesser fabrication complexities make closed

membranes equally important. Thermal losses, thermal response time, mechanical stability and microhotplates lifetime are greatly influenced by the materials employed in fabrication. A wide range of materials have been tried out, while the fabrication cost, desired performance, device dimensions are some of the key parameters, affecting the material choices. For a high performance microhotplate with low power consumption, fast response time, scalable design, good mechanical stability and good temperature uniformity, where the fabrication cost is compensated with the bulk production, classical CMOS materials have been proved. As an emerging alternative to CMOS materials, low thermal conductivity PI or PS membrane can be a good direction. For high temperature and harsh environment applications such as infrared emitters, automobile industries etc., SiC and ceramics are the materials of choice. Ceramics is a promising technology for a small scale production, where low fabrication cost is desired and larger area is acceptable.

2.3 Insulation Layer or Heat Spreader

It is often required to provide an electrical insulation layer to separate the thermal domain from the application domain, while preserving the good thermal efficiency between the two domains. For example in gas sensor, a passivation layer insulates the microhotplate from the sensor [17, 61] and in microfluidics, it separates the fluidic domain from the thermal domain. In platinum microheaters, it has been reported that an insulation layer helps in mitigating the degradation caused due platinum exposure to surroundings oxygen [71]. For microhotplates, an insulation layer should have a balance of contrasting properties that is, good thermal conductivity and good electrical insulation. Silicon Nitride (Si_3N_4), Silicon Dioxide (SiO_2) and Silicon Carbide (SiC) are the major materials employed in microhotplates either as an electrical insulator or as a heat spreading layer. Silicon dioxide is an excellent electrical insulator but its thermal conductivity is the lowest among the three materials. Silicon Carbide has better thermal conductivity than Silicon Nitride, and it helps in achieving an temperature uniformity of 0.005 K/μm [106]. However, the process complexity of SiC is higher. Compared with SiC, a Si_3N_4 layer is easy to deposit and it offers better electrical insulation than SiC [107]. Neda et al. experimentally observed the effect of SiO_2 passivisation layer on the time response and

for improving the time response they suggested the use of other passivisation materials, such as diamond and Si_3N_4 as passivisation layers [108]. Nitride insulation layer not only increases the mechanical stability of the membrane, but also the achievable temperature [5]. Recently, we have found that by employing an optimized dimension of nitride insulation layer, the temperature uniformity and the power consumption is improved. This is because, with selective deposition, the thermal conductivity can be increased only in selected part of the membrane, i.e., in the active area. In addition, this will not add any complexity to the existing fabrication steps [109]. However, a thicker insulation layer increases the power consumption and thermal response time [110].

2.4 Modeling of Microhotplate

Microhotplate dimensions and material choices affect the thermal profile in the membrane. For example, with a meander heater, a thin oxide-nitride membrane will help to attain high temperatures at low power, however, the thermal distribution will be bell shaped, depicting a temperature non-uniformity. Optimization via FEM simulations or mathematical models, aids the designers to choose an appropriate material and to finalize the dimensions of an efficient microhotplate [52, 67, 85, 86, 111]. The advantages of modeling over FEM simulations, are the small calculation time and better control over the accuracy of results. The mathematical modeling is approached either by solving the diffusion equation (in 1D, 2D or cylindrical coordinates) or by developing a lumped element model. Pike and Gardner developed a lumped element model for a back etched, closed type microhotplate [85]. The thermal capacitance (C) accounts for the heat storage in the lumped elements. The membrane is divided into four strips and each strip contributes its own resistance and capacitance. Finally, the heat balance equation is applied for transient response analysis. This approach neglects the heat loss at the corner regions of the membrane and the thermal convection outside the heated area [85]. For improving modeling accuracy, corner losses can be taken into account by employing a circular membrane shape approximation instead. The steady state thermal power calculated using this model is in close agreement with the experiment results. Another

lumped element model, developed by Mo et al., considers the heat losses due to convection and radiation, in a spider microhotplate [86]. This model treats the microhotplate as an electrothermal transformer and state space analysis is carried out for the coupling stability of the microheater. In summary, the lumped model can be employed for the quick estimation of power consumption and the response time of the microhotplates.

In contrast to lumped modeling, derivation of analytical model, by solving diffusion equations, also provides the temperature distribution of microhotplate. Kozlov et al. use Fourier series method for developing an analytical model to find out the temperature distribution in the multilayered parallelepiped structures of heat-generating devices on a close type membrane [96]. The 3D device structure is simplified to a 2D one, due to the negligible temperature gradient along the thickness. Multilayered membrane is substituted with a homogenous material membrane with equivalent parameters. The thermal distributions are computed for both equivalent homogenous and multilayered membrane and errors are within 1.1%. In [60], Khan et al. showed that a perfectly circular temperature distribution can be accurately expressed in terms of modified Bessel functions. However, due to various reasons such as the hotspot formation, effect of contact pads or corner effect in square membrane, often, the thermal contours are not perfectly circular. A circular symmetry can be achieved, either by choosing materials with very different electrical resistivities for heaters and electrical contacts [13] or by adopting proper design strategies as reported in [57]. Ansari et al. developed a model by solving the diffusion equation for microcantilevers to predict the temperature distribution due to self-heating [112], in a two-step approach. In step one, only the conduction loss is considered and in the subsequent step, the convection loss is included. The model neglects radiation loss in both steps. Finally, the model is confirmed with FEM results. An obtained deviation of 4% is attributed to the approximation involved in thermal conductivity and convection coefficient values. Most models assume a constant value for material properties and a constant convection coefficient, to simplify the analysis. However, material properties and convection coefficient are temperature dependent. In addition, scaling of microhotplate also affects the natural convective coefficient [113]. The thermal perturbation caused by the contact pads is often ignored. However, due to finite resistance and heat sinking abilities of the contact pads, the isotherm on the

membrane is disturbed [60]. This affects the temperature uniformity of the microheater in the active area. Therefore, for improving the accuracy of analytical analysis, the effect of pads should also be considered.

2.5 Methods of Characterization

In this section various methods employed for the measurement of microhotplate's key performance parameters such as microhotplate reliability over repeated usage, deformation, individual layer stress measurement, operating temperatures, heater resistance, temperature coefficient of resistance and thermal time constant are discussed.

Among the different measurement techniques employed for resistance measurement, heater resistance can be determined by passing a low sense current (typically 10µA) through the microheater and measuring the voltage developed across it. A low value of sense current helps in reducing the joule heating associated with it. During measurements, the microhotplate is placed either in an oven or on a thermal probe station. This ensures an uniform thermal profile across the microheater. Otherwise, the joule heating may cause nonuniform heat distribution in the microheater and therefore, affects the accuracy of resistance measurements [17, 26]. Using similar setup, the temperature dependent resistance and temperature coefficient of resistance (TCR) can also be measured. This measurement is carried out by varying the temperature of external heat source in defined thermal steps. In a method for determining microheater TCR values, the heater resistance are approximated using a linear equation which relates the temperature to the heater resistance [15]. However, for microhotplates performing at higher temperatures, TCR can be calculated more accurately using Callendar – van Dusen equation [114]. In comparison with Callendar-van Dusen equation, linear equation overestimates the microheater resistance by 12% when operated at 900°C [8].

The thermal time constant can be measured by sourcing the current or voltage to the microheaters and by noting the time needed to reach stabilized temperature [50]. For measuring temperature, thermocouples [9] or on-chip thermometer/temperature sensors are usually adpoted. Commercial instruments such as, Laser Raman thermometry, liquid

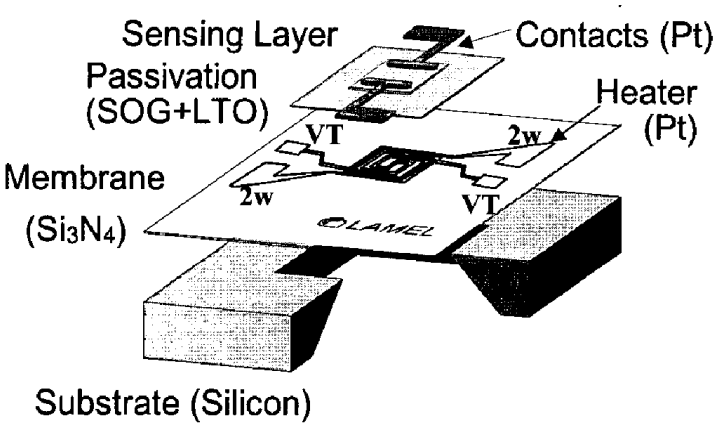

FIGURE 2.4: Solid-state gas sensor where the microheater is patterned along with the four-point probe heating element configuration. For passivisation, layers of Spin On Glass (SOG) and Low Temperature Oxide (LTO) were employed. [17]

crystal thermography, scanning thermal microscopy, visible-NIR thermography and Near-Field infrared scanning microscope [30, 49, 115–119] can also be employed to accurately measure the thermal distribution. Moreover, from these precise thermography results, crucial design parameters such as thermal conductivity, emissivity and heat transfer coefficients etc., can be extracted. By using these measured parameters in FEM simulations and in analytical modeling, thus the obtained results will be more accurate. Moreover, many authors have employed thermography measurements to extract the thermal resistances and TCR values also [30]. Incorporating four point probe heating element [17, 61] is an another technique reported for measuring the temperature of the active area. In this method, the voltage taps or pads are provided to sense the change in resistance of the heater (see Fig. 2.4). These taps or pads are designed to minimize the thermal loss through them and are attached to the main microheater design. The extra voltage pads allow measuring the temperature versus resistance changes in either two points or Kelvin type (four point probe measurement) arrangement. In two probe testing, measurements are made by sourcing current into heater pads and sensing the voltage across the microheaters. In four probe measurement, the heater pads are supplied with a low sensing current while the voltage is measured across the test pads [17]. Advantage of this method lies in the lower cost of testing and alleviation of other sophisticated instruments. However, this method can find out only the average temperature profile along the heating element length, instead of active area temperature [17].

For characterization of mechanical stablity of microhotplates, methods such as optical

profilometery [9], optical interferometer [65] and 3D vibrometer [53] are used. These noninvasive methods are basically adopted for the deformation study of microhotplates during operation. Another noninvasive technique employed for measuring the deformation is digital holographic microscopy [120]. For measuring the stress in individual layers of a composite membrane, wafer curvature measurement [15] can be employed. Another approach to evaluate the mechanical stability of the fabricated microhotplate is by using pulsed voltage test [16]. This test applies the voltage, to the microheater, in pulse mode and the frequency of this pulse is decided from previously known thermal response time. This condition allows the microhotplate to reach its steady state mechanical deformation as well as temperature. In this way, the number of repeated cycle before the mechanical failure occurs can be estimated [16]. A low drift in the heater resistance across wide repetition cycles is a desired characteristics from the microhotplate reliability point of view and pulsed voltage test helps in evaluating the resistance drift over repeated use [16].

Accelerated aging test helps in the reliability estimation of the microheaters [9], in this test the microhotplates are subjected to repeated thermal cycling. Apart from realiablity evaluation, in composite membranes thermal cycling leads to an additional advantage, as the thermal cycles mitigates any initial stress developed during the fabrication [120]. This in-turn helps in reducing the initial deformation of the membrane [120]. In order to decide up on the minimum line width in microheater which is limited by electromigration effect, calculation of maximum current densities can be carried out to reveal the electromigration possibility at a particular temperature [9].

For evaluating the heating efficiency of microhotplate, Ali et al. [65] and Xu et al. [14] uses a figure of merit (FOM) term such as power per active area (PPAA) or power per heater area. This term gives the information about the power needed by a microhotplate to heat up a $1\mu m^2$ area to the desired temperature. However, a proper FOM should also include parameters such as membrane to heater ratio, time response, mechanical stability and temperature uniformity. As discussed earlier, heat losses from outer heater edges to the membrane, is the major cause of temperature non-uniformity. The method used to improve temperature uniformity, for example, a two-heater microheater, requires additional power or methods such as the use of heat spreader, silicon island and increased

membrane thickness, increases the effective thermal conductivity, which consequently results in an increased power consumption. Hence, a microhotplate with good temperature uniformity might have high value of PPAA, but it is still better, from a performance point of view. Moreover, an area as well as operating temperature independent FOM will be beneficial for providing a wider comparison range. Table 2 summarizes the various microhotplate, design, process and membrane type and materials employed. Some entries are blank due to the lack of reported data. Especially, the values of time constant and temperature uniformity are not available in many papers. The PPAA is calculated for reaching a temperature of 250°C. The power consumption is deduced from the particular work, when the exact values are unavailable. Due to the lack of data, the FOM of few microhotplates is available in the table. Among these few, microhotplate developed by Mele et al. has the best PPAA with a value of $0.171 \frac{\mathrm{mW}}{1000 \mu \mathrm{m}^2}$.

2.6 Summary

A systematic review of microhotplates with an emphasis to the gas sensing application is presented in this chapter. Though the major conclusions are drawn at the end of each section, Fig. 2.5 summarizes the three microhotplate components (microheater, support platform and insulation layer), the designer choices and the specific performance parameters associated with each components. A list of most commonly desired parameters for a microhotplate is shown at the center of Fig. 2.5, where the interdependency among these performance parameters is also illustrated. The effect of increased thermal resistance on the key performance parameters is shown by one-way arrows.

For a constant applied power, an increased thermal resistance will reduce thermal losses and will lead to an improvement in the operating temperature. For the same reason it will also improves the power consumption and temperature uniformity, for a targeted temperature. However, thermal response time degrades, due to its inverse dependency on thermal resistance. If thermal resistance is increased by the thinning of membrane, the resulting membrane fragility and thermally induced stress, heighten mechanical stability issues. However, the thermal resistance can also be increased by employing a low thermal conductivity membrane which eliminates the membrane fragility issues. But at

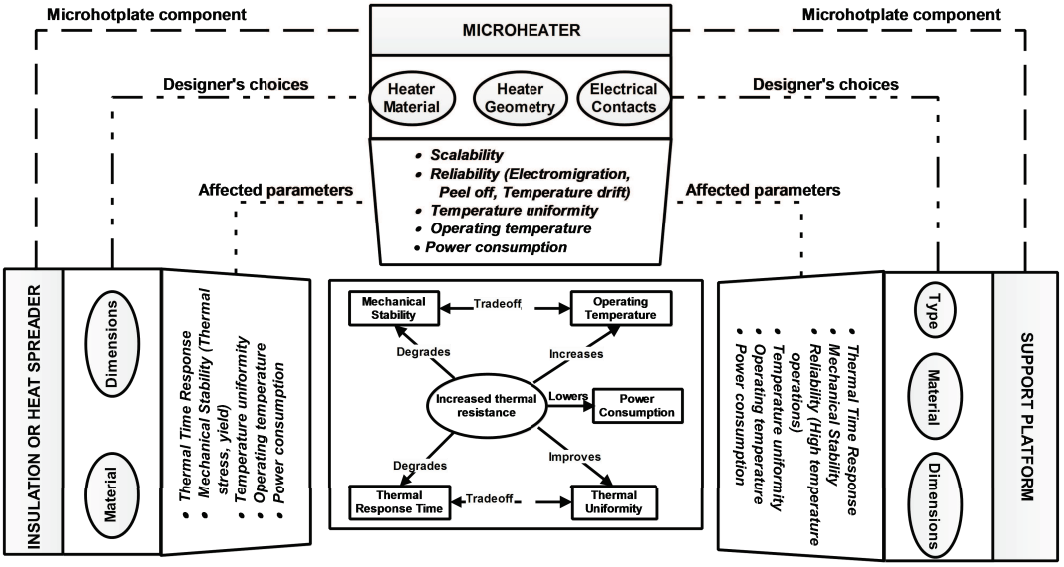

FIGURE 2.5: Microhotplate components, design parameters and the performance parameters associated with each component. Some of the key performance parameters and tradeoff among them are shown at the center.

increased operating temperatures, thermal stresses will again bring back the mechanical stability problems. The interrelation among performance parameters is shown with two-way arrows, which depicts the tradeoff among the parameters. An increase in operating temperature will deteriorate mechanical stability, due to increased thermal stresses. Whereas, if mechanical stability is improved with a thicker membrane, it reduces the operating temperature. Similarly, there exists a tradeoff between temperature uniformity and thermal time response, as the increased thermal resistance degrades the thermal time response but improves the temperature uniformity.

Among the three components, micro-heaters are the heart of the microhotplate, and by an optimum design of microheater, operating temperature, power consumption and temperature uniformity can be improved. Various designs have been tried out with the central idea of managing the thermal losses by a judicial choice of microheater design and materials. Various material have been reported in literature, among them platinum is the most widely used heating material. However, platinum metal suffers from poor adhesion problem, for which a layer of refractory material is usually deposited apriori. A careful choice of adhesion layer material can enhance the performance while minimizing the temperature drift and peel off problem.

Microhotplate consists of a platform which supports the microheater. The dimensions, material and type of this platform greatly affects the performance parameters such as, thermal time response, mechanical stability, thermal stress induced reliability issues, temperature uniformity, maximum operating temperature and power consumption. The support platform can be sub categories on the basis of their shape such as, bulk, closed type membranes and open type membranes. Though, for obtaining low power consumption, good temperature uniformity and maximum operating temperature, open type membranes seem to be a wise choice, the fabrication complexity, yield and mechanical robustness are some parameters which make closed type membranes equally reported in literature. The choice of membrane material for both closed and open type membranes, affects the performance parameters such as power, temperature uniformity, mechanical stability, time response, yield etc., of a microhotplate. Because of their low fabrication cost CMOS compatible materials such as Si , SiO_2 and Si_3N_4 are a suitable choice. However, thermal stress generated at the high temperatures, poses mechanical stability issues in these membranes. Composite membranes offer a solution for managing the thermally generated stress and hence improve the mechanical stability of CMOS material membrane. Moreover, composite membranes also allow to tailor the thermal conductivity of the membrane which could result in reduced thermal losses. As an alternative to CMOS materials, Polyimide (PI) and Porous Silicon (PS), owing to their low thermal conductivity, have been reported as alternative membrane materials. For high temperature and harsh environment applications such as infrared emitters, automobile industries etc., Silicon Carbide (SiC) and ceramics are the materials of choice. Ceramics in particular, is a promising technology for a small scale production, where low fabrication cost is desired and larger area is acceptable. Apart from membrane material, membrane dimensions also influence the power, thermal time response and mechanical stability of both closed and open type membranes.

The third major component of microhotplate i.e., the insulation layer is employed to separate the thermal domain (represented by microhotplate) and the application domain (such as a gas sensing layer or microfluidics channel). The choice of material to be used as the insulation material affects the power, thermal time response, temperature uniformity and mechanical stability, hence, employment of optimum dimensions of the insulation

layer will bring in performance benefits.

In the design of a microhotplate, as depicted at the center of Fig. 2.5, various tradeoffs exists among the performance parameters, for example, the mechanical stability of a closed type membrane is more with small MHR, however, the power consumption is more in such membranes. Another example is the width and length of supporting arm in the open type membranes which directly relates the tradeoff that exists between power consumption, thermal response time and mechanical stability. Therefore, in such case of study, analytical modeling and FEM simulations find their usefulness.

The experimental characterization of operating temperatures, deformation, thermal time constant, heater resistance and accelerated age testing have been carried out by many different methods. The employment of Kelvin type four point measurement pads and on chip thermometers in the microhotplate design, could result in a lesser dependency over sophisticated instruments. Definition of a standard figure of merit is another need in the method of performance evaluation. The reported figure of merit (PPAA) could include other interlinked performance parameters such as membrane to heater ratio, temperature uniformity, time response etc. A new Figure of Merit (FOM) should be able to compare the performance of any microhotplate, operating not necessarily at identical temperatures.

TABLE 2.2: Summary of various reported microhotplates (N = Silicon Nitride, O = Silicon dioxide, S = Simulation study, F = Fabricated results and NM = Not Mentioned)

Memb. Dimen. (µm × µm × µm)	Heater Dimen. (µm × µm × µm)	Memb. material	Heater type	Insulat. mat.	Sim. or Fab.	Opera. Temp. (°C)	Power (mW)	Deflection (μm)	TC	Temp. Uniformity (K/μm)	FOM @250°C ($\frac{mW}{1000\mu m^2}$)	Year,Ref.
1000×100×NM	300× 50×0.3	O	Meander	N	S	400	NM	NM	NM	NM	-	2008,[48]
1000× 1000×0.25	450 ×450×0.239	N	Double Meander	N	F	300	45	12	NM	NM	-	2008,[9]
500×500 ×1	$\pi 55^2 \times 0.2$	O/N/O	Circular	Pt/O	S+F	250	7.21	~1.6#	NM	NM	0.758	2008,[53]
1800× 1800 ×2.5	500× 460×0.4	O/P^+Si	S-Shape	O	F	450	166	NM	NM	0.28	-	1998,[6]
2100 × 1500 ×2	NM	N	Meander	O	S+F	154	NM	NM	NM	NM	-	2012,[26]
NM×0.2	NM	N	Line	None	F	NM	NM	0.4	NM	NM	-	2012,[12]
NM	345×385×0.25	N/O	Sqr. Ring	NM	F	250	387	NM	NM	NM	2.91	2011,[3]
$\pi 282^2 \times$NM	$\pi 75^2 \times$NM	N/O	Ring	W/O/N	S	250	23.24	NM	NM	0.2#	1.32	2005,[13]
NM	NM	N/O	Double Spiral	N	S+F	250	840	NM	NM	NM	-	2010,[4]
3240×1110×0.33	1350×370×0.21	N/O	Meander	N	F	250	90.73	NM	4.336	NM	0.181	1997,[85]
1000×1000×0.7	330× 330×0.2	N/O	Meander -Spiral	N/O	F	250	18.64	NM	18#	0.22	0.171	2012,[15]

Values of time constant (TC) and temperature uniformity are reported at different temperatures compared to the power

Table 2.2: Summary of various reported microhotplates (N = Silicon Nitride, O = Silicon dioxide, S = Simulation study,F = Fabricated results and NM = Not Mentioned)

Memb. Dimen. (µm × µm × µm)	Heater Dimen. (µm × µm × µm)	Memb. material	Heater type	Insulat. mat.	Sim. or Fab.	Opera. Temp. (°C)	Power (mW)	Deflection (μm)	TC	Temp. Uniformity (K/μm)	FOM @250°C ($\frac{mW}{1000\mu m^2}$)	Year,Ref.
640×640×1	240×240×0.34	O/N/O	Loop	O	S+F	250	12.43	NM	NM	NM	0.215	2004,[61]
1000× 1000×0.21	500×500×0.23	N	Double Spiral	NM	S+F	250	34.1	NM	5	0.05#	0.136	2004,[121]
NM	100× 100×0.15	PI	Double Spiral	PI	S+F	300	14.8	NM	NM	NM	-	2008,[52]
NM	NM	AlGaAs/GaAs	Double Spiral	None	F	250	34.3	NM	4.1	NM	-	2008,[50]
400×400× NM	100×100× 0.34	Si/O	Meander	O/N	F	250	8.1	NM	~1	NM	0.81	2009,[30]
NM	NM	Si/O	Meander	None	S+F	800	NM	45	NM	NM	-	2009,[28]
1100×1100× 0.8	480×480× 0.2	N/O	Parallel-Meander	O/SiC/O	S	450	NM	NM	NM	NM	-	2011,[7]
NM	NM	N/O	Meander	None	S+F	250	16.9	NM	NM	NM	-	2011,[14]
500×500 × 1	$\pi 55^2\times$ 0.2	O/N/O	Circular	O	F	250	15.3	2.5	NM	NM	1.6	2008,[54]
250×100× 1	NM	O	Meander	None	S	200	22	NM	NM	NM	-	2012,[51]
200×200× NM	NM	O	NM	Al	S+F	250	35	NM	0.6	NM	-	1993,[63]

Values of time constant (TC) and temperature uniformity are reported at different temperatures compared to the power

Table 2.2: Summary of various reported microhotplates (N = Silicon Nitride, O = Silicon dioxide, S = Simulation study,F = Fabricated results and NM = Not Mentioned)

Memb. Dimen. (µm × µm × µm)	Heater Dimen. (µm × µm × µm)	Memb. material	Heater type	Insulat. mat.	Sim. or Fab.	Opera. Temp. (°C)	Power (mW)	Deflection (μm)	TC	Temp. Uniformity (K/μm)	FOM @250°C ($\frac{mW}{1000\mu m^2}$)	Year,Ref.
NM	NM	O	NM	O/N/O	S+F	250	4.8	NM	1	NM	-	2002,[86]
410×410×1.3	NM	O/N	Meander	None	S+F	250	8.6	NM	$<5^{\#}$	NM	-	2011,[16]
1000× 1000× 1.8	80×80×NM	O/SiC/O	Plate	N	F	250	20	NM	NM	NM	3.13	2001,[91]
$\pi 1500^2 \times 20$	250×400×1	Al_2O_3	Meander	None	F	450	90	NM	$80^{\#}$	NM	-	2008,[92]
1800× 1800× 275	NM	LTCC	Double Spiral	None	S+F	400	630	NM	NM	NM	-	2004,[122]
$\pi 280^2 \times 2$	$\pi 75^2 \times 0.3$	O	Concentric	W/Si	S+F	250	11.83	8.5	$10^{\#}$	$0.33^{\#}$	0.669	2006,[59]
$\pi 150^2 \times 2$	$\pi 12^2 \times 0.3$		Rings			250	4.77	2.5	$2^{\#}$	NM	10.54	

Values of time constant (TC) and temperature uniformity are reported at different temperatures compared to the power

3

Modeling and Simulation of Microhotplate

3.1 Introduction

A number of microhotplate performance parameters can be tailored by parameters such as Membrane to Heater Ratio (MHR), material choices and dimensions. Employing an optimized value of these parameters helps the microhotplate designer in realizing an efficient microhotplate design. Apart from performance, design cycle time is also a critical parameter, which can be minimized by restricting the design to key performance parameters with the help of appropriate assumptions. In order to limit the number of parameters and to arrive at a proper assumption, we have restricted our-self to gas sensing

area. Therefore, motivation of this chapter is to identify the optimum performance parameters and to verify the assumptions made for an efficient microhotplate designed for gas sensing application.

In order to design a microhotplate which can perform efficiently over the desired temperature range, the first investigation is carried out to identify the individual loss components, because the total power consumption depends primarily on the significant part of loss mechanism. In the next study, we focus on the selection of a proper Membrane to Heater Ratio (MHR), which is critical for the performance of square membrane. The key parameters such as power, temperature uniformity, mechanical reliability and response time are affected by the MHR value. Based on these studies we suggest a new method for the performance improvement, in which the performance of a microhotplate is enhanced by employing an insulation layer of optimized dimensions. For finding the optimize dimensions of insulation layer, a steady state mathematical model is developed. In order to simplify the modeling approach, the membrane area is approximated by strip approximation.

The thermal time response of microhotplate is affected by thermal resistance of membrane. In the proposed method, the optimized dimension of insulation layer selectively alters the membranes thermal resistance. In order to analyze the effect of insulation layer dimension on thermal time response, a lumped element model is developed.

While developing the analytical model to find the optimized insulation layer dimensions, the membrane area is approximated using a strip approximation. This approximation underestimates the membrane area, hence, it directly affects the modeling accuracy. Therefore, for minimizing the area error, a triangular approximation approach is suggested. This approximation is then employed in developing a simple mathematical model for power consumption estimation. However, the developed model can be employed for the quick design optimization also.

All simulation studies are designed with a microhotplate which consists of a multilayer stack of heater and membrane layers supported by a micromachined substrate. Membrane is realized using a stack of SiO_2 and Si_3N_4 films. The microheater is designed over a 1.4 μm thick membrane consisting of thermally grown SiO_2 and CVD Si_3N_4. Starting

TABLE 3.1: Material properties used for simulations [21]

Material	Si	Si_3N_4	SiO_2	Pt
Density (kg/m^3)	2.3×10^3	2.7×10^3	2.1×10^3	21.4×10^3
Thermal Conductivity (W/mK)	157	24	1.42	71.6
Dielectric Constant	11.9	8.0	3.9	0.0
Specific Heat (J/KgK)	703	170	1.0×10^3	133
Electrical Conductivity (s/m)	1.4×10^3	10×10^{-3}	1×10^{-10}	8.9×10^6
Young Modulus (MPa)	1.3×10^5	2.2×10^5	7×10^4	1.4×10^5
Poisson Ratio	0.27	0.27	0.17	0.35
TCE (K^{-1})	2.5×10^{-6}	1.6×10^{-6}	5×10^{-7}	9.7×10^{-6}

material is a (100) silicon wafer and after cleaning, a 1 μm thick thermal oxide is grown over it. Subsequently, a 0.4 μm thick nitride was deposited on it using LPCVD process. By employing a stacked layers of silicon dioxide and nitride membrane, the thermally generated stress are reduced [16, 84]. Sputtered platinum is widely used as a heating material because of its excellent stability at relative high temperatures [68]. A 0.12 μm thick platinum is deposited onto the membrane using the sputtering process and platinum is patterned using the microheater mask. To realize a square membrane, the bulk micromachining is employed to remove the bulk of silicon using anisotropic etching. On the other hand, for realizing the bridge membrane, front etching is carried out using wet anisotropic etching. This step will release oxide/nitride composite membrane. All FEM simulations are carried out using CoventorWare [21]. And simulations employ tetrahedron meshing for the entire structure, a different mesh element sizes are selected for various layers in-order to get a good accuracy in a reasonable simulation time. Table 3.1 summarizes the material properties used for the study [21]. These simulation settings are employed for all the studies, unless otherwise specified.

3.2 Power Loss Components of Microhotplate- A Simulation Study

To simplify the microheater design, assumptions are often made regarding the significance of a particular loss component while neglecting other components. However, the

validity of such assumption also depends upon the application area or the operating temperatures. For example, an application area where the operating temperature are less than 300°C, convention losses can be neglected without adding significant errors to the power consumption estimation. Whereas, for an application with higher working temperatures, the same assumption regarding convection losses might lead to significant errors in power consumption, this is because of the increase in the convention losses at higher temperatures. Therefore, proper assumptions will lead to correctly predict the output of a microheater and hence will improve overall performance of the design. Moreover, once the contribution of each power component is identified, it will enable us to evolve with a strategy to overcome the losses. Further, in the microhotplate design insulation layer is employed, the investigation is extended to analyze the effect of this layer on the contribution of individual heat loss component. Where, we have considered the effect of a thin nitride insulation layer on the conduction, convection and radiation part of thermal losses. Such a study is important since it would predict the increased power demand exclusively due to the insulation layer. Fig 3.1a shows the layout of the microheater. For this study a new R-shaped microheater geometry is designed mainly to achieve uniform heating by varying the line widths of the R shape heater. The line width is kept maximum at the center to avoid the formation of any hotspot. To insulate the heater geometry from other application domain a 0.4μm of silicon nitride is deposited over the patterned microheater. The 3-D model of the generated structure is shown in Fig. 3.1b.

Since the outcome of the simulations are affected by several parameters such as the value employed for material thermal conductivities, emissivities. Therefore, a discussion is presented for the major consequences of the assumptions involved and infer some possible solutions to predict results more accurately.

The various heat loss paths which contribute in the form of convective, radiative and conduction losses are identified in the Fig. 3.1c. For carrying out the convection and radiation studies, the values of heat transfer coefficient and the emissivity are taken from the literature. The convection losses from the front side as well as back etched part are considered and convective loss coefficient (h) value of 250W/m^{2}K for the top side and 125W/m^{2}K for bottom side is used. The emissivity (ϵ) value is process dependent and

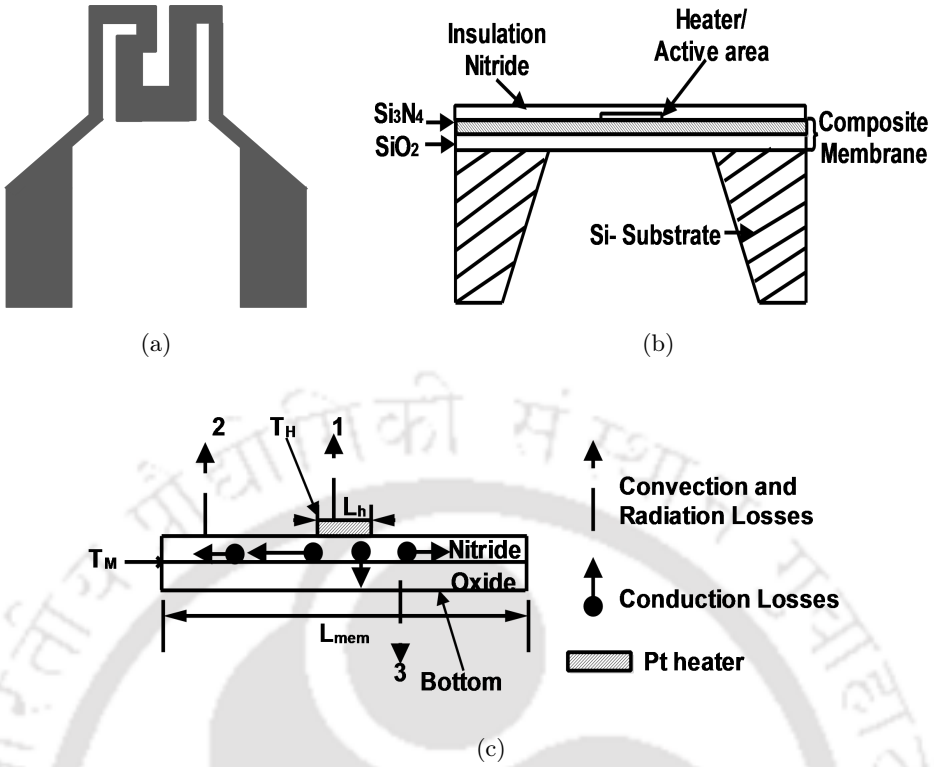

FIGURE 3.1: (a) Microheater layout, (b) 3D Structure (Cross-sectional view) and (c) thermal loss paths. Temperature at the heater edge is denoted as T_H, temperature at the membrane edges are denoted as T_M, membrane length and heater length are denoted as L_{mem} and L_h respectively.

its values ranging from 0.2 – 0.88 and 0.6 – 0.7 have been reported for silicon dioxide and silicon nitride respectively [6] [14], [123]. In this study, the value of h and ϵ are chosen to represent the worst case scenario [124] for gas sensing application. The values of effective emissivity for silicon dioxide and silicon nitride are chosen to be 0.7 and 0.88. The thermal conductivity and emissivity of material depends on deposition method, operating temperature, thickness, however, the effect of them is ignored for simplicity. Similarly, the convection coefficient value is also temperature dependent, however, a constant value is assumed in this study. For lower operating temperatures it is often assumed that the convection and radiation losses are negligible whereas conduction losses are a major source of power loss. But at higher temperature operation, the convection heat losses through surrounding air will be a important component of total power losses. The radiation losses will also becomes a major component as the membrane temperature increases. The contribution of radiation and convection part depends on the convection heat transfer coefficient and emissivity values, operating temperature and also on the

area of the microheater [13]. The simulations are carried out for the membrane part only and hence this study will not account for the conduction losses in the bulk silicon as well as the convective and radiative losses from the bulk faces. The following are the major consequences of the assumptions involved.

- The simulation does not consider the bulk silicon losses and therefore in actual experimental result the losses will be higher.
- Due to the constant convection coefficient assumption, the heat losses from the back of the structure will be overestimated. The die will be mounted on a thermally insulated base of a TO-8 header to result in a closed cavity structure, and hence the actual convection losses will be slightly lower compared to simulated values.
- While doing the parametric study by sweeping the voltages, the value of h is also expected to change with temperature. Since a constant value of h is used throughout the simulations, inaccuracies will be present in convective power losses especially at higher temperatures.

While simulating the microhotplate the ambient temperature is kept at 27°C and the resistance of the microheater at ambient temperature is 30.5Ω. The temperature dependent heater resistance is calculated using the linear equation which is given as,

$$R_T = R_0(1 + \alpha\Delta T) \tag{3.1}$$

The linear equation (3.1) is usually used for the resistance calculation. But it will results in significant errors especially at higher operating temperatures leading to an underestimation of power losses. Hence, for accurately calculating the change in resistance at this wide temperature range, the Callendar – van Dusen equation is employed.

$R_T = R_0(1 + A\Delta T + B\Delta T^2 - 100C\Delta T^3 + C\Delta T^4)$

Where,

R_T = Resistance at temperature T,

R_0= Resistance at room temperature,

and $A = \alpha + \frac{\alpha\delta}{100}$, $B = \frac{-\alpha\delta}{100^2}$ and $C = -\frac{\alpha\beta}{100^4}$.

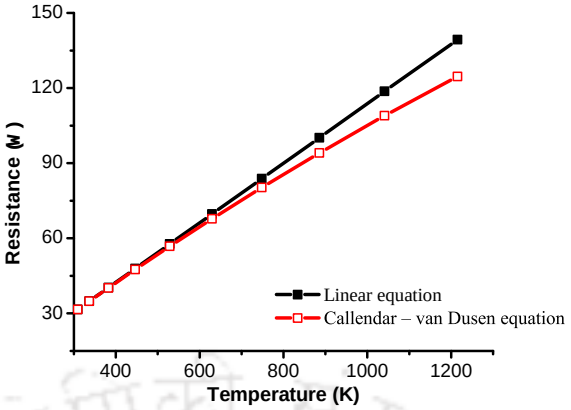

FIGURE 3.2: Resistance estimation with linear and Callendar – van Dusen equations

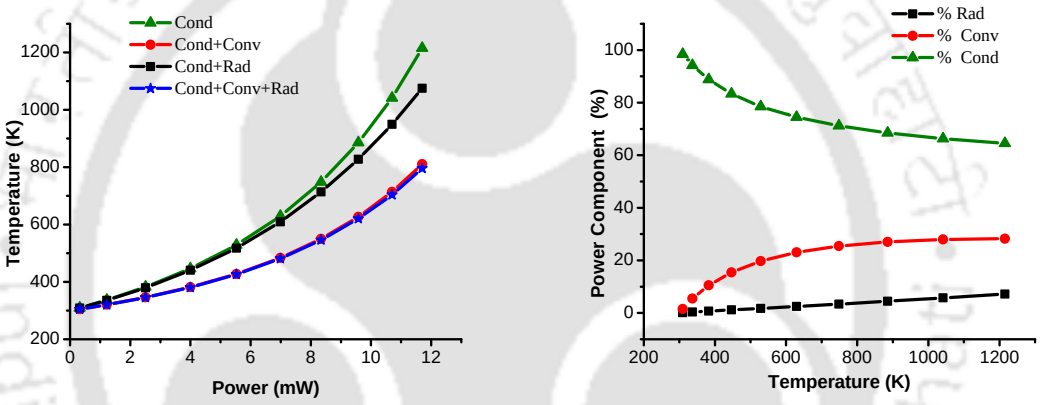

(a) Power Component (b) Percent power component

FIGURE 3.3: Individual power components without nitride insulation layer

For temperature greater than 0°C the coefficient β and hence C will be zero, resulting in equation

$$R_T = R_0(1 + A\Delta T + B\Delta T^2) \tag{3.2}$$

This equation is valid till 1000°C and α, β, δ values are obtained experimentally. For this study, $\alpha = 3.85e-3°C^{-1}$, $\delta = 1.5°C$ are considered [114]. A comparison of resistances calculated by both the equations is shown in Fig. 3.2. It may be noted that the linear equation overestimate the resistance values by 12% at 1200K temperature.

3.2.1 Results and Discussion

For all the studies involved, an extruded meshing scheme is used. The voltages are varied from 0.1 to 1V and the applied potential will cause joule heating in the microheater structure. Individual power components without the nitride insulation layer is presented first in Fig. 3.3. The power delivered and the corresponding temperature achieved under different components are plotted. As expected, the achievable temperature will be higher for any given power, when the convection losses are neglected and only the conduction losses are considered. But in reality with all the three losses present, the achievable temperature will be reduced. The conduction component will be the highest contributor to power loss. The convection losses will be second highest contributor $(20-30\%)$ of the total power. Till 1200K, the radiation loss was the least contributing part of power loss components. For achieving a target temperature of 800K, the total power needed is 11.7mW out of which conduction part is 8.03mW and convection part is 3.52mW.

With the deposition of nitride layer over the microheater, the conduction losses in the insulation layer also will be added to the total losses and the results are presented in Fig.3.4. Assuming a conduction loss only situation, the highest temperature achievable was reduced from 1200K to 925K when the nitride layer is added. With all loss mechanisms present, the microheater has achieved a temperature of 619K for an applied voltage of 1V. From Fig. 3.4b it can be seen that the dominant power loss is due to conduction but at higher temperatures (beyond 450K) the convection losses also become significant. For achieving a target temperature of 619K, the total thermal power required is 15mW in which the conduction part is 10.2mW, convection loss is 4.63mW. The radiation loss component remains insignificant.

The results of individual power components with and without nitride insulation layer are summarized in Fig. 3.5. With a nitride layer over the heater, the conduction loss has increased from 8.03mW to 10.2mW for an applied voltage of 1V and the corresponding convection loss has increased from 3.52 to 4.63mW. The highest achievable temperature with a constant 1V supply is 275°C lower in comparison with the same heater with no nitride layer. The major reason for this reduction in temperature is the conduction and

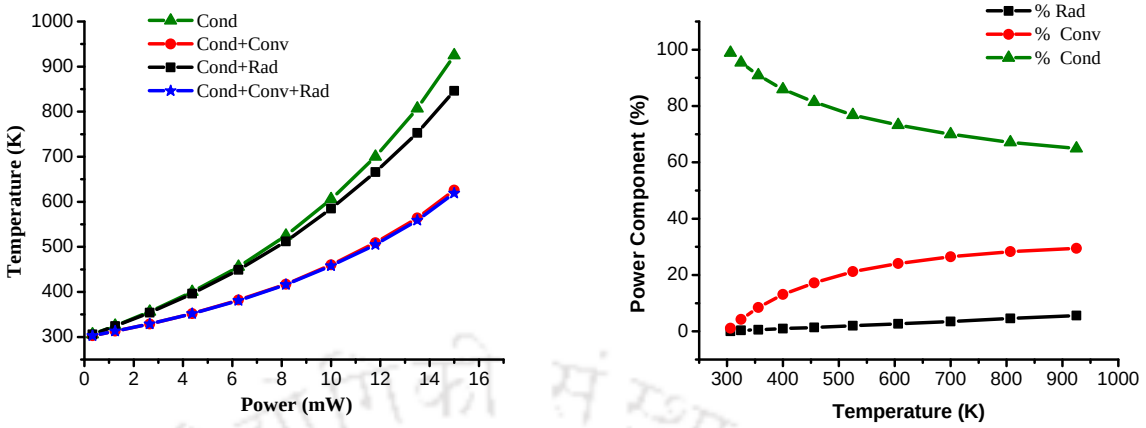

(a) Power Component (b) Percent Power Component

FIGURE 3.4: Individual power components with nitride insulation layer

convection losses involved in the nitride layer. As expected the radiation losses in both the cases were almost the same and contributed least to the overall power loss.

Theoretically the total power can be computed by equation [85]

$$P_{Total} = \frac{4 * K_{eff} A_c * \Delta T}{L} + hA_s\Delta T + \epsilon\sigma A_s(T^4 - T_a^4) \tag{3.3}$$

where K_{eff} is the effective thermal conductivity of the composite membrane $K_{eff} = \sum_{i=1}^{n} u_i v_i K_i$ [112] where u and v are the ratio of layer to total membrane thickness for width and thickness, respectively and A_c is the area of cross-section of the membrane. A_s is the heater area, h is the convection coefficient, ϵ is the emissivity and σ is Stefan constant.

For achieving a 620K temperature without the top nitride, 9.58mW power is required when all the loss mechanisms are present. It is very close to the theoretically calculated value of 9.63mW, using equation 3.3 with $K_{eff} = 7.87\frac{W}{mK}$ .Similarly for achieving 620K with a top nitride present, a K_{eff} value of $11.45\frac{W}{mK}$ is employed and equation 3.3 results in a power of 15.77mW which is close to the value of 15mW obtained using simulations. The convection loss can be minimized by reducing the membrane area but by doing so the conduction losses in the bulk silicon will increase [6]. Also, the conduction losses in the membrane can be reduced by reducing the thermal mass of the membrane, but this

may leads to mechanical stability issues arising due to the generation of thermal stress during operation.

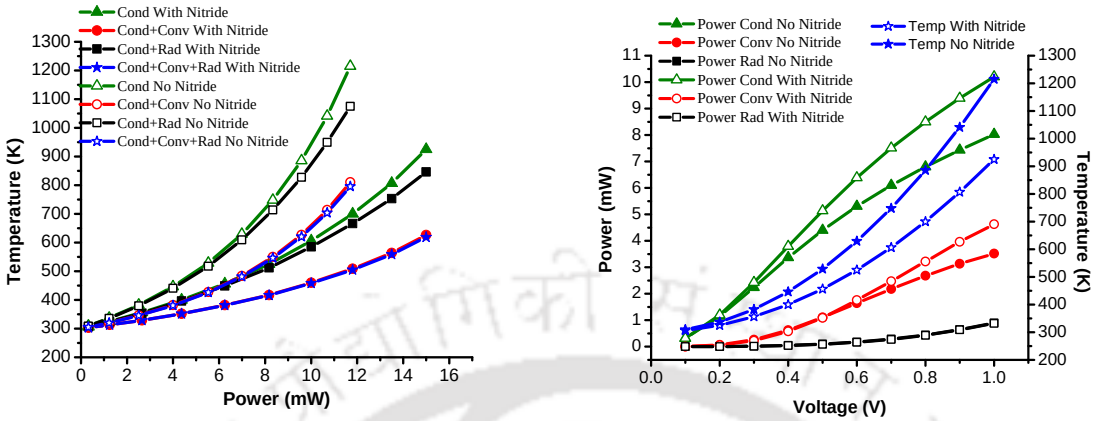

(a) Power Component (b) Comparison of Power and Temperature

FIGURE 3.5: Comparison of individual power components with and without nitride insulation layer

3.3 Effect of Membrane to Heater Ratio - A Simulation Study

For a square membrane, it has been reported that the power consumption can be improved by keeping a optimum Membrane side length to Heater side length Ratio (MHR) [28, 52, 79]. Various previous studies have also identified the influence of MHR on other performance parameters as well [5, 79] but a detailed investigation of the effect of MHR on all the key performance parameters is still lacking. An analysis of the effect of MHR on the performance parameters namely power, temperature uniformity, vertical deformation and thermal time response has been carried out to identifying the tradeoffs that exists between these performance parameters in a systematic manner.

3.3.1 Results and Discussion

The effect of MHR on the performance parameters are evaluated in the following manner: dimension of the membrane is varied from 700 μm $\times$ 700 μm to 200 μm $\times$ 200 μm, while keeping the heater area (100 μm $\times$ 100 μm), die size, maximum operating temperature

(694K), membrane thickness and composition constant. Due to the large thermal capacity of the bulk substrate, die edges are assumed to be at room temperature [112]. To investigate the vertical displacement due to the thermally generated stress, electrothermomechanical simulations are carried out. At the desired operating temperature of 694K, contribution from the radiation losses component can be safely ignored [8, 65]. Moreover, since conduction is the major component of thermal loss mechanism [79], the simulations are carried out for conduction losses in the device and to the air.

Effect of MHR on the Power Consumption

The power consumption of the microhotplate depends on thermal losses. In order to minimize the thermal losses in the square membrane it is required to optimize the dimensions of membrane. As the MHR increases, the power required to reach a particular temperature reduces, this is due to the increased thermal resistance of the membrane.

Conduction losses to the surrounding air are calculated theoretically as [91]

$$P_{Air} = 4 \cdot \pi \cdot K_{air} \cdot R_h \cdot (T_h - T_{amb}) \tag{3.4}$$

where, K_{air} is the thermal conductivity of air in W/mK, R_h is radius of the heater, T_h is the operating temperature and T_{amb} is ambient temperature. The conduction losses to air are dependent on the heater area and the maximum operating temperature. Hence the conduction losses to air will be constant for all values of MHR. With $R_h = 56\mu$m and $K_{air} = 0.026\ \frac{W}{mK}$ [106], the conduction loss to air obtained is 7.21 mW. The total power consumption of the membrane is the sum of conduction loss to material ($P_{Cond-simulation}$) and conduction loss to air (P_{air}) as given in Eq. (3.5).

$$P_{total} = P_{Cond-simulation} + P_{Air} \tag{3.5}$$

The power consumption with MHR variation is shown in Fig. 3.6. The power consumption to reach an operating temperature of 694K has been reduced from 33.23mW to 18.6mW when the MHR is increased from 2 to 7. This is a significant amount of power

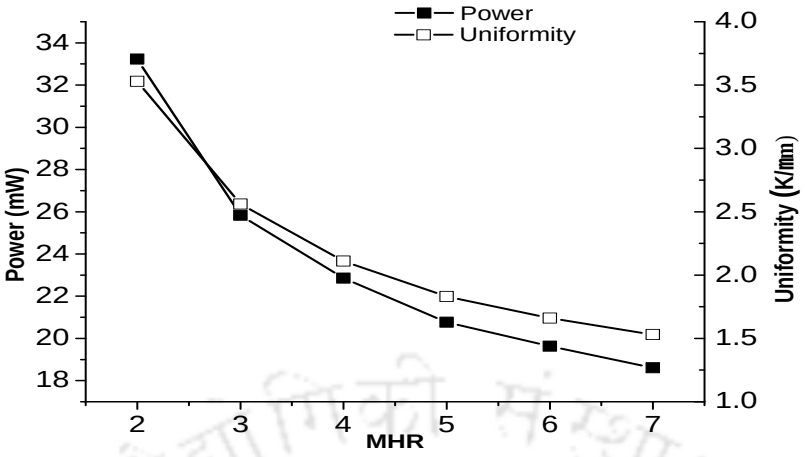

FIGURE 3.6: Effect of MHR on power and uniformity

saving for square membrane. The saving in power with a large MHR has been observed experimentally [79]. With increased MHR, the distance between sink (bulk silicon) and source (heater region) increases, hence the power consumption reduces. However, as depicted in Fig. 3.6, power saving achieved by increasing the MHR tends to saturate, beyond MHR of 5. Hence, increasing the MHR beyond 7 will not be beneficial. The MHR also affects yield, and square membranes with large MHR has the lowest yield [105].

Effect of MHR on the Temperature Uniformity

Temperature uniformity is an important performance parameter, and it is affected by heater geometry. Heater geometry, in-turn is affected by the resistivity of membrane [56]. A high resistivity of membrane will ensure reduced conduction loss path to the membrane edges which act as a heat sink. The effect of MHR on the temperature uniformity of the active area is shown in Fig. 3.6. The thermal losses by the edges of the membrane is reduced when the MHR is increased and thereby the temperature uniformity of the microhotplate is increased. As a result, the temperature difference between the center and the outer edges of microheater reduces. With MHR=7 an improvement of 56.65% is achieved compared to the temperature uniformity with MHR=2.

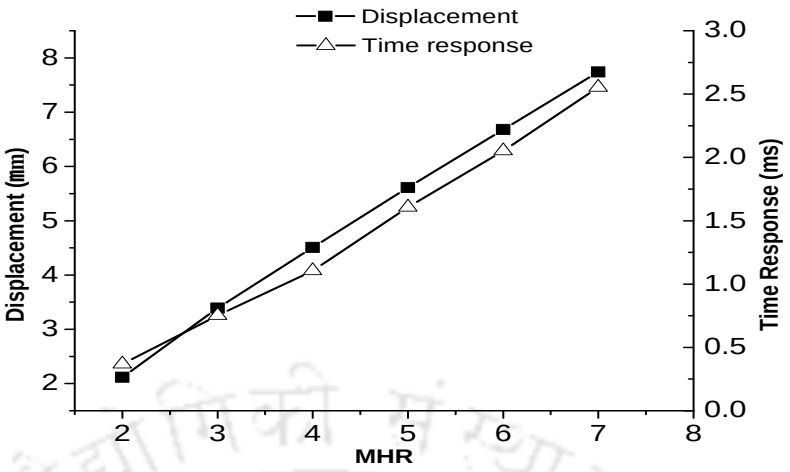

FIGURE 3.7: Effect of MHR on time response and vertical displacement

Effect of MHR on the Mechanical Deformation

Membranes are often composed of different material with different thermal expansion coefficient, because of which during operations, thermal stress and strains are produced and thereby resulting in the structural deformation. The internal stress of Si_3N_4 and SiO_2 layers is above 0.1 GPa which results in the buckling of membrane [82]. These buckling causes reliability problems in microheater and results in membrane damage by peel off or fracture/microcracks. Silicon nitride layers have large tensile stress and silicon dioxide layers are compressive. Hence by choosing an appropriate thickness of Si_3N_4 and SiO_2 layers, the internal stress can be balanced [16, 84]. Many articles have reported the use of Si_3N_4/SiO_2 or even $Si_3N_4/SiO_2/Si_3N_4$ composite membranes [62, 96]. Moreover, in these composite membrane, intrinsic stress of the silicon nitride can be varied by using silicon rich nitride [82]. The resulting stress in a composite membrane can be estimated by [61]

$$\sigma_{res} = \frac{t_{SiO_2}\sigma_{SiO_2} + t_{Si_3N_4}\sigma_{Si_3N_4}}{t_{SiO_2} + t_{Si_3N_4}} \tag{3.6}$$

where, σ_{res} is the total stress of the composite layer stack, $t_{SiO_2}, t_{Si_3N_4}$ are the thickness of oxide and nitride layer respectively, and $\sigma_{SiO_2}, \sigma_{Si_3N_4}$ are the stress of oxide and nitride layer respectively. Using the value of thermal stress for thermal oxide and nitride

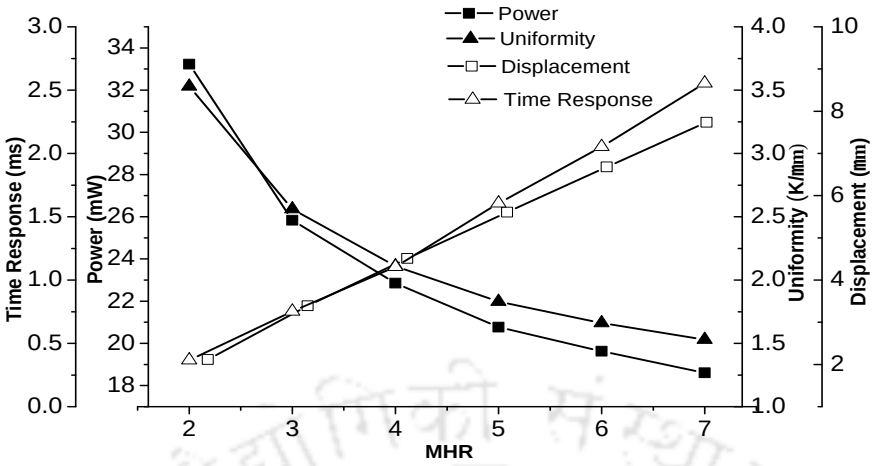

FIGURE 3.8: Comparison of the effect of MHR on power, uniformity, vertical displacement and thermal response time

as –230 MPa and 250 MPa [15]. This results in a resultant compressive stress of 92 MPa which lies in the range of –0.1 GPa $< \sigma_{res} <$ +0.1 GPa is required for good mechanical reliability in microhotplates [82]. As shown in Fig. 3.7, with an increase in MHR, the vertical displacement increases from 2.11 μm (with MHR=2) to 7.74 μm (with MHR=7). These results indicate a clear tradeoff between power, temperature uniformity and vertical displacement. A smaller membrane size will reduce the vertical displacement, but it will also adversely affect the power consumption and temperature uniformity.

Effect of MHR on the Time Response

Thermal response time of microhotplate is govern by the thermal resistance of the membrane [83] and is calculated as the time to reach 63.2% of the final value. As shown in the Fig. 3.7, rise time of the microhotplate has been increased from 0.37 ms to 2.55 ms for MHR=2 and MHR=7 respectively. As MHR increases, the thermal capacity of membrane increases and thereby the response time is also increased proportionately. In order to have a fast response time, it is desirable to use a small MHR. This requirement contradicts with power and temperature uniformity parameters. Hence, an optimum MHR has to be chosen to achieve the best possible time response, without compromising temperature uniformity and power consumption.

A large MHR can be used for improving the power consumption and temperature uniformity of the microhotplate. However, with increased MHR the mechanical reliability and time response deteriorates. The tradeoff that exists among these performance parameters is plotted in Fig. 3.8. Depending upon the application domain, where these microhotplate will be employed, suitable MHR can be selected by considering the prime performance requirement. For example, for a gas sensing application, temperature uniformity and time response are important performance parameters. By selecting MHR=4, time response can be improved. With the improved time response, pulse mode operation of the microheater will allow further power saving.

3.4 Insulation Layer Optimization - Model and Simulation

It has been already established that in microhotplates, often an insulation layer is required to separate the thermal domain (microhotplate) from its application domains such as gas sensor. While investigating the microhotplate for determining the individual power loss components, we noticed that the blanket deposition of a thin insulation layer increases not only the conduction losses but also the convection losses. The deteriorating effect of blanket insulation layer deposition on microheater performance is also reported by Neda et al. [108].

Investigation further reveals that a blanket deposition on insulation layer alters the thermal conductivity of membrane, which causes an increase in power consumption and deterioration of thermal uniformity. Hence, in this section, we explore the effect of optimized insulation layer dimensions on the microhotplate dimensions and Fig. 3.9 depicts the optimization approach.

Among the various reported insulation layer materials, we investigate the Silicon Nitride as the insulation layer because of its relative ease of fabrication and good electrical insulation. In addition, Silicon Nitride insulation layer can serve the dual purpose of providing good temperature uniformity and good thermal efficiency between the microheater and gas sensor. We focus on improving temperature uniformity, by increasing the thickness of the insulation layer. Such an approach will be advantageous even when the membrane

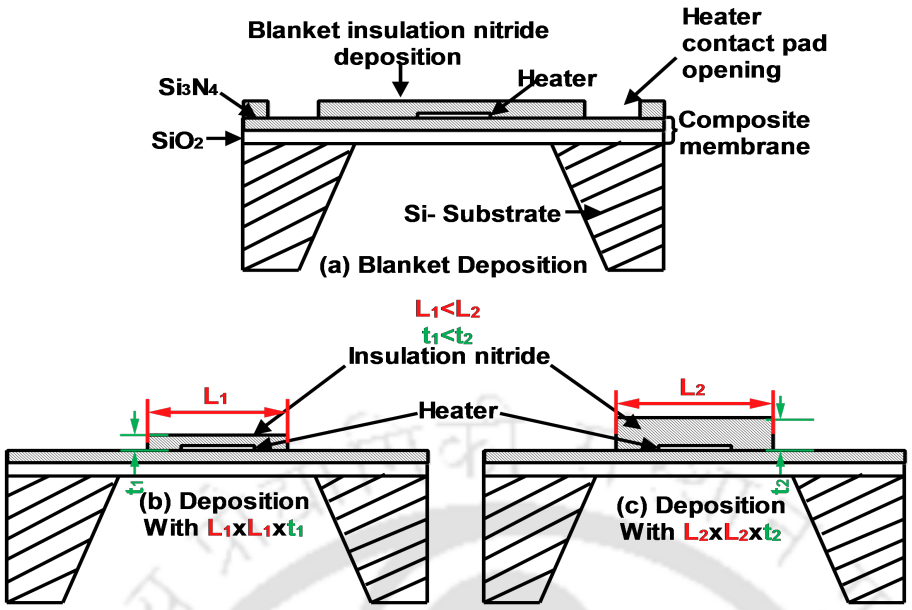

FIGURE 3.9: Optimization of insulation layer (a) blanket insulation layer deposition, (b)-(c) finding the optimum insulation layer dimension

material composition and dimensions are changed, because, only the dimensions of the insulation nitride layer needs to be varied to obtain the desired temperature uniformity. On the other hand, when one targets to achieve the temperature uniformity, by optimizing the heater geometry, many parameters such as the shape, thickness and material properties of both membrane and insulation layer need to be taken into account.

When a thick nitride layer is employed as an insulation layer, the improvement in the temperature uniformity is also accompanied by increased power consumption and thermal time response. Considering these tradeoffs, an optimization of nitride layer dimensions in order to achieve good electrical insulation as well as temperature uniformity is investigated for the first time. Optimization of insulation nitride dimensions via FEM simulations is a very time consuming task. Hence, our main objective is to develop an analytical model for the optimization of the heat spreading nitride dimensions. The advantage of the developed model is its modular nature, because of which the power losses in insulation layer and membrane can be calculated separately. Awareness of the individual power losses in the design phase can be advantageous in designing an optimum microhotplate. It allows to optimize the dimensions of membrane and heat spreading film separately and one could meet the stringent design constrains. Apart from being modular, the model inherit the advantage of being faster than FEM simulations. The

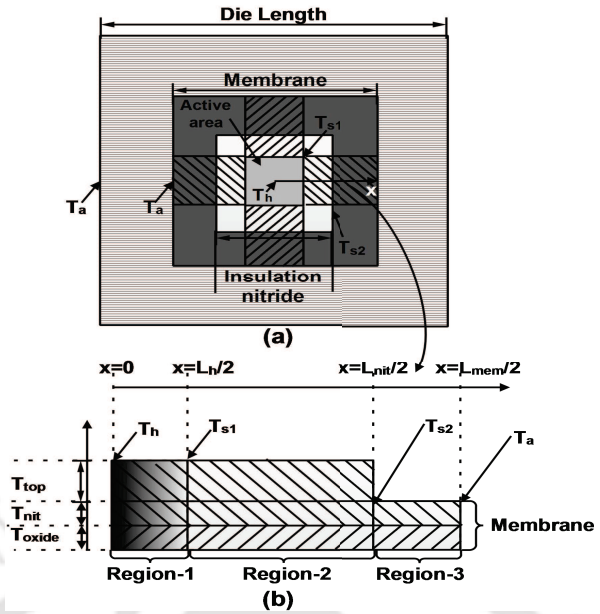

FIGURE 3.10: (a) Top view of a die consisting of membrane (dark gray), active area (light gray) and insulation nitride (white). (b) Cross-sectional view of one strip showing different layers and regions, T_{top} is the insulation nitride thickness and T_{nit}, T_{oxide} are the thickness of nitride and oxide layer in the membrane.

analytical model results will be compared systematically with FEM simulations, for determining the effect of insulation layer dimensions on power, temperature uniformity and maximum achievable temperature.

3.4.1 Steady State Modeling of Square Microhotplate

It is known that a meander microheater suffers from hotspots and causes a non-uniform temperature distribution in the active area [5]. In order to increase the accuracy of the thermal modeling, a non-uniform thermal profile of the meander microheater is considered. When an insulation nitride layer is blanket deposited over the membrane, it increases the thermal conductivity of whole membrane. This increased thermal conductivity will cause an increased thermal loss as well as temperature non-uniformity. However, by optimizing the dimension of the top insulation layer, the thermal conductivity can be increased only in selected part of the membrane, i.e., in the active area, thereby, improving the power consumption and temperature uniformity. Moreover, this will not add any complexity to the existing fabrication steps.

Conduction, convection and conduction losses to air are the primary loss mechanisms as the radiation losses are not significant [8, 65] in the gas sensing temperature range of interest. However, for completeness, the effect of radiation is also included in the model. The top view of a die is shown in Fig. 3.10a. The die consists of a membrane which provides the platform for microheater and insulation layer over it. Instead of considering the thermal losses in the whole membrane, the membrane is modeled into four strips (shown as hatched regions) and it is assumed that the heat losses are dominated only in these strips. The cross sectional view of a single strip is magnified in Fig. 3.10b. The membrane consists of SiO_2 and Si_3N_4 layers. Another layer of Si_3N_4 at the top acts as the insulation (heat spreader) layer. Due to the thermal losses in the membrane, the temperature at the edges of microheater (T_{s1}) will be lower than the temperature at the center of membrane (T_h). Similarly, the temperature at the edges of insulation layer (T_{s2}) will be lower than the active area. Hence, the strip is further divided into three regions. The first region (x = 0 to x = $L_h/2$) is heater region, which includes joule heat generation from the platinum heater. The region 2 (x = $L_h/2$ to x = $L_{nit}/2$) consists of the heat spreader film with no heat generation. Region 3 (x = $L_{nit}/2$ to x = $L_{mem}/2$) consists of membrane only and has no heat generation. By applying energy balance at the interfaces of these regions, intermediate temperatures are calculated. It may be noted that the region 2 also consists of contact electrodes and due to their finite resistance they will also have joule heating effect. However, for simplicity, this effect is neglected in the model. Once the temperature at each node is calculated, this model will be used to calculate the heat losses contribution from the membrane and top nitride separately. This approach makes the modeling flexible and modular.

Due to the large difference between the length (517μm) compared to the thickness (<10μm) of the membrane, the 3D geometry of the membrane can be approximated as 2D. Fig. 3.11(a) shows the contour plot of the square membrane and the associated temperatures. The membrane has symmetrical isotherms and the isotherm in a single strip is expanded in Fig. 3.11(b). It can be noted that there is a large temperature variation in the X direction, whereas, the temperature variation in Y direction is small, hence the model can be further simplified from 2D to a 1D problem. Hence, the governing equation [112] is given as,

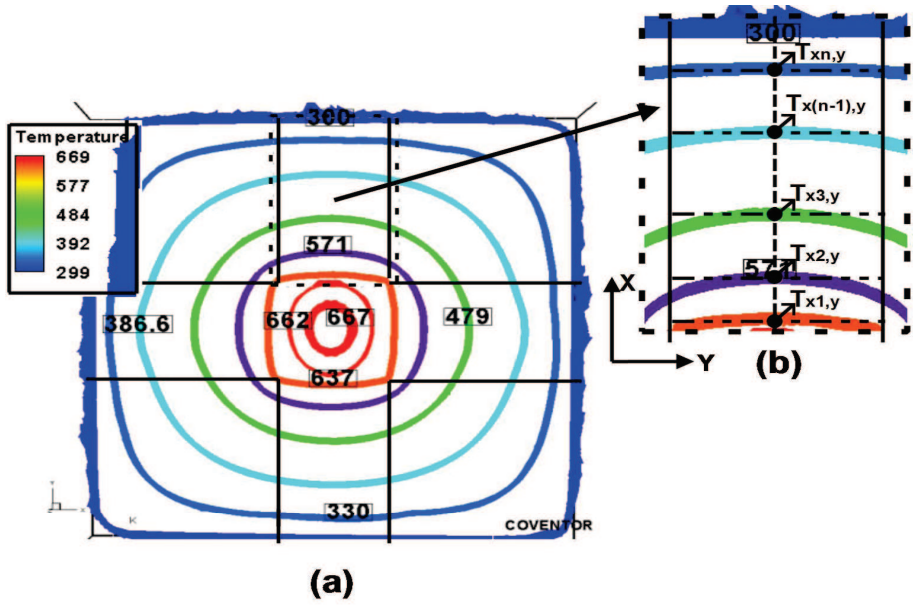

FIGURE 3.11: (a) Temperature contour plot of membrane using FEM simulations. (b) Expanded contour plot in a single strip, where $T_{x_n,y}$ is the temperature at (x_n, y) location and $T_{x_n,y} << T_{x_1,y}$.

$$\rho c_p \frac{dT}{dt} = \nabla \cdot (K_{eff} \nabla T + K_{air} \nabla T - q_h - q_r) + \frac{P}{V} \tag{3.7}$$

where ρ is the mass density, c_p is the specific heat, T is the temperature, K_{eff} is the effective thermal conductivity of the membrane, ∇T is the temperature gradient, K_{air} is the thermal conductivity of air, V is the volume, P is the input power, q_h and q_r are the convective and radiative heat losses respectively. The thermal conductivity of the three regions depends on the direction of thermal heat transfer. That is, the thermal conductivity of the composite membrane is calculated by considering either the in-plane or cross-plane thermal conductivity. Due to the smaller thickness of the membrane as compared to the lateral dimension, the temperature along Z-axis is assumed to be isothermal. Also, material properties are assumed to be temperature independent and thermal contact resistance between the different layers are not taken into account, both in simulation and theoretical modeling. The model is initialized by the calculation of thermal resistance of the membrane from the lumped model. From the thermal resistance, the power required to attain a desired temperature T_h is computed. Next, the proposed model is

applied for evaluating intermediate temperatures. With the intermediate temperatures known, the power consumption can be calculated more accurately.

In microhotplates, conduction losses in the membrane cannot be neglected. However, depending on microhotplate operating temperature, convection and/or radiation can be omitted. Hence, the model is developed for three cases. In first case, model is developed considering conduction and convection loss mechanisms and neglecting radiation losses. In case 2, the conduction and radiation losses are present. In case 3, model is developed when all the three losses are present.

Case-1: With Conduction and Convection Losses Present

The convection coefficient is assumed to be constant and since the die will be mounted on a Transistor Outline (TO) package, the convection losses from bottom of the membrane is not considered. However, the model can be easily extended, for including the effect of convection from both sides. The volumetric thermal energy balance differential equations for heat conduction and convection in the three regions are given as follows,

The balance of conduction and convection per unit volume across the region 1 can be written as,

$$\frac{d^2T_1}{dx_1^2} - \frac{hA_{s1}(T_1 - T_a)}{K_{eff1}V_1} + \alpha_1 = 0, \ (0 \leq x_1 \leq \frac{L_h}{2}) \tag{3.8}$$

Similarly, energy balance for region 2 and 3, can be presented as,

$$\frac{d^2T_2}{dx_2^2} - \frac{hA_{s2}(T_2 - T_a)}{K_{eff2}V_2} = 0, \ (\frac{L_h}{2} \leq x_2 \leq \frac{L_{nit}}{2}) \tag{3.9}$$

$$\frac{d^2T_3}{dx_3^2} - \frac{hA_{s3}(T_3 - T_a)}{K_{eff3}V_3} = 0, \ (\frac{L_{nit}}{2} \leq x_3 \leq \frac{L_{mem}}{2}). \tag{3.10}$$

where $K_{eff1,2} = \frac{(T_{nit}+T_{oxide}+T_{top})}{((T_{oxide}/K_{SiO_2})+(T_{nit}/K_{Si_3N_4})+(T_{top}/K_{Si_3N_4}))}$,

$K_{eff3} = \frac{(T_{oxide}K_{SiO_2})+(T_{nit}K_{Si_3N_4})}{T_{nit}+T_{oxide}}$, $\alpha_1 = \frac{P}{K_{eff1}V_1}$, h is the convection coefficient, A_s is the surface area of the region, L_h, L_{nit}, and L_{mem} are side length of the microheater, top nitride, and membrane respectively. V_1, V_2, and V_3 are volume of region 1, 2, and 3 respectively. Equations (3.8), (3.9), and (3.10) are the governing differential equation for the three regions of the strip. The temperature boundary conditions shown in Fig. 3.10, are as follows, T_h is the temperature of microheater at the center of membrane, T_{s1} is the temperature at the heater edges, T_{s2} is the temperature at the nitride edges, and T_a is the temperature at membrane and die edges. Solving the above differential equations with the boundary conditions results in the temperature profiles for the three regions and is given as,

$$\begin{aligned} T_1(x_1) = \frac{e^{-x_1\theta_1}}{\theta_1^2\lambda_1}\Bigg(& \left(e^{\frac{L_h\theta_1}{2}}-1\right)\left(e^{\frac{L_h\theta_1}{2}}-e^{x_1\theta_1}\right)\left(e^{x_1\theta_1}-1\right)\alpha_1 \\ & + \Bigg(\left(e^{\frac{L_h\theta_1}{2}}-1\right)\left(e^{\frac{L_h\theta_1}{2}}-e^{x_1\theta_1}\right)\left(e^{x_1\theta_1}-1\right)T_a \\ & + \left(e^{L_h\theta_1}-e^{2x_1\theta_1}\right)T_h + e^{\frac{L_h\theta_1}{2}}\left(e^{2x_1\theta_1}-1\right)T_{s1}\Bigg)\theta_1^2\Bigg) \end{aligned} \tag{3.11}$$

$$\begin{aligned} T_2(x_2) = \frac{e^{-x_2\theta_2}}{\delta_2}\Bigg(& e^{(L_h+x_2)\theta_2}T_a - e^{(L_{nit}+x_2)\theta_2}T_a \\ & + e^{\frac{L_h\theta_2}{2}+L_{nit}\theta_2}(T_a-T_{s1}) + e^{\frac{1}{2}(L_h+4x_2)\theta_2}(T_{s1}-T_a) \\ & + e^{\frac{1}{2}(L_{nit}+4x_2)\theta_2}(T_a-T_{s2}) + e^{L_h\theta_2+\frac{L_{nit}\theta_2}{2}}(T_{s2}-T_a)\Bigg) \end{aligned} \tag{3.12}$$

$$\begin{aligned} T_3(x_3) = \frac{e^{-x_3\theta_3}}{\delta_3}\Bigg(& e^{(L_{mem}+x_3)\theta_3}T_a - e^{(L_{nit}+x_3)\theta_3}T_a \\ & + e^{\frac{(L_{nit}+4x_3)\theta_3}{2}}(T_a-T_{s2}) + e^{L_{mem}\theta_3+\frac{L_{nit}\theta_3}{2}}(T_{s2}-T_a)\Bigg). \end{aligned} \tag{3.13}$$

The value of temperatures at the edges of heater (T_{s1}) and top nitride (T_{s2}) can be found by applying energy balance at the interface. Energy balance equation at the interface of region 1 and 2 can be written as,

$$\frac{dT_1}{dx_1}\Big|_{x_1=\frac{L_h}{2}} + \frac{P}{K_{eff1}A_{c1}} = \frac{K_{eff2}A_{c2}}{K_{eff1}A_{c1}}\frac{dT_2}{dx_2}\Big|_{x_2=\frac{L_h}{2}} \tag{3.14}$$

which after substitution of values will be given as,

$$\frac{1}{\delta_2\theta_1\lambda_1}\Bigg(-\left(e^{\frac{L_h\theta_1}{2}}-1\right)^2\alpha_1\delta_2+\theta_1\Big(\mu_1\Big((T_a-T_{s1})\zeta_2+2\Big(T_{s2}-T_a\Big)\sqrt{\eta_2}\Big)\theta_2\lambda_1+ \\ \delta_2\Bigg(\Bigg(-T_a+2e^{\frac{L_h\theta_1}{2}}(T_a-T_h)+T_{s1}+e^{L_h\theta_1}(-T_a+T_{s1})\Bigg)\theta_1+\mu_2\lambda_1\Big)\Bigg)\Bigg)=0 \tag{3.15}$$

Similarly for region 2 and 3, energy balance equation produce,

$$\frac{2(T_{s1}-T_a)\delta_3\sqrt{\eta_2}\theta_2+(T_a-T_{s2})(\delta_3\zeta_2\theta_2-\mu_3\delta_2\zeta_3\theta_3)}{\delta_2\delta_3}=0 \tag{3.16}$$

Solution of (3.15), (3.16) results in the intermediate temperatures (T_{s1} and T_{s2}) ;

$$T_{s1}=\Bigg(\theta_1\Big(4\mu_1\delta_3\eta_2\theta_2^2\lambda_1+(\delta_3\zeta_2\theta_2-\mu_3\delta_2\zeta_3\theta_3)\Big(-\mu_1\zeta_2\theta_2\lambda_1+\delta_2\theta_1\big(2+\lambda_1\big)\Big)\Big)\Bigg)^{-1} \\ \times\Bigg(-2e^{\frac{L_h\theta_1}{2}}\Bigg(\cosh\Big(\frac{L_h\theta_1}{2}\Big)\delta_2\left(\alpha_1+T_a\theta_1^2\right)-\delta_2\left(\alpha_1+(T_a-T_h)\theta_1^2\right)-\sinh\Big(\frac{L_h\theta_1}{2}\Big)\theta_1 \\ \times\Big(\mu_2\delta_2+\mu_1T_a\zeta_2\theta_2\Big)\Bigg)(\mu_3\delta_2\zeta_3\theta_3-\delta_3\zeta_2\theta_2)+4\mu_1T_a\delta_3\eta_2\theta_1\theta_2^2\lambda_1\Bigg) \tag{3.17}$$

$$T_{s2} = \left(\theta_1\left(4\mu_1\delta_3\eta_2\theta_2^2\lambda_1 - (\mu_3\delta_2\zeta_3\theta_3 - \delta_3\zeta_2\theta_2)\left(\delta_2\theta_1(2+\lambda_1) - \mu_1\zeta_2\theta_2\lambda_1\right)\right)\right)^{-1}$$
$$\times\left(2\left(e^{\frac{L_h\theta_1}{2}} - 1\right)^2\alpha_1\delta_2\delta_3\sqrt{\eta_2}\theta_2 + \theta_1\left(-\mu_1 T_a\delta_3\left(\zeta_2^2 - 4\eta_2\right)\theta_2^2\lambda_1 - \mu_3 T_a\delta_2^2\zeta_3\theta_1\theta_3(2+\lambda_1)\right.\right.$$
$$+\delta_2\theta_2\left(\mu_1\mu_3 T_a\zeta_2\zeta_3\theta_3\lambda_1 - \delta_3\left(2\mu_2\sqrt{\eta_2}\lambda_1 - \theta_1(-4e^{\frac{1}{2}(L_{nit}\theta_2 + L_h(\theta_1+\theta_2))}\right.\right.$$
$$\left.\left.\left.\left.(T_a - T_h) + T_a\zeta_2(2+\lambda_1)\right)\right)\right)\right) \tag{3.18}$$

where

$\theta_1 = \sqrt{\frac{hA_{s1}}{K_{eff1}V_1}}$, $\theta_2 = \sqrt{\frac{hA_{s2}}{K_{eff2}V_2}}$, $\theta_3 = \sqrt{\frac{hA_{s3}}{K_{eff3}V_3}}$

$\delta_2 = e^{L_h\theta_2} - e^{L_{nit}\theta_2}$, $\delta_3 = e^{L_{mem}\theta_3} - e^{L_{nit}\theta_3}$,

$\zeta_2 = e^{L_h\theta_2} + e^{L_{nit}\theta_2}$, $\zeta_3 = e^{L_{mem}\theta_3} + e^{L_{nit}\theta_3}$,

$\eta_2 = \left(e^{(L_h+L_{nit})\theta_2}\right)$, $\lambda_1 = \left(e^{L_h\theta_1} - 1\right)$,

$\mu_1 = \frac{(K_{eff2}A_{c2})}{(K_{eff1}A_{c1})}$, $\mu_2 = \frac{P}{(K_{eff1}A_{c1})}$, $\mu_3 = \frac{(K_{eff3}A_{c3})}{(K_{eff2}A_{c2})}$.

Using the solution of intermediate temperatures, the conduction power loss is calculated as,

$$P_{cond-mem} = 2K_{eff12}(T_{mem} + T_{top} + T_{Pt})(T_h - T_{s1}) + \frac{8K_{eff12}A_{c2}}{(L_{nit} - L_h)}(T_{s1} - T_{s2})$$
$$+ \frac{8K_{eff3}A_{c3}}{(L_{mem} - L_{nit})}(T_{s2} - T_a) \tag{3.19}$$

where K_{eff12} is the effective thermal conductivity of region 1 and 2. K_{eff12} depends on the ratio of heat spreader length to membrane length ratio and is calculated as,

$$K_{eff12} = \frac{K_{Si3N4}T_{nit} + K_{SiO2}T_{oxide} + \xi^2 K_{top}T_{top}}{T_{nit} + T_{oxide} + \xi^2 T_{top}} \tag{3.20}$$

with $\xi = \frac{L_{nit}}{Lmem}$.

The convection power is calculated for the three regions by the following equations,

$$P_{cr1} = \theta_1^{-3}\left(hL_h\left(L_h\alpha_1\theta_1 - 2\left(2\alpha_1 - \left(T_h - 2T_a + T_{s1}\right)\theta_1^2\right)\tanh\left(\frac{L_h\theta_1}{4}\right)\right)\right) \tag{3.21}$$

$$P_{cr2} = \theta_2^{-1}\left(4hL_h\left(2T_a - T_{s1} - T_{s2}\right)\tanh\left(\frac{\left(L_h - L_{nit}\right)\theta_2}{4}\right)\right) \tag{3.22}$$

$$P_{cr3} = \theta_3^{-1}\left(4hL_h\left(T_{s2} - T_a\right)\tanh\left(\frac{\left(L_{mem} - L_{nit}\right)\theta_3}{4}\right)\right) \tag{3.23}$$

The total convection power from whole of the membrane is then sum of the three power computed using (3.21), (3.22), and (3.23) which can be represented as,

$$P_{total-conv} = P_{cr1} + P_{cr2} + P_{cr3} \tag{3.24}$$

With the temperature at the edges evaluated using (3.17) and (3.18), total losses can be calculated using (3.19) and (3.24), the conduction and convection losses in the top nitride and membrane can be calculated using (3.19), (3.21), (3.22) and (3.23). The total power loss is calculated as,

$$P_{total-cc} = P_{cond-mem} + P_{total-conv} \tag{3.25}$$

Case-2: With Conduction and Radiation Losses Present

This case is particularly implies a vacuum condition where the convection losses are not present, for the gas sensing temperatures below 400°C, the radiation term can be approximated as $4\epsilon\sigma A_s T_a^3(T-T_a)$ [125]. With this linearized approximation, the governing equation can be presented as,

$$K_{eff}V\frac{d^2T}{dx^2} + P - 4\epsilon\sigma A_s T_a^3(T-T_a) = 0 \tag{3.26}$$

The energy balance of conduction and radiation per unit volume across the three regions are,

$$\frac{d^2T_1}{dx_1^2} - \frac{4\epsilon\sigma A_{s1}T_a^3(T_1-T_a)}{K_{eff1}V_1} + \alpha_1 = 0 \ (0 \le x_1 \le \frac{L_h}{2}) \tag{3.27}$$

$$\frac{d^2T_2}{dx_2^2} - \frac{4\epsilon\sigma A_{s2}T_a^3(T_2-T_a)}{K_{eff2}V_2} = 0 \ (\frac{L_h}{2} \le x_2 \le \frac{L_{nit}}{2}) \tag{3.28}$$

$$\frac{d^2T_3}{dx_3^2} - \frac{4\epsilon\sigma A_{s3}T_a^3(T_3-T_a)}{K_{eff3}V_3} = 0 \ (\frac{Lnit}{2} \le x_3 \le \frac{L_{mem}}{2}) \tag{3.29}$$

The solution of (3.26) can be found using the similar boundary conditions as used for case-1. The solution is similar to (3.17), (3.18) except the terms θ_1, θ_2, and θ_3 for case-2 are given as,

$$\theta_1 = \sqrt{\frac{4\epsilon\sigma A_{s1}T_a^3}{K_{eff1}V_1}},\ \theta_2 = \sqrt{\frac{4\epsilon\sigma A_{s2}T_a^3}{K_{eff2}V_2}},\ \theta_3 = \sqrt{\frac{4\epsilon\sigma A_{s3}T_a^3}{K_{eff3}V_3}}.$$

The radiation loss can be calculated using (3.26) and can be represented as,

$$P_{rr1} = \theta_1^{-3}\left(4\epsilon L_h \sigma T_a^3((\alpha_1\theta_1 L_h) + (2(\theta_1^2 - 2\alpha_1)(T_{s1} + T_h - 2T_a)))\tanh(\frac{\theta_1 L_h}{4})\right) \tag{3.30}$$

$$P_{rr2} = \theta_2^{-1}\left(16\epsilon\sigma L_h T_a^3(2T_a - T_{s1} - T_{s2})\tanh(\frac{\theta_2(L_h - L_{nit})}{4})\right) \tag{3.31}$$

$$P_{rr3} = \theta_3^{-1}\left(16\epsilon\sigma L_h T_a^3(T_{s2} - T_a)\tanh\left[\frac{\theta_3(L_{mem} - L_{nit})}{4}\right]\right) \tag{3.32}$$

The total radiation losses from whole of the membrane will be the sum of the three computed power and is given as,

$$P_{total-rad} = P_{rr1} + P_{rr2} + P_{rr3} \tag{3.33}$$

The conduction and radiation losses in the top nitride and membrane can be calculated using (3.19), (3.30), (3.31) and (3.32). Where, the edges temperature are evaluated using (3.17) and (3.18) using the θ_1, θ_2, and θ_3 values applicable in this case. Total losses can be calculated as,

$$P_{total-cond-rad} = P_{total-cond} + P_{total-rad} \tag{3.34}$$

Case-3: With Conduction, Convection, and Radiation Present

With all the loss mechanism, the volumetric thermal energy balance differential equation becomes,

$$K_{eff} V \frac{d^2T}{dx^2} + P - A_s(h + 4\epsilon\sigma T_a^3)(T - T_a) = 0 \tag{3.35}$$

Hence, the differential equations for the three regions are written as,

$$\frac{d^2T_1}{dx_1^2} - \theta_1(T_1 - T_a) + \alpha_1 = 0,\ (0 \leq x_1 \leq \frac{L_h}{2}) \tag{3.36}$$

$$\frac{d^2T_2}{dx_2^2} - \theta_2(T_2 - T_a) = 0,\ (\frac{L_h}{2} \leq x_2 \leq \frac{L_{nit}}{2}) \tag{3.37}$$

$$\frac{d^2T_3}{dx_3^2} - \theta_3(T_3 - T_a) = 0,\ (\frac{Lnit}{2} \leq x_3 \leq \frac{L_{mem}}{2}) \tag{3.38}$$

The solution of (3.35) can be obtained by applying the boundary conditions. The solution is similar to (3.17) and (3.18) with,

$$\theta_1 = \sqrt{\frac{A_{s1}(h+4\epsilon\sigma T_a^3)}{K_{eff1}V_1}},\ \theta_2 = \sqrt{\frac{A_{s2}(h+4\epsilon\sigma T_a^3)}{K_{eff2}V_2}},\ \theta_3 = \sqrt{\frac{A_{s3}(h+4\epsilon\sigma T_a^3)}{K_{eff3}V_3}}.$$

Once the temperatures at the edges are evaluated, the total power can be computed in a similar way as in the previous case. In order compute the total losses in the optimized microhotplate, the component of conduction loss to air can be theoretically calculated as [91]

$$P_{air} = 4\pi K_{air} R_h (T_h - T_a) \tag{3.39}$$

where K_{air} is the thermal conductivity of air in $\frac{W}{mK}$, R_h is radius of the heater. The total loss in the membrane can be computed as,

$$P_{total-cond-conv-rad-air} = P_{total-cond} + P_{total-rad} + P_{total-conv} + P_{air}. \tag{3.40}$$

To evaluate the analytical model the microhotplate is designed with meander [26, 49] heater. Fig. 3.12 shows the layout of the meander microheater and square membrane,

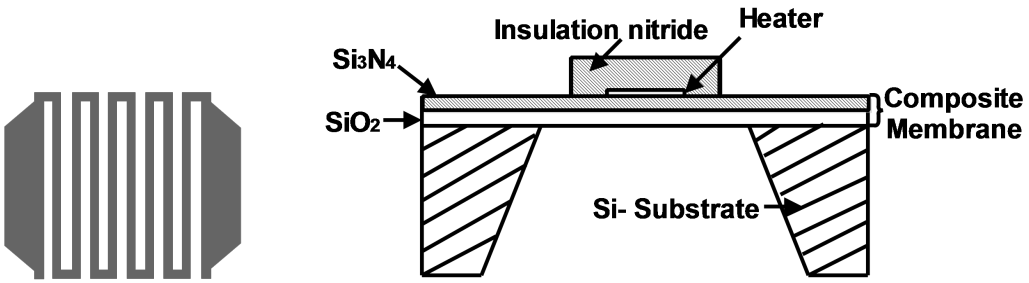

(a) (b)

FIGURE 3.12: (a) Top view of the meander microheater. (b) Cross-sectional view of square membrane (not to scale).

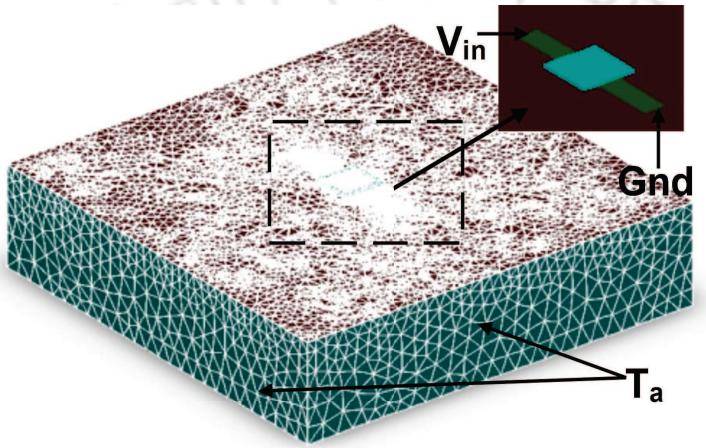

FIGURE 3.13: The meshed image of the microhotplate. Due to the dense meshing, microheater and insulation nitride cannot be seen and therefore they are expanded in the figure. V_{in} is the applied potential, Gnd is the electrical zero potential and sides of the dies are at ambient temperature, T_a .

used for this investigation. The minimum lithographic dimension used for the microheater is 5 μm and the corresponding heater resistance is 182 Ω. To insulate the heater from the gas sensing layer, a silicon nitride layer is deposited over the patterned microheater. The thickness and lateral dimension of silicon nitride is varied from 0.3 μm$-$8 μm and from 120 μm$-$250 μm respectively. For meshing, a 50 μm element mesh size is used for the substrate. Membrane layers are meshed with 30 μm element size. For the microheater, 5 μm mesh element is utilized and the resulting number of volume elements are 1,23,375. The meshed image of the generated microhotplate along with the voltage load and boundary conditions is shown in Fig. 3.13.

3.4.2 Comparison of Theoretical and Simulation Results

A convection coefficient value of 20W/m^{2}K and an emissivity value of 0.7 [6] is used for both simulation and analytical calculations. MHR is defined as the ratio of membrane side length to heater side length. With a membrane side length of 517 μm and a heater side length of 100 μm, the MHR value is 5.17. For a given die size, membrane thickness and material, this MHR value has resulted in minimum thermal losses to the substrate. Subsequently, top nitride thickness is optimized for attaining a temperature uniformity of 0.22K/μm, a value which is comparable to reported literature [15]. The heater edges temperature, T_{s1} can also be written as, $T_{s1} = T_h - (\text{Uniformity} * L_h/2)$, where T_h is the desired operating temperature. Insulation nitride thickness is the only unknown, which can be evaluated from (3.17). The required nitride thickness, for a temperature uniformity of 0.22K/μm at 694K, is 8.29 μm. In order to verify the performance parameters, the structure is analyzed using FEM simulation, which includes the second order effects. Finally, with the optimum thickness of the nitride layer, effect of its coverage area on power and temperature uniformity is studied and the results are compared with analytical model.

Effect of Heat Spreader Thickness on Temperature Uniformity

For gas sensing applications, the specific operating temperature depends on the metal oxide, type of gas and its concentration. The typical values of temperature is found in 523K-773K range and a temperature of 694 K is targeted in this work. For a fair comparison, the heat spreader area of 120 μm $\times$ 120 μm and the targeted temperature of 694 K are kept constant. The FEM simulation results of temperature uniformity as a function of heat distributor thickness is plotted in Fig. 3.14. There is a large improvement in the temperature uniformity as the thickness is increased, but it starts to saturate beyond a nitride layer thickness of 5 μm. A 8 μm thick insulation layer is a wise choice as there is an improvement of 89% in the temperature uniformity compared to membrane with no insulation nitride. The reason for the increase in temperature uniformity in the active region with thickness is because of the selective increase in thermal conductivity of region 1 and 2. Whereas, the thermal conductivity of the region

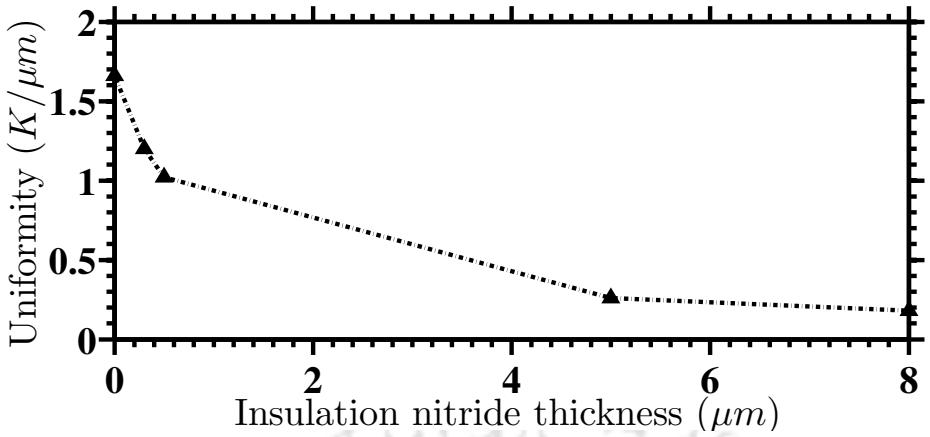

FIGURE 3.14: Thermal uniformity as a function of nitride thickness

3 will remain the same for a fixed nitride length. As a result, the temperature difference between center and heater edge is made lower.

Effect of Heat Spreader Length on Power and Temperature Uniformity

The analytical model is compared with the FEM simulation results. Simulations are carried out with convective and radiative boundary conditions applied to the whole membrane and to the top nitride. The values of the intermediate temperatures (T_{s1} and T_{s2}) are obtained from (3.17) and (3.18). The analytical and simulation results of case-1, case-2 and case-3 are shown in Fig. 3.15, Fig. 3.16 and Fig. 3.17 respectively. All the results are in close agreement with the analytical model. The model resulted in a maximum error of 4.29%, among the three cases, which occurs in case-2, for a heat spreader length of 250 μm. For the hand-held battery operated devices, desirable operating voltage ranges from 1 V – 2 V [126]. Therefore, for an applied voltage of 2 V and the top nitride thickness of 8 μm, Fig. 3.18 shows the comparison of analytical and simulation results of the temperature profile over the half length of the membrane. It is known that the temperature non-uniformity in the active area increases as the operating temperature increases. For the same constant applied voltage, the highest operating temperature achieved is with 120 μm $\times$ 120 μm insulation nitride area and the obtained temperature uniformity is 0.18 K/μm. In other words, the optimized insulation

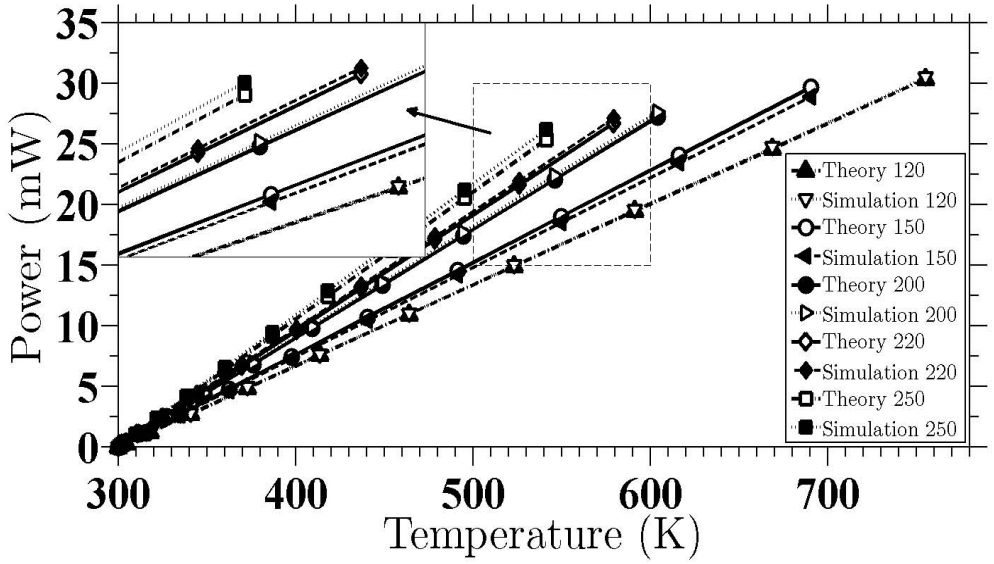

FIGURE 3.15: Comparison of analytical modeling with simulation results for conduction convection case (case-1)

nitride area, apart from saving in power and improvement of temperature uniformity, will also helps in achieving high operating temperature at a constant applied voltage. The maximum deviation between analytical and simulation results occurs outside the top nitride area for 120 μm $\times$ 120 μm area, at around 120 μm distance as shown in Fig. 3.18. The deviation can be attributed to the heat sink effect of the contact electrodes. Interestingly, the heat sink effect of contact electrodes is minimized as the top nitride area increases. The above mentioned errors in the model can be reduced by considering the whole membrane area instead of strips and also by taking into consideration the effect due to the perturbation caused by the contact pads. The contribution of convection and radiation losses to the total power at this convection coefficient and temperature are negligible.

Since the intermediate temperatures are now known, the power losses in the top insulation nitride layer can be calculated. The power loss in the top nitride due to conduction losses, for various length has been shown in Fig. 3.19 for an applied voltage of 2 V and 8 μm top nitride thickness. As the heat spreader length is increased, the conduction loss in the region 2 increases. This is one of causes for the increase in thermal losses and reduction in the maximum achievable operating temperature.

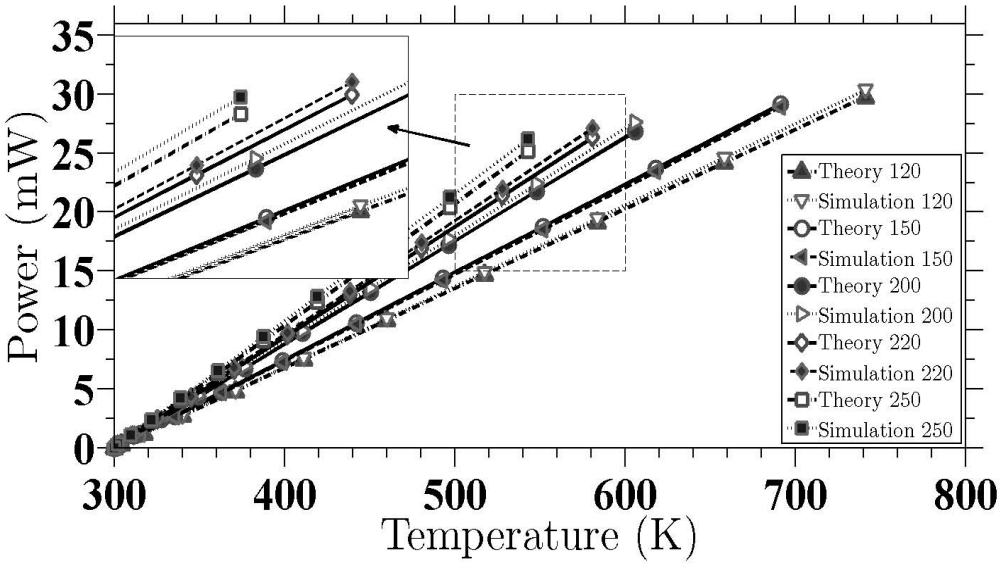

FIGURE 3.16: Comparison of analytical modeling with simulation results for conduction radiation case (case-2)

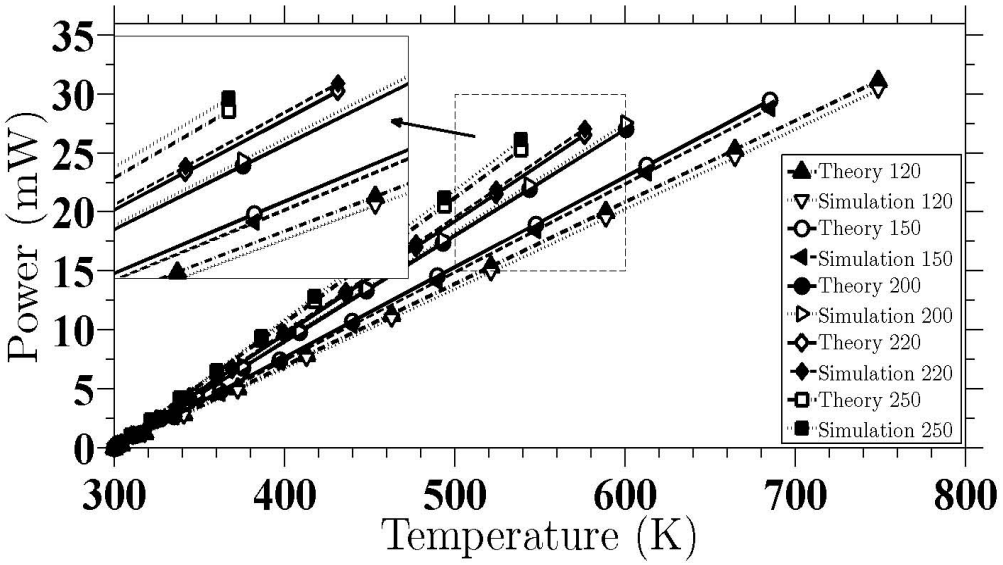

FIGURE 3.17: Comparison of analytical and simulation results with conduction convection and radiation loss (case-3)

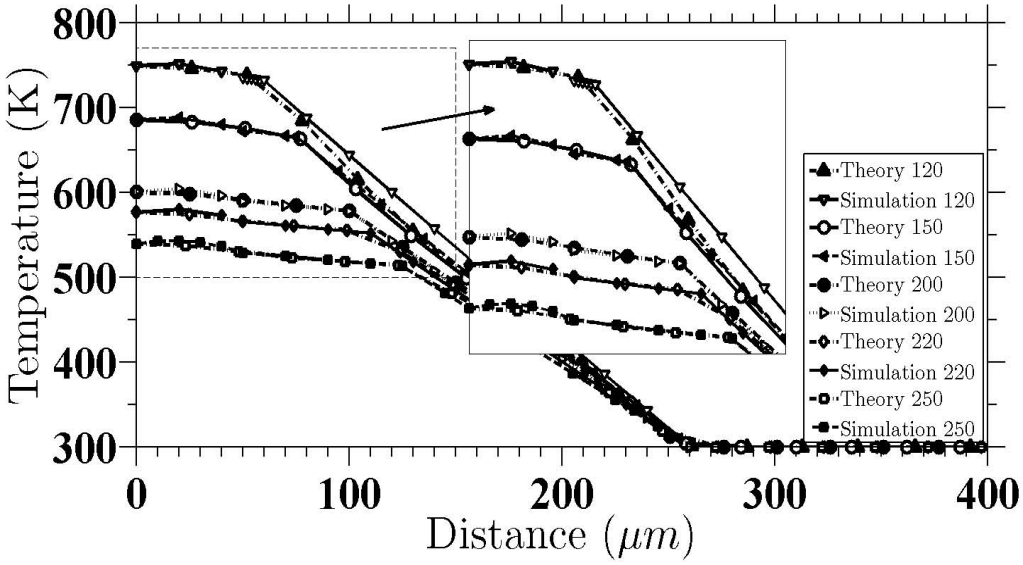

FIGURE 3.18: Comparison of simulation and analytical model temperature profile across the half length of membrane for case-3, with 2 V and 8 μm insulation nitride thickness.

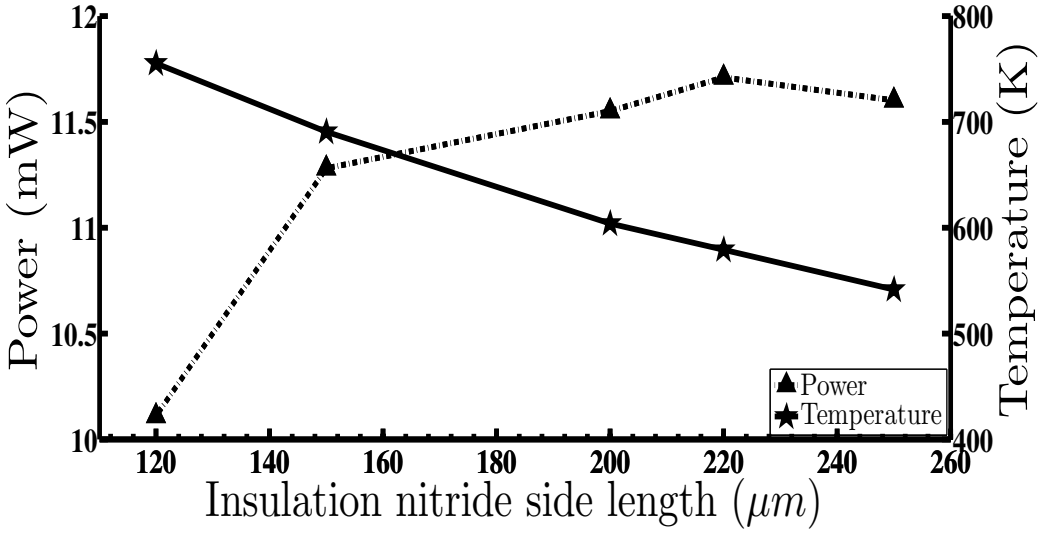

FIGURE 3.19: Conduction loss in insulation nitride and highest achievable temperature with 2 V and 8 μm insulation nitride thickness.

Reducing the insulation layer thickness

Though with a 8μm thick silicon nitride layer, a thermal uniformity of $0.18\frac{\text{K}}{\mu\text{m}}$ is obtained, deposition time for this thick silicon nitride can be large. The deposition time can be reduced by decreasing the insulation layer thickness. We have investigated two methods for reducing the insulation layer thickness and hence, the deposition time. In method one, the thickness can be reduced while retaining all the advantages, is by employing a material with higher thermal conductivity than silicon nitride. Separate simulation studies are carried out where silicon carbide was employed as insulation layer material. The study reveals that with an 1.5μm thick silicon carbide layer the targeted thermal uniformity of $0.18\frac{\text{K}}{\mu\text{m}}$ can be achieved. Therefore, the deposition time in the whole process will significantly reduce by employing silicon carbide layer while retaining similar uniformity.

Second method use the combination of two methods i.e, the choice of suitable heater geometry plus optimization of insulation layer dimensions. Simulation studies were carried out to find the optimum dimension of insulation layer, required for a targeted uniformity of $0.22\frac{\text{K}}{\mu\text{m}}$, a value comparable to the reported literature. This method has reduced the silicon nitride thickness requirement to 50%, i.e., a 4 μm nitride layer will be required to achieve the targeted uniformity. Whereas, for SiC as insulation layer, the thickness requirement has reduced from 1.5μm to 0.8 μm, and resulted in even better thermal uniformity than targeted.

3.5 Transient Analysis of Bridge Microhotplate

A thick insulation layer alters the thermal resistance of membrane which affects the thermal response time of microhotplate. In this study, a lumped element model is developed by including the effective area of the microhotplate. This allows an accurate estimations of thermal capacitance and resistance. These values are used for the steady state power

calculations. Theoretical calculated power allows to initiate the model without the constrain of iterative calculations or prior knowledge of experiment results. The model is employed to analyze the effect thermal mass on transient response of microhotplate. For evaluation of developed model, FEM simulations are carried out.

3.5.1 Transient Modeling of Bridge Membrane

In this section, we target to develop a lumped element model for analyzing the effect of thick insulation layer on the transient response of a bridge membrane. Fig. 3.20a shows the top view of the bridge membrane modeled in this work. Due to the larger thermal capacity of the silicon substrate the edges of the supporting arms can be considered to be at room temperature. Therefore, only the bridge needs to be considered in the modeling approach. The bridge is divided into supporting arms and central platform. The central platform supports the meander microheater, and arms supports the electrical connection (or tracks). The presence of insulation nitride layer in the central platform area alter its thermal conductivity. Therefore, thermal resistances of the two arms and the central platform are calculated separately. Fig. 3.20b shows the lumped element model of the membrane. With this, the heat conduction equation can be written as [85],

$$C_{tot}\frac{dT}{dt} = P_{app} - \frac{\Delta T}{R_{tot}}, \tag{3.41}$$

where, C_{tot}, R_{tot} are the total thermal capacitance and resistance of the bridge membrane. P_{app} is the power applied to the microheater and ΔT is the temperature difference between heater temperature at center (T) and ambient temperature (T_a). Solution to the differential equation 3.41 is given as,

$$T(t) = T_a + P_{app}R_{tot}\left(1 - e^{\frac{-t}{R_{tot}C_{tot}}}\right). \tag{3.42}$$

Equation (3.42) will produce the time dependent thermal response, once the total thermal resistance and capacitance are known. The main contribution of thermal resistance

is from the nitride covered area and the arms. Whereas, the main contribution of capacitance term arises from the active area only. The thermal resistance and capacitance distribution is represented by lumped elements as shown in Fig.3.20.

$$R_{tot} = 8R_{Cen} + 2R_{Arm}, \tag{3.43}$$

where R_{Cen} is thermal resistance of the top nitride area, R_{Arm} is the thermal resistance of the supporting arm. Thermal resistance of the supporting arm can be written as,

$$R_{Arm} = \frac{L_{Arm}}{K_{Arm}A_{Arm}} = \frac{L_{Arm}}{K_{Arm}T_{mem}W_{Arm}}, \tag{3.44}$$

where, L_{Arm}, K_{Arm}, and A_{Arm} are length of the arm, in-plane thermal conductivity and the cross-sectional area of the arm respectively. T_{mem} is the thickness of the membrane. The effective width of the arm depends on the thickness of the top nitride layer. This is because of increased thermal capacity in the active area which affects the isotherm in insulation nitride covered area. The effective width of the strip can then be written as, $W_{Arm} = L_h + \left(\frac{L_{Nit}-L_h}{L_{mem}+L_{Nit}}\right)L_{Nit}$.

$$R_{Cen} = \frac{L_{Nit}}{2K_{Cen}A_{Cen}} = \frac{L_{Nit}}{2K_{Cen}(T_{mem} + T_{top})L_h}, \tag{3.45}$$

where, L_{Nit}, K_{Cen}, A_{Cen} and T_{top} are the side length of the top insulation nitride, cross planes thermal conductivity, the cross-sectional area of center and thickness of top nitride respectively. The total thermal capacitance of the bridge membrane is given as,

$$C_{tot} = 4 \times C_{Cen} = 4L_{nit}(T_{mem} + T_{top})L_h((\rho c_p)_{Cen}) \tag{3.46}$$

with the resultant volumetric heat capacity $((\rho c_p)_{Cen})$ written as,

$(\rho c_p)_{Cen} = \frac{(\rho c_{p_{mem}} \times \rho c_{p_{top}})(T_{mem}+T_{top})}{\rho c_{p_{top}} T_{mem}+\rho c_{p_{mem}} T_{top}}$

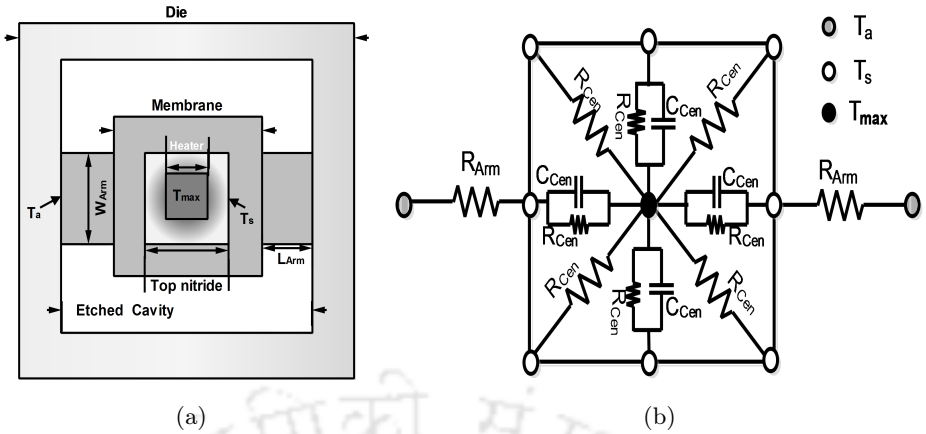

FIGURE 3.20: (a) Top view of a die consisting of bridge membrane (gray), active area (dark gray square at the center), etched cavity (white) and insulation nitride (gradient white), (b) Lumped element model of the bridge membrane, T_{max} is the temperature at the center of membrane, T_s and T_a are the temperatures at the edges of top nitride and ambient temperature respectively.

Equation (3.42) can be utilized now, with the calculations of the thermal resistances using (3.43) and capacitance using Eq. (3.46).

The bridge membrane of present work has two supporting arms of length (L_{Arm}) and width (W_{Arm}) of 120 μm and 100 μm respectively. The meander [30] microheater is patterned onto the central membrane which is 140 μm $\times$ 140 μm in dimensions. Heater area is 100 μm $\times$ 100 μm, over which an insulation layer area of 120 μm $\times$ 120 μm is deposited [109]. Thermal mass is increased by varying the nitride thickness from 0.3 μm - 8 μm.

3.5.2 Results and Discussion

For all simulations the die size, maximum operating temperature (694K), membrane thickness and composition are kept constant. Die edges are assumed to be at room temperature [112] and in this temperature range, the radiation losses can be safely ignored [8]. Time constant (TC_{90}) is calculated as the time required for the temperature to reach the 90% of the maximum heater temperature (T_{90}) [9]. For the calculation of theoretical time constant, Eq. (3.42) is solved iteratively. Steady state theoretical power is also calculated by equating the LHS of Eq. (3.41) to zero, which resulted in $P_{app} = \frac{\Delta T}{R_{tot}}$. The results from this and iteratively calculated power are in close agreement. Hence,

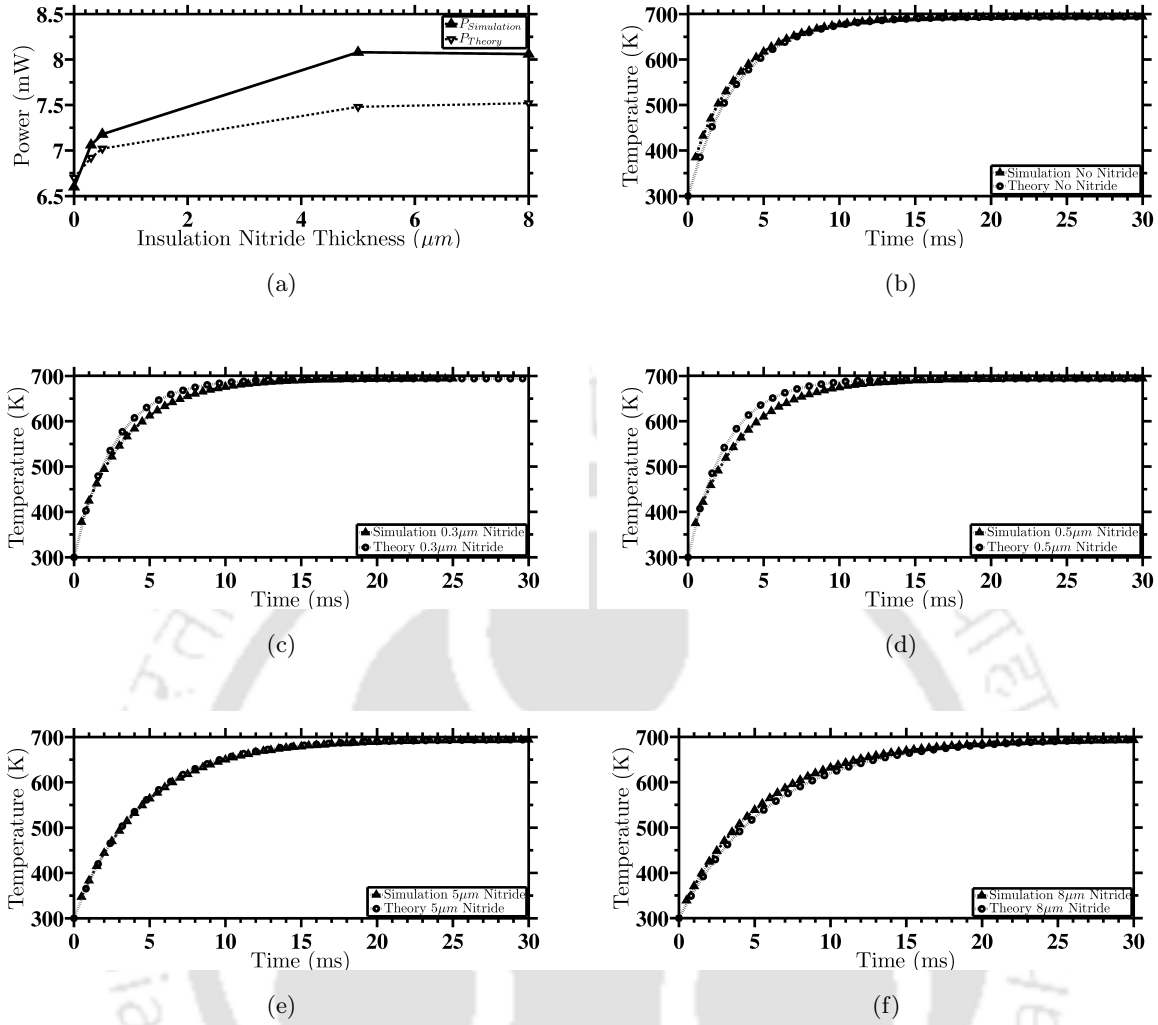

FIGURE 3.21: Comparison of FEM and theoretical (a) steady state power consumption, (b-f) transient response of bridge membrane with insulation nitride thickness of (b) no nitride, (c) 0.3 μm, (d) 0.5 μm, (e) 5 μm, and (f) 8 μm

instead of iteratively calculating power, the model can be initiated by using the theoretically calculated P_{app} values. Fig. 3.21(a) shows the comparison of power calculated from lumped model and simulation. The maximum error observed across different nitride thickness is less than 8%.

The resulting transient plots for different nitride thickness are shown in Fig. 3.21(b-f) . As the top nitride thickness increases, the thermal resistance in the center of the membrane decreases. Therefore, the overall thermal resistance also decreases. The theoretical model predicts the T_{90} temperature close to the simulation results. Error in the model (Fig. 3.22) are within 3.2%. In comparison to bridge membrane with no nitride layer, the time constant has increased by 72.95% with 8 μm thick nitride layer.

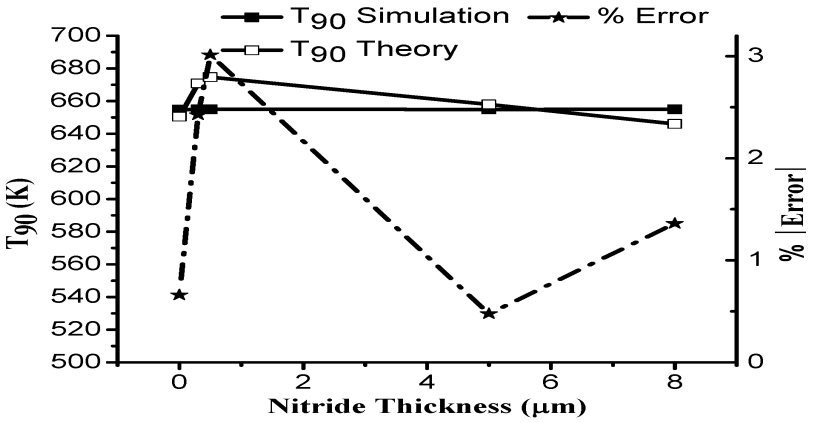

FIGURE 3.22: Simulation and theoretical temperature evaluated at TC_{90}

3.6 Membrane Area Error Reduction - Triangular Approximation Based Model

In modeling, it is a common practice to make assumptions regarding the area of membrane. In [85], Pike et al. approximated the membrane into rectangular strips. Whereas, Li et al. approximated the square geometry as a circular shape [125]. These approximations does not takes into account a large portion of the membrane which directly affects the accuracy of modeling results. The modeling accuracy can be improved by, taking most of the membrane area into consideration. In-order to minimize the area errors, the membrane is divided into 8 symmetrical triangles as shown in figure 3.23. Each triangle has a base width of $\frac{L_{mem}}{2}$ and a height of $\frac{L_{mem}}{2}$ and it is further divided into small rectangular strips of width dx and length L_n. The number of strips in each triangle will be $\frac{L_{mem}}{2dx}$. A small error length (dl), relates the base length (b) with the length of each strip such that $dl = b - L_n$. Iteratively, one can find an optimum value of dl such that the error between the approximated triangle and actual triangle area is minimum. The length of each n strip is related to dl as,

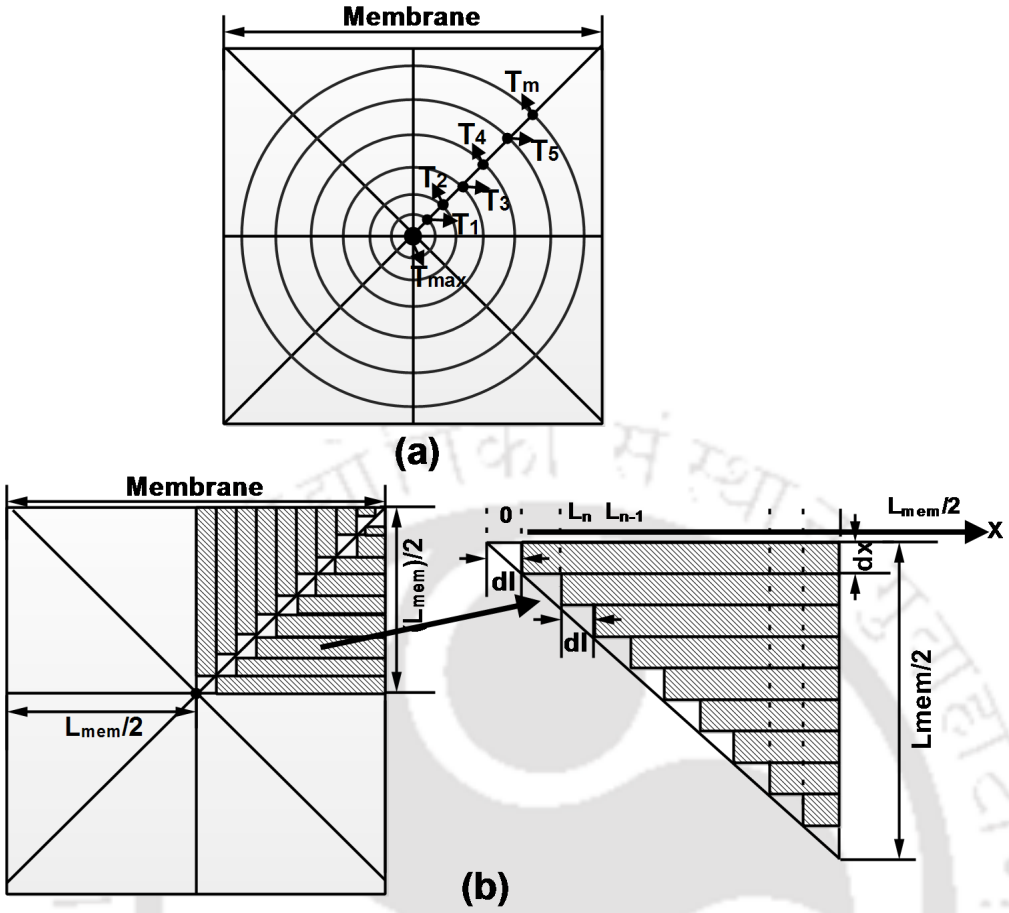

FIGURE 3.23: Membrane is partitioned into 8 similar triangles. (a) Assumed circular symmetry of contour in membrane (b) One such triangle is expanded and hatched part shows the individual strips of width dx.

$$\begin{aligned} L_n &= b - dl \\ L_{n-1} &= b - 2dl \\ L_{n-2} &= b - 3dl \\ &\vdots \\ L_2 &= b - (n-1)dl \\ L_1 &= b - ndl \end{aligned} \tag{3.47}$$

$$\text{and } dl > 0,\ dx > 0 \text{ and } 0 < \frac{dl}{dx} < 1.$$

where b is the base length of triangle which is equal to half membrane length ($\frac{L_{mem}}{2}$).

By assigning a small fixed value for dx, the dl is varied and the condition for the end of iterations is that no strip length should be zero or negative, and this defines the minimum dl value. Therefore, a minimum value of dl will impose a limitation on the maximum accuracy of discretization. By applying this method, the obtained area error is within 0.8%. Another possible approach to the problem is by decreasing the strip width (dx), with a fixed dl value; however, this will increases the number of strips, and it will take unnecessary longer time to converge. Therefore, a fixed value of dx which results in short iterations time and area errors within 1% is initially chosen. After the discretization of the triangle, the power loss in each strip is calculated with the corresponding temperature at strips edge. Figure 3.24 shows the approximated and actual temperature profile assuming a high temperature uniformity in active area. The approximated profile is constructed by assuming a constant temperature in the heater area which is equals to the desired heater temperature (T_{max}), a linear reduction outside the heater area, and constant temperature (T_m) near the membrane edge. The membrane edge temperature (T_m) can be estimated from the conduction heat loss equation [112];

$$T_m = \left(\psi\left(\frac{L_{mem}}{2dx}+\frac{b}{dl}-\frac{b}{dx}\right)-\psi\left(\frac{b}{dl}-\frac{b}{dx}\right)\right)^{-1}\left(dl(\sum_{n=1}^{\frac{b}{dx}}\frac{T(L_n)}{L_n}-\frac{P_{lumped}}{8Kdxt_{mem}})\right) \quad (3.48)$$

where $\psi(x)$ is the polygamma function and P_{lumped} is the power required to attain a desired temperature (T_{max}). P_{lumped} can be calculated from the lumped model [85]. Once the temperatures profile is known, the power consumption can be calculated more accurately by taking the summation of power in each strip;

$$P_{Total} = 8 \times K \times dx \times t_{mem} \sum_{n=1}^{\frac{b}{dx}} \frac{(T(L_n) - T(L_m))}{L_n} \quad (3.49)$$

where K is the in-plane thermal conductivity of the composite membrane and is calculated as

$K = \frac{K_{SiO2}T_{SiO2}+K_{Si_3N_4}T_{Si_3N_4}+K_{Si}T_{Si}}{T_{mem}}$ and T_{mem} is the composite membrane thickness

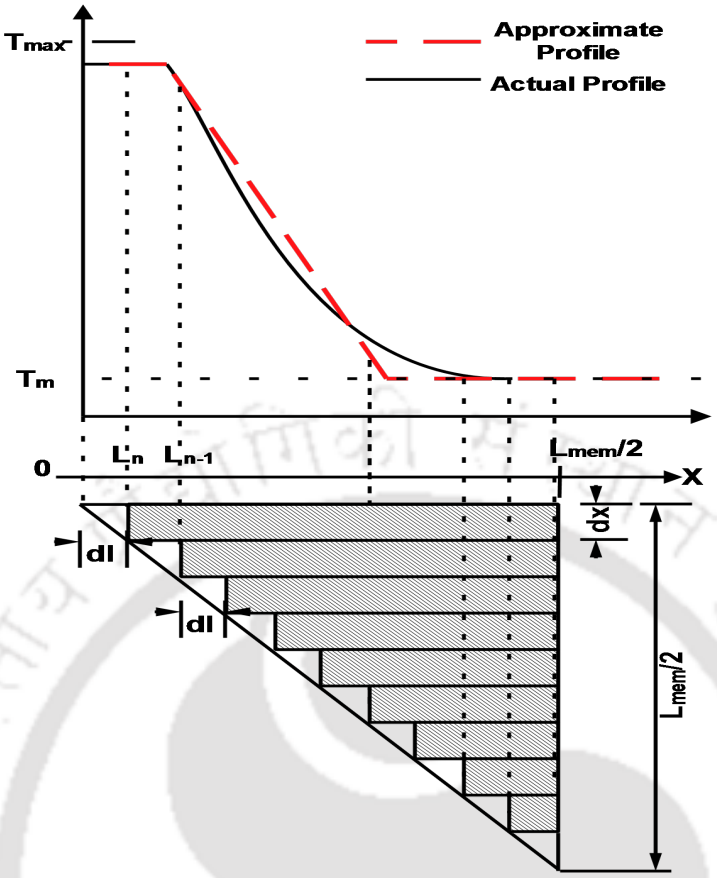

FIGURE 3.24: Approximated temperature profile in the membrane and the approximated triangle for the calculation of power consumption

and can be expressed as $T_{mem} = T_{Si_3N_4} + T_{Si} + T_{SiO2}$.

Figure 3.25 compares the simulated and approximated thermal profile. The approximate profile may help in making a quick estimation of power consumption and the approximated profile shown in Fig. 3.24, assumes a constant temperature both in active area and near the membrane edges. The slope of the transition region can be estimated by;

$$\text{slope} = \frac{(T_{max} - T_m)}{n \times \left(\frac{L_{mem}}{\sqrt{2}} - \frac{L_h}{2} \right)} \tag{3.50}$$

However, the temperature profile can be accurately predicted by employing an analytical expression as obtained in [109]. Nevertheless, the approximated profile is good enough for quickly estimating the power consumption.

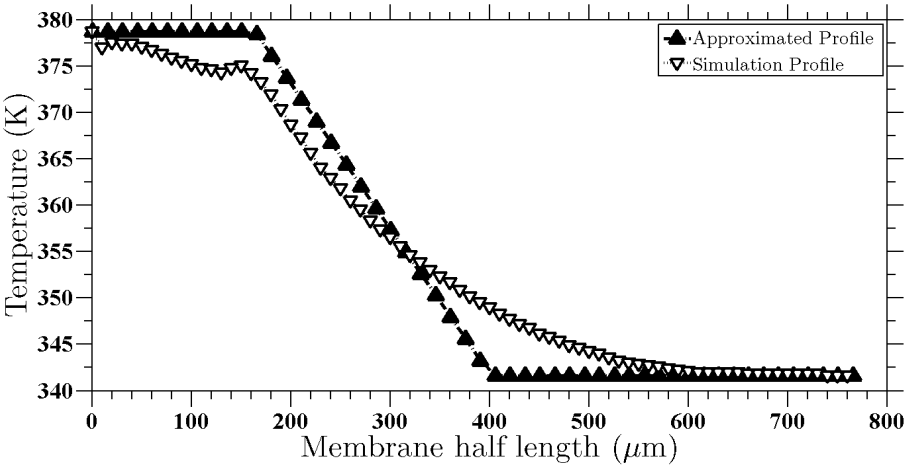

FIGURE 3.25: Simulated and approximated temperature profile for an applied voltage of 9 Volts. The temperature non-uniformity in active can be noted.

3.7 Summary

While constructing a simulation study or developing an analytical model, often reduced parameters and proper assumptions will lead to fast design cycle. In this thesis, the prime performance parameters and assumptions are targeted for a gas sensing application. Thereafter, a systematic and detailed analysis was carried out for the determination of individual power loss components in microhotplate over a wide temperature range. The Callendar – van Dusen equation was employed to accurately predict the resistance values across a temperature range of 300 – 1200K. The most significant losses are due to conduction in both structures i.e with and without insulation nitride layer. Convection losses has as much as 30% contribution to total heat loss mechanism at temperatures greater than 500K. The conduction losses in the insulation nitride layer depends on the thickness of the layer. For a nitride insulation of 0.4μm thick, one has to input 5.42mW more power in order to achieve a particular temperature of 620K. This results in 56.6% higher power compared to a structure without insulation nitride layer. This will be a significant amount of power overhead for a battery operated hand held device. Hence, there exist a tradeoff between good electrical insulation and input power requirements. Even though the emissivity was chosen to be the worst case value, the radiation losses

were not significant and can be safely ignored. For a majority of applications, it is rather important that the heat generated by the microheater is transferred completely to the application domain. The gas sensing is an example where it is desired that the generated heat has to be transferred via conduction in vertical direction.

With a goal of improving the performance of microhotplate, the MHR dependency on the key performance parameters was systematically analyzed. All the four performance parameters namely, power, temperature uniformity, mechanical displacement and time response are affected by the MHR. Whenever a lower power consumption and a higher temperature uniformity is needed a high MHR (MHR=7) can be chosen. However, the mechanical deflection and time response deteriorated with a high MHR value. All these parameters are crucial for the performance of microhotplate and a tradeoff exists among them. The tradeoff required in terms of power, temperature uniformity and time response can be decided by the prime requirement of the application domain. For example, for a gas sensing application, temperature uniformity and time response are key performance parameters. By selecting MHR=4, time response can be improved. With the improved time response, pulse mode operation of the microheater will allow further power saving. During the MHR study, due to the inherit hotspot formation of the meander heater, the values of temperature uniformity obtained are not satisfactory. However, we found that by depositing an optimized insulation layer over heater, the temperature uniformity can be improved. Therefore, in order to optimize the dimensions of the top insulation layer, an analytical model was developed. The model also helps in determining the temperature profile and power consumption of the microhotplate. The model was tested on a square membrane with meander heater. The improvement obtained in the temperature uniformity with 8 μm nitride compared to no-nitride was 89%, however, at the cost of increased power consumption of 28.6%. Finally, from this study it can be concluded that the use of an optimum dimension nitride heat distributor is an effective method for achieving triple advantages, which are electrical insulation, better temperature uniformity and minimized power overhead. The accuracy of the model can be increased by considering the whole membrane area instead of four strips into consideration. This is because strip approximation does not takes into account of a large portion of membrane area. A different method is suggested where in order

to estimate the area of the membrane a triangular approach was employed, and the membrane area error was within 0.8% which was better compared to strip or circular approaches. For predicting the effect of insulation layer thickness on the power and time response, a lumped element model is developed. The thermal resistance and capacitance values used in transient model were also employed for the calculation of steady state power. The model is verified with the FEM simulations and is in close agreement, with a maximum error of 3.2% and 8% in transient response and power calculations respectively.

4

Fabrication and Characterization of Microhotplate

A square microhotplate is fabricated and its detailed process steps are presented in this chapter. The fabrication was carried out through the Indian Nano User Program (INUP) at Center of Excellence in Nanoelectronics (CEN) at Indian Institute of Technology Bombay (IIT-Bombay). Among the three types of membrane, we have utilized square shape membrane because of its ease of fabrication and high yield compared to bridge or spider membrane. The fabricated microhotplate utilizes an S-shape heater [6] with an active area of 500 μm $\times$ 330 μm. The active area dimensions are bounded by the minimum lithographic dimension and in order to minimize the fabrication cost, plastic photomasks are employed for pattern transfer using lithography. Hence, the minimum lithographic dimension used in the microheater design is 50 μm.

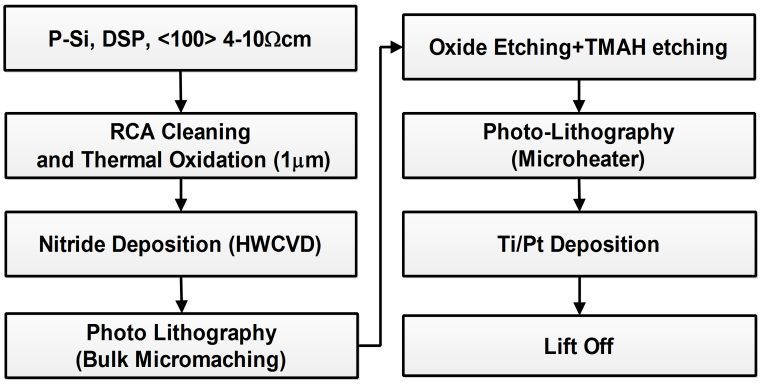

FIGURE 4.1: Process flow of microhotplate

The microheater is patterned over a composite membrane consisting of $Si/SiO_2/Si_3N_4$ layers. The thickness of individual layers in a composite membrane are determined according to the composite stress value and for a stable membrane, the composite stress value should be within ± 0.1 GPa [82]. The composite stress of SiO_2/Si_3N_4 membrane alone is within ± 0.1 GPa limit. Silicon has a compressive residual stress of 6.9 MPa [127]. Combining these two values, the overall stress of $Si/SiO_2/Si_3N_4$ membrane is estimated to be 0.057 GPa-0.0173 GPa. The membrane is compressive in nature for a silicon layer thickness of range 1-10μm. The stress is evaluated for a range of silicon thickness in order to address the fragility issues of the membrane. The fragility can be minimized by either increasing the membrane thickness or by reducing the membrane length. Since the membrane length is bounded by the MHR value, the membrane thickness will be a feasible solution. The membrane dimensions depends on the dimension of the bulk micromachining window. With the opening window of 1500×1500 μm^2, anisotropic etching will result in a membrane side length of 1084 μm. The time of bulk micromachining will define the thickness of the remaining silicon layer in the composite membrane.

4.1 Process Steps

Figure 4.1 summarize the process flow employed for the realization of the designed microhotplate. Figure 4.2 provides the cross-sectional view to visually aid the understanding of the evolution of microhotplate after each process steps.

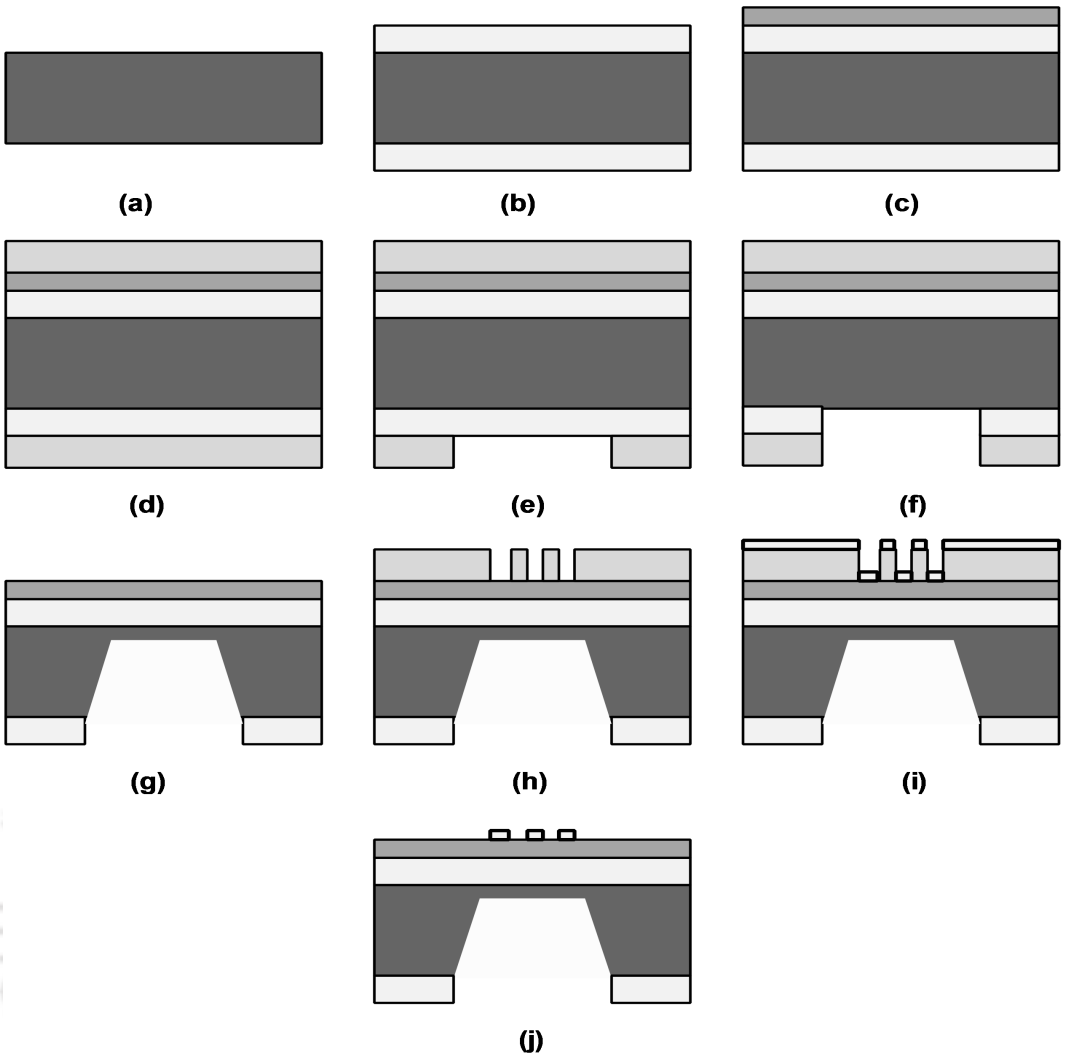

FIGURE 4.2: Visualization of process flow (a) Starting Si- Substrate, (b) Thermally grown oxide, (c) Nitride deposition on one side, (d) PR coating on both sides, (e) Patterning of PR using Mask 1, (f) SiO_2 etching, (g) Bulk micromachining using TMAH and PR removal, (h) PR coating and patterning with Mask 2, (i) Heater material deposition, (j) Patterned heater after Lift-off .

A 2 inch p-type Silicon (100), double side polished (DSP) wafer with resistivity of 4 – 10 Ωcm is chosen as the substrate. After the standard RCA cleaning and drying of silicon wafer (Fig. 4.2), SiO_2 is grown by wet oxidation (Fig. 4.2) at 1100°C for 3 hour. The measured oxide thickness by Ellipsometer is 980 nm which is close to the targeted thickness of 1 μm. In the subsequent process, on one side of the wafer, a thin layer of Si_3N_4 is deposited using Hot Wire Chemical Vapor Deposition (HWCVD) method; for this deposition, the filament temperature of HWCVD is maintained at 1900°C and the substrate temperature is kept at 250°C. A mixture of silane and ammonia ($SiH_4 : NH_3$) in the ratio of 1:20 is passed to the chamber for 25 minutes. The thickness of deposited

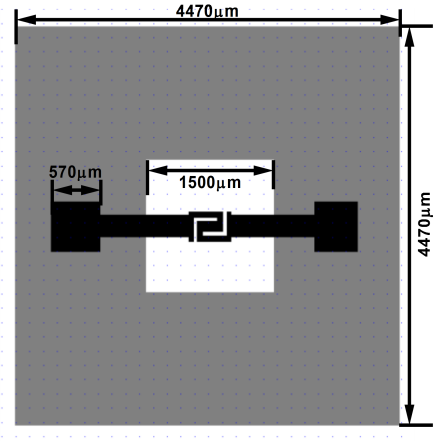

FIGURE 4.3: Photomask of a single die. Gray region is the Mask-1 used for TMAH etching and black layer is for microheater pattering (Mask-2)

film is measured using ellipsometer and results confirmed the deposition of 393 nm nitride layer with this recipe (Fig. 4.2).

The wafer is subjected to the first lithography step, for the subsequent bulk micromachining of silicon wafer. The photomask of single device is shown in Fig. 4.3. However, it may be noted that the photomask is designed for a complete 2 inch wafer and consists of 44 individual microhotplates. A 30 μm wide dicing lines are also provided in the Mask-1 layer in order to ease the separation of individual microhotplates. As can be seen from the figure, the size of the square opening is of 1500 $\times$ 1500 μm^2. Before lithography process, the wafer is dehydrated at 110°C on a hotplate for 15-20 minutes, followed by a coating of PPR (S1813) at 3000 rpm for 30 seconds on the oxide side. As a precaution, the PPR is also coated over nitride deposited side of the wafer (Fig. 4.2). The PPR coated wafers are baked at a temperature of 70°C and for 15 minutes Using Double Side Aligner (DSA) EVG620 and Mask-1, the wafers are exposed with a constant UV dose of 75 mJ/cm^2. The exposed wafer is developed in MF319 solution for 30 second. followed by rinsing in DI water and hardbake for 5 minutes at 90°C. This results in a cross-section as shown in Fig. 4.2. For opening the oxide window and for selectively exposing silicon for TMAH (Tetra Methyl Ammonium Hydroxide) etching, the developed wafer is wet etched with buffered hydrofluoric acid (BHF, etch rate of 82 nm/min) for 12 minutes (Fig. 4.2). TMAH (25% V/V) was used for silicon bulk micromachining. Additionally, 2 ml of IPA is added to 25 ml of TMAH for obtaining smooth etched edges. The etching is carried out for 8 hours and the etch rate with this recipe

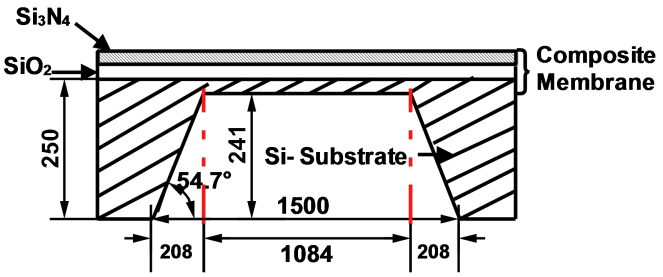

FIGURE 4.4: Cross-sectional diagram of the microhotplate after bulk micromachining (all dimensions are in μm)

at 91°C is found to be 30 μm/hour. The cross-sectional view after the TMAH etching process is shown in Fig. 4.2. The depth of etching is evaluated experimentally using XP2 stylus-based surface profilometer and the result of measurement are summarized in Fig. 4.4. After the bulk micromachining step, the mechanical strength of the wafer is reduced significantly. Therefore, before further processing, a dummy wafer is glued to the micromachined side to avoid wafer or membrane breakage.

After gluing dummy wafer, the microheater is patterned using the second lithography mask. Since this is a lift-off assisted patterning process, the lithography recipe is different from the previous process. For lift-off assisted patterning, the thickness of PPR should be large and therefore, the wafer is coated with PPR at a lower spin rate. The PPR (S1813) is coated at 1500 rpm for 30 seconds followed by 15 minutes prebake at 70°C. Using double side alignment technique, mask-2 is aligned to the back bulk micromachined side and the wafer is exposed to UV at a constant dose of 75 mJ/cm^2. Unlike first lithography step, the postbaking step is not used here since it will harden the PPR and may adversely affect the lift-off. After the development and blow-drying the wafer with nitrogen gun, a cross-sectional of view as shown in Fig. 4.2 is obtained. The platinum heater material is deposited over the patterned wafer using sputtering process. With a deposition rate of 39 nm/min for platinum, 3 minutes sputtering is carried out to achieve the desired heater thickness of 120 nm. Prior to platinum deposition, a 10 nm thick titanium film is deposited to address the adhesion problem of platinum (Fig. 4.2). The lift-off of platinum is carried out at room temperature using a short duration ultra sonication in acetone (Fig. 4.2). The optical images of the single die after these processes are shown in Fig. 4.5, where Fig. 4.5a shows the optical image of backside etched wafer and Fig. 4.5b shows the top view of patterned microheater.

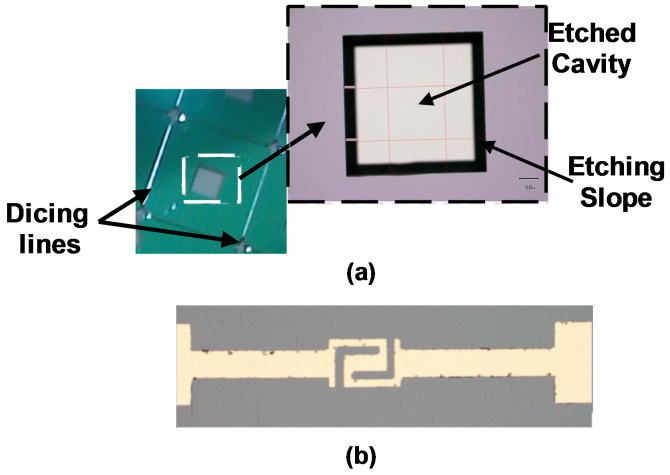

FIGURE 4.5: Fabricated microhotplate and microheater (a) Single Die after bulk micromachining using TMAH (b) Top view of S shape microheater

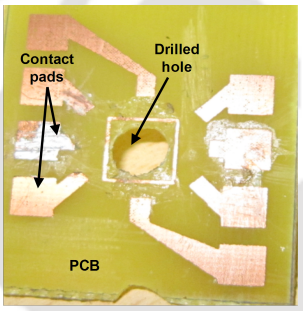

FIGURE 4.6: PCB with contact pads and drilled hole

4.2 Characterization Setup

After the wafer level fabrication of microhotplate, individual devices are diced and electrical contacts were made using conductive silver epoxy paste. The contacts are activated by curing the die in oven at 88°C for 2 hours. Subsequently, the die is mounted on the PCB for testing. A hole is drilled into the PCB to alleviate the direct thermal losses to the PCB (see Fig. 4.6). To further minimize the thermal losses to PCB, ceramic wool is placed between PCB and die. Ceramic wool is a standard thermal insulation material with very low thermal conductivity (0.8 $\frac{\mathrm{W}}{\mathrm{mK}}$) and can withstand upto 1300°C. An additional advantage of using ceramic wool as a base is that it will allow the microheater to withstand temperature higher than PCB melting temperature. The die is mounted on finished PCB as shown in Fig. 4.7.

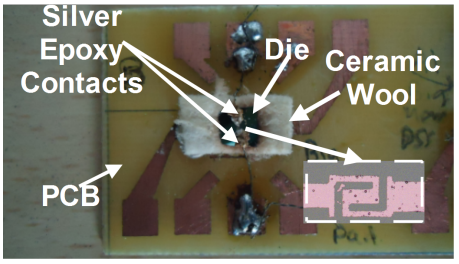

FIGURE 4.7: PCB mounted die, with die resting on ceramic wool. Inset shows the expanded view of the S-Shape microheater

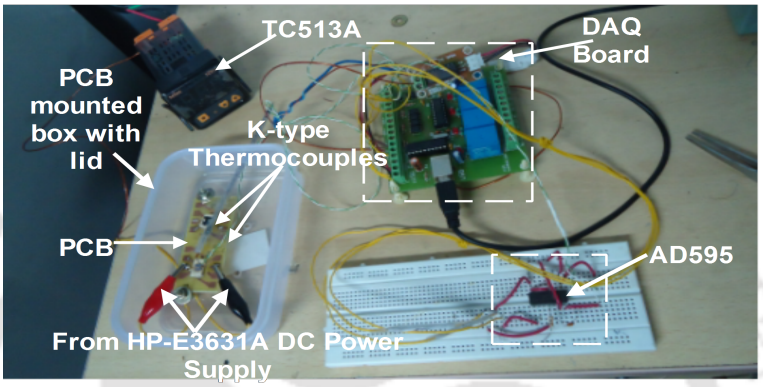

FIGURE 4.8: Test setup with Data Acquisition (DAQ) board

A test setup (Fig. 4.8) is made using a closed plastic box with an arrangement to fix the PCB in it. For the temperature measurement, K-type thermocouples are used and their outputs are feed to an AD595 instrumentation amplifier IC that has provision for cold junction compensation. The analog output of AD595 is connected to a Data Acquisition (DAQ) board which has a 10 bit ADC resolution. A visual basic based program is used to control and acquire the data from the DAQ board. In addition, TC523A temperature controller is used to monitor the temperature inside the testing box. HP E3631A DC power supply is used for supplying the current/voltage to the microhotplate.

4.3 Results and Discussion

In this section, the characterization results obtained for the fabricated microhotplate are presented. Prior to fabrication, the microhotplate design was optimized using FEM simulations. In this section, results of fabricated microhotplate are compared with the

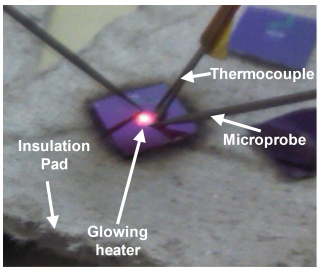

FIGURE 4.9: Direct testing of microhotplate using microprobes

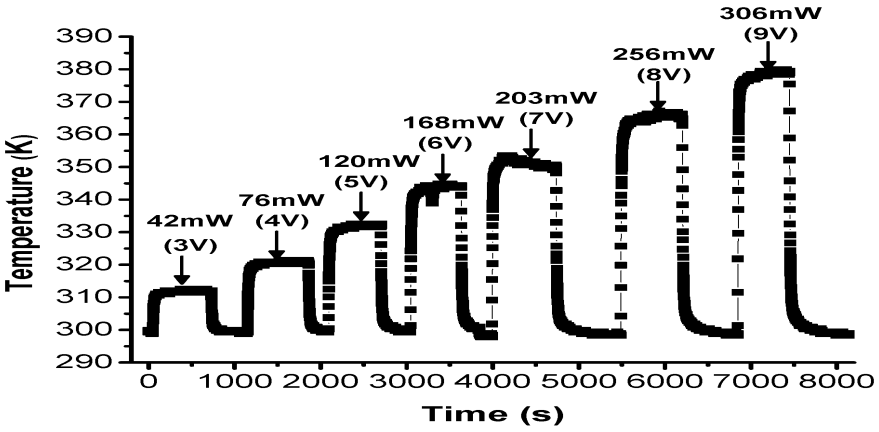

FIGURE 4.10: Experimentally obtained transient profile for different input power

simulation results and with the model developed using triangular approximation (Chapter 2, Section 2.6). The characterization results of fabricated microhotplate are also compared with other reported microhotplates.

When a constant 2 V is applied across the microheater, no appreciable temperature is observed, therefore, the input potential is varied from 3 to 9 V in 1 V steps. With 10 V applied, a maximum temperature of 393 K is observed, just before the contact failure. The current drawn is 38 mA and hence the power consumption is 380 mW. In order to overcome the temperature limit set by silver epoxy contact and to verify whether the microhotplate can operate at higher temperatures, we have made separate measurement, where the microhotplate is probed directly with micro-probes (see Fig. 4.9), and a temperature >694 K is obtained when a current of 175 mA is applied. From Fig. 4.9, it may be concluded that the present microhotplate can achieve temperature higher than 694 K.

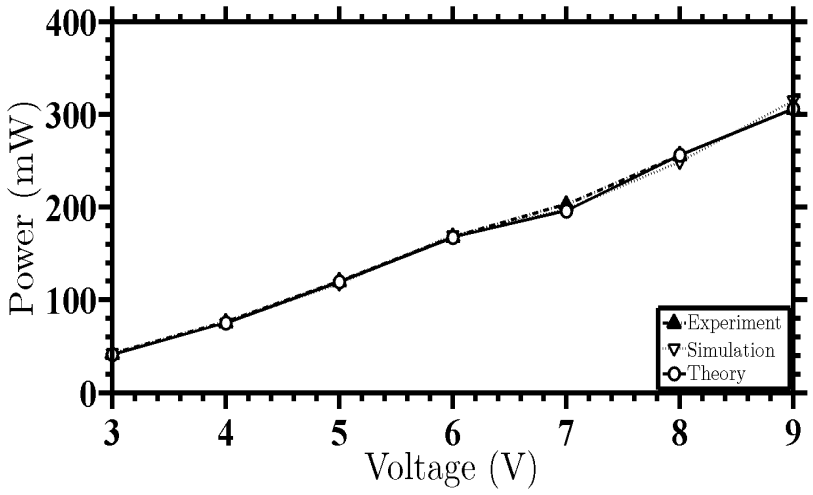

FIGURE 4.11: Comparison of power values obtained by experiment, simulation and theory

Figure 4.10 shows the temperature profile with respect to time and with different applied power levels. Each measurements are carried out for sufficiently long time, to accurately measure the steady-state temperature and to minimize the inaccuracies due to heater resistance drift. A comparison of power values obtained by experiment, simulation and theory are shown in Fig. 4.11. The simulations and theoretical results are in close agreement with experimental results. The fabricated microhotplate is able to operate at a temperature of 379 K with an applied power of 306 mW, whereas, when compared to [4], 481.66 mW power is required to obtain the similar temperature. Heating efficiency is defined as power per active area (PPAA) or power per heater area [14, 65]. It gives the information about the power required by a microhotplate to heat up a 1 μm^2 area by desired temperature. The heating efficiency of the present microhotplate is $1.85 \times 10^{-6} W/\mu m^2$, which is much lower when compared to a smaller circular active area of $\pi 12^2 \mu m^2$ [59] where a heating efficiency of $9.67 \times 10^{-6} W/\mu m^2$ was obtained. The heating efficiency of present work is comparable to a value $1.18 \times 10^{-6} W/\mu m^2$ that was obtained in [3], for an active area of $(345 \times 385 \mu m^2)$ in [3], which is much smaller than the present work. However, the present microhotplate is not the best energy efficient one. Mele et al. has developed a microhotplate with a PPAA of $0.171 \times 10^{-6} W/\mu m^2$ [15].

4.4 Summary

A square microhotplate with S Shaped microheater was designed, fabricated and tested. The performance of microhotplate is comparable to some earlier reported microhotplates, however, microhotplates with similar dimensions have been reported recently with much lower power consumption owing to their lower membrane area.

5

Model for Selectivity and Sensitivity of Nanowire Transistor Based Gas Sensors

IMPROVING the performance of microhotplate helps in enhancing the linearity, response time, sensitivity and selectivity of gas sensors. Further, design of a microhotplate depends upon the gas sensor performance specifications. For example, the sensitivity of a semiconductor type sensor among other parameters, also depends upon the number of adsorption site participating in the chemisorption process. For a target gas, the probability of active participation of these adsorption site is highest, at a particular temperature. Moreover, an uniform temperature across the sensor (semiconductor) surface will increase the chemisorption probability, resulting in an increased sensitivity. Therefore, a microhotplate which will be used for part per million (ppm) level sensing can be designed with

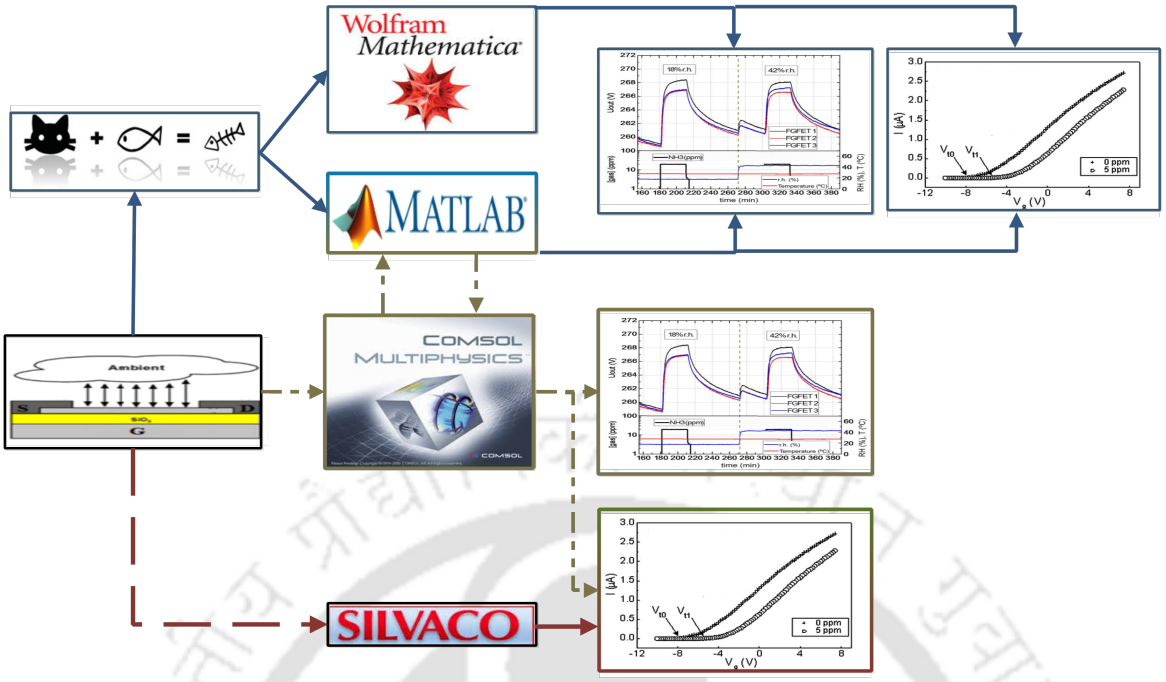

FIGURE 5.1: Various Simulation/Modeling Methods for Gas Sensor. Identified paths I, II and III are shown in blue, green and red color respectively. Transient and steady state responses are for illustration purpose [18, 19].

a slightly lower temperature uniformity as compared to a microhotplate designed for part per billion (ppb) level sensing. The various method of tuning the temperature uniformity of a microhotplate and similarly, other performance parameters are dealt in the previous chapters, hence, the focus of this chapter is to understand the sensing mechanism of a semiconducting type gas sensors. Further, this chapter targets to develop an analytical model for optimizing the various sensor design parameters which will ultimately lead to an efficient sensor.

In Fig. 5.1 the various routes for gas sensor modeling/simulation are identified. Computational software program such as Matlab/Mathematica can be used for simulating chemisorption induced surface bending, surface potential and theoretical verification of current through sensor. For analyzing the field effect based sensors response in steady state, Technology Computer Aided Design (TCAD) software such as SILVACO or Sentaurus can be used. Whereas, for the transient analysis of these field effect based sensors, one can use simulation packages such as COMSOL and Matlab in conjunction.

The various method of simulating a gas sensor can be classified into three paths, and each path includes the device physics involved when a sensor is exposed to a gas. Exposure

of semiconductor surface to target gas will induce chemisorption effect, which leads to the change in device characteristics such as channel/carrier concentration modulation, Schottky barrier formation or contact transformation. As shown in Fig. 5.1 the path one involves, the sensor's governing equations, which are often solved simultaneously to analyze the device response to the targeted ambient. These coupled equations can be solved iteratively using mathematical packages such as Mathematica or Matlab. The second path identifies an another possible approach, in which, the influence of ambient gas on the semiconductor surface can be analyzed in the steady or transient state. The second path defines the method to simulate the sensor characteristics by combining FEA and/or FDM/FEM simulations. The surface bending and chemisorption effect is captured using mathematical packages such as Matlab/Mathematica. And the device equations can be handled with a FEA simulators such as COMSOL. By using both the software in conjunction, where the surface bending results from the mathematical package will be called to the FEA simulator for obtaining the sensor response. Therefore, this path can lead to the extraction of both steady state and transient response. In the third path, the gas sensing response can be obtained by defining the sensor structure and material properties in a TCAD simulator and considering the steady state surface bending which may lead to the sensor's steady state response.

Modeling of a field effect transistor (FET) employed for gas sensing application [128–130] is helpful in understanding the sensing mechanism. Moreover, it enables the sensor designers to decide upon the sensor structure and its parameters such as contact material, channel dimensions, semiconductor doping and biasing conditions for achieving maximum sensitivity. In the following sections of this chapter, with the aim of developing an analytical model for field effect transistor (FET) based gas sensor, we have employed the first route. The analytical model is developed for the analysis and design optimization of the device. The developed model takes a system level modeling approach, where the cause (surface activity) and their effect on the device characteristics are related, by unifying the effect of gas exposure on the sensor surface and its effect on the device response. Apart from design optimization, the developed model can help sensor designers to predict the sensitivity and selectivity with respect to different gases.

Models are available in literature from gas-surface interaction perspective, which elaborates the chemisorption induced surface states or from device perspective, which explains the change in electrical characteristics. In one of the sensor modeling approaches previously reported [24, 131–134], Soares et al. have developed a model for tin dioxide nanowire FET and obtained sensor currents with and without gas exposure [131]. A more accurate model can be obtained by taking into consideration the nanowire width modulation due to surface depletion. The GaN nanowire device model presented by Cha et al. takes the width modulation into account. In some gas sensor models, ohmic contacts are assumed, however, the contacts can translate from ohmic to rectifying, depending upon the nature of gas (oxidizing or reducing) [135]. Further, in many modeling approaches, the correlation of gas concentration with the surface depletion width is not mentioned. In this chapter, a mathematical model is developed for a nanowire gas sensor by considering rectifying contact [20] and width modulation.

For improving any sensor design, an understanding of sensing mechanism is essential. Therefore, it is important to relate the cause (reaction on the surface) to the change in device characteristics. Sensor modeling is challenging because, in order to understand the sensing mechanism, the transcendental current equations and surface charge equations are to be solved simultaneously to find a self consistent solution. Efforts are made to unify the effect of gas exposure on the gas sensor surface and its effect on the device response, hence presenting a detailed explanation to the sensing mechanism.

5.1 Sensor Structure

The device structure investigated in this section is a back gated field effect device [19] (Fig. 5.2), with n-type Zinc Oxide (ZnO) nanowire as the sensing layer. A heavily doped p-substrate act as gate, silicon dioxide (SiO_2) as gate oxide and Ni/Au metal is used for source and drain contacts. The work function difference between the contact metal and the ZnO leads to the formation of non-ohmic contacts with depletion widths (d_{SC} and d_{DC}). The depletion width due to the oxide-semiconductor work-function difference is depicted as d_2 in Fig. 5.2a.

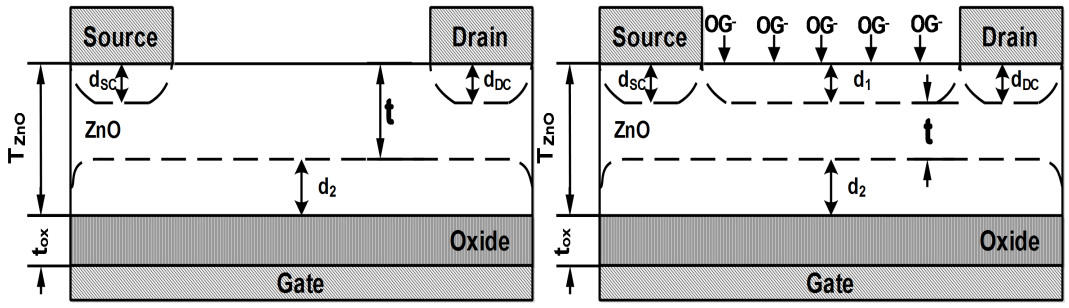

FIGURE 5.2: n-type nanowire FET with (a) No bias and no exposure and (b) No bias but exposure to oxidizing gas. OG^- represents the ionized oxidizing gas molecules on the semiconductor surface. d_{SC} and d_{SD} are the depletion width at source and drain contacts, respectively.

As this device is exposed to an oxidizing gas (see Fig. 5.2b), the electron are extracted from the surface by the adsorbed species, which results in the formation of depletion width (d_1). As long as no bias is applied, all the depletion widths will remains the same. From Fig. 5.2a and 5.2b, it can be inferred that when the FET device is exposed to an oxidizing gas, its channel thickness is modulated.

For simplifying the modeling approach, the sensors contacts can be treated Schottky diodes and the middle portion of wire can be treated as a back gated FET [19] with the internal drain (V_{Di}) and source (V_{Si}) voltages. Fig. 5.3a depicts the equivalent circuit of the sensor. The back gated FET is modeled as depletion mode transistor. When a drain and source biasing is applied, the channel region is tapered in shape and the charge in channel region can be calculated from effective thickness of the channel available for conduction $[T_{eff} - d_2(y)]$, length of the channel (L) and its width (W) [136]. The depletion width $[d_2(y)]$ can be calculated by relating the voltage at a position y and can be written as [135],

$$V_G - V_{FB} - V(y) = \frac{qN_d d_2^2(y)}{2\varepsilon_{zno}} + \frac{qN_d W_{eff} d_2(y)}{C_{ox}} \tag{5.1}$$

Where W_{eff} effective width of the channel, $C_{ox} = \frac{2\pi\varepsilon_{ox}}{\ln((2tox+(T_{zno}/2))/(T_{zno}/2))}$ is the gate oxide capacitance per unit length [137], voltages V_G, V_{FB}, are gate and flatband voltage, respectively. V(y) is potential at a distance y. From Eq. 5.1, the depletion width can be written as,

$$d_2(y) = -\frac{W_{eff}\varepsilon_{zno}}{C_{ox}} + \sqrt{(\frac{W_{eff}\varepsilon_{zno}}{C_{ox}})^2 - \frac{2\varepsilon_{zno}(V_G - V_{FB} - V(y))}{qN_d}} \tag{5.2}$$

The voltage at which the nanowire will be fully depleted (see Fig. 5.3b) can be calculated by substituting $d_2 = T_{eff}$, and $V(y) = 0$ in Eq. 5.2. The required gate voltage ($V_G = V_P$) can be written as,

$$V_P = V_{FB} - (\frac{qN_d}{2\varepsilon_{zno}})t_{eff}^2 - \frac{qN_dW_{eff}}{C_{ox}}t_{eff} \tag{5.3}$$

The current through the FET can be written as

$$I_D = \alpha(T_{eff} - d_2(y))\frac{dV}{dy} \tag{5.4}$$

Where $\alpha = qN_dW_{eff}\mu_n$, $\mu_n = \frac{\mu_{n0}}{1+\frac{\mu_{n0}}{V_{sat}}E}$

In the linear region of operation ($V_{FB} > V_G > V_P$ and $V_D < V_G - V_{FB} + V_{Dep}$), FET current can be obtained by integrating Eq. 5.4 from source to drain such that,

$$\begin{aligned} I_D &= \frac{\alpha}{3L}\Bigg(3T_{eff}(V_{Di} - V_{Si}) + \rho\Bigg(3(V_{Di} - V_{Si}) \\ &\quad +\gamma(2V_{Si} + \delta) - \beta(2V_{Di} + \delta)\Bigg)\Bigg) \end{aligned} \tag{5.5}$$

With $\rho = \frac{W_{eff}\varepsilon_{zno}}{C_{ox}}$, $\tau = \frac{(qN_dW_{eff})}{C_{ox}}$and

$\beta = \sqrt{1 + \frac{2(V_{Di}+V_{FB}-V_G)}{\rho\tau}}$, $\gamma = \sqrt{1 + \frac{2(V_{Si}+V_{FB}-V_G)}{\rho\tau}}$

$\delta = 2(V_{FB} - V_G) + \rho\tau$

When the gate voltage satisfy the condition $V_G \geq V_{FB}$ and drain voltage is less than ($V_G - V_{FB}$), along with the current through the channel (see Fig. 5.3d), the charge accumulation near the oxide-ZnO interface will result in an accumulation current component also. Hence, the current under these biasing condition can be presented as [137],

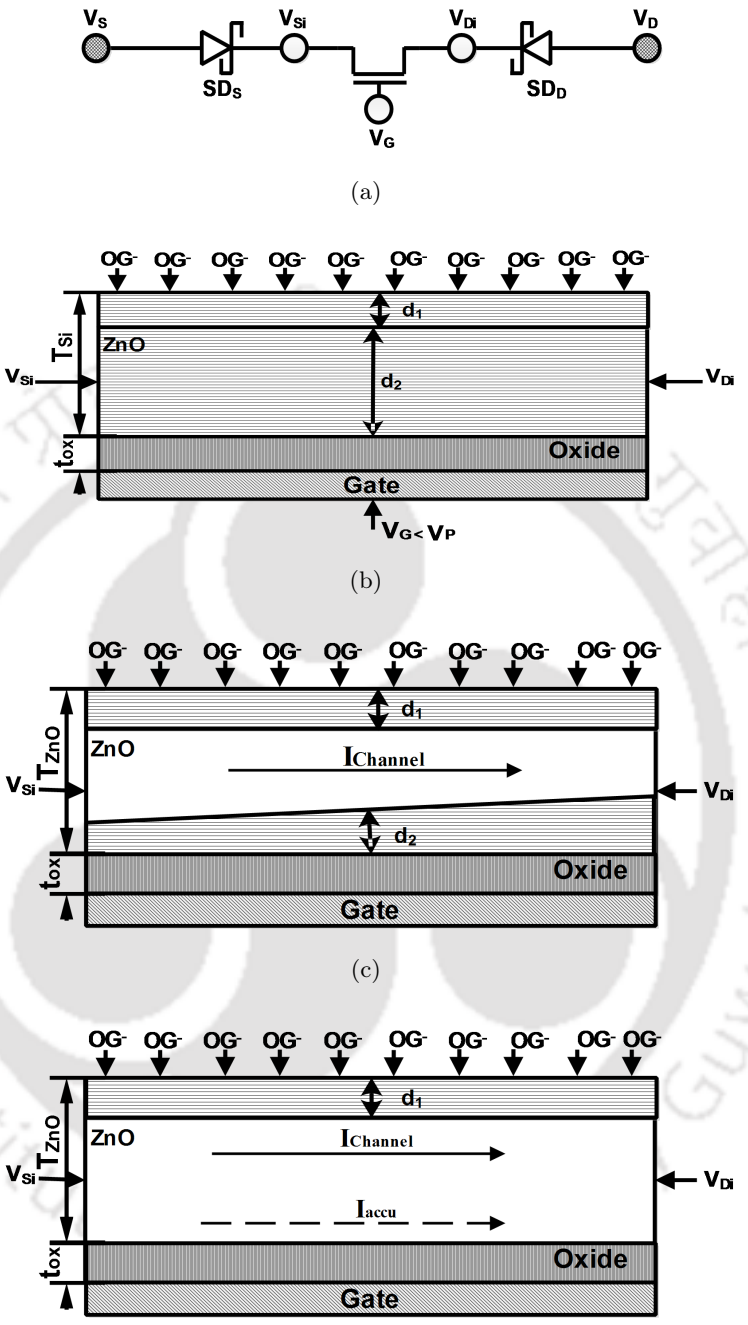

FIGURE 5.3: (a) Modeling the ZnO nanowire sensor where nanowire contacts are treated as Schottky diodes and middle region as depletion type FET [20], (b) fully depleted ZnO NWFET with $V_G < V_P$, (c) equivalent model of the ZnO FET under oxidizing gas exposure and with $V_G > V_P$ and $V_D > 0$ (d) accumulation of charge with $V_G \geq V_{FB}$ and $V_D < V_G - V_{FB}$. The channel current ($I_{Channel}$) and accumulation current (I_{accu}) are shown with arrows.

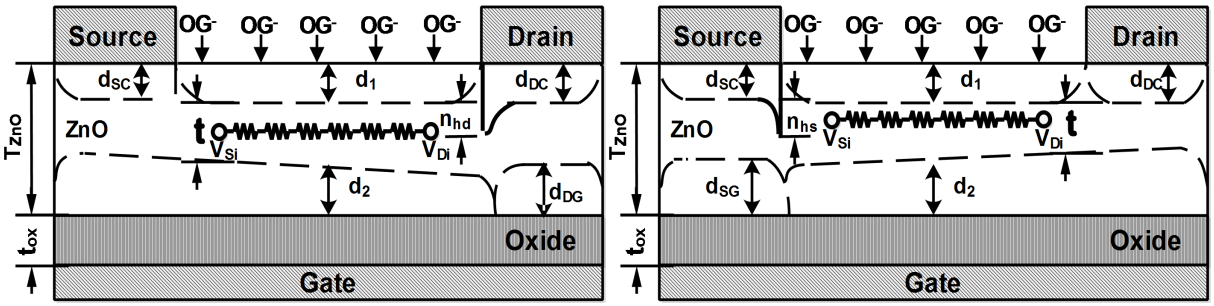

(a) With negative drain bias, exposure to oxidizing gas (b) With positive drain bias and exposure to oxidizing gas

FIGURE 5.4: Back Gated FET structure under different operating condition. d_x is the depletion width, t is the non depleted conducting region, n_{hd} and n_{hs} are the notch height at the drain and source edges, respectively. T_{ZnO} is the diameter of nanowire and T_{ox} is the gate oxide thickness

$$I_{DA} = \frac{\alpha T_{eff}}{L}(V_{Di} - V_{Si}) + \frac{\mu_n C_{ox}}{k1L}((V_G - V_{FB})(V_{Di} - V_{Si}) - \frac{(V_{Di} - V_{Si})^2}{2}) \quad (5.6)$$

5.2 Device Under Gas Exposure and Bias Voltage

Fig. 5.4a shows the change in depletion widths with respect to the negative drain bias applied. The drain Schottky diode will be reverse-biased and the source Schottky diode will be forward-biased. Due to the negative polarity of applied bias, d_2 will be of wedge shape with a higher width on the source side. Also, since $V_{Di}<V_{Si}$, depletion width at the edge of drain contact will increase and results in a notch formation, as shown in in Fig. 5.4a where the height of this notch is depicted as n_{hd}. Under the same negative drain biasing condition, when the FET is exposed to oxidizing gas, the surface depletion width (d_1) will also be present as shown in Fig. 5.4a. Under this conditions, the drain current is modulated in accordance to the width of depletion width d_1, which in-turn depends on the concentration of the gas. The effect of contact on the sensor performance is evident here. Whatever may be the biasing conditions, the sensor current is regulated by the reverse biased Schottky diode [135]. The current through the diode can be written as [20],

$$I_{SD} = AD_1 \exp^{\left(\frac{-qV_{si}}{D_{11}}\right)} \tag{5.7}$$

Where $D_{11} = \frac{E_{00}}{\left(\frac{E_{00}}{kT} - \tanh\left(\frac{E_{00}}{kT}\right)\right)}$;

and quantities E_{00} and E_0 are given as,

$E_{00} = \frac{qh}{4\pi\sqrt{\frac{N_d}{m*\varepsilon_{zno}}}}$; $E_0 = E_{00}\coth\left(\frac{E_{00}}{kT}\right)$.

Where h, A, m*, ϕ_b and R are Planck constant, nanowire cross-sectional area, effective mass of electron, Schottky barrier height and Richardson constant respectively.

Fig. 5.4b depicts the depletion widths when a positive drain bias is applied. Under this biasing condition, the drain Schottky diode is forward biased and source diode is reverse biased. Similar to negative drain biasing condition, the depletion width shape d_2 will be altered and a notch will be present at the source side. As the drain bias is increased further, the drain current will increase. It will increase both the internal source voltage (V_{Si}) and the notch height (n_{hs}). Hence, under the positive drain biasing, the drain current is limited by the source Schottky diode or in other words, it is limited by the depletion width at the source side. For moderately doped or thin nanowire sensors, the notch heights will be able to modulate the effective channel width, resulting in current saturation.

5.3 Estimation of Surface Depletion Width, Potential and Band Bending

The exposure of ZnO surface to Nitrogen Dioxide molecules decreases its surface electron concentration (see Fig. 5.5a) and the gas-surface interaction can occur according to the following reaction [130],

$$NO_2 \uparrow + e^- \rightarrow NO_2^- \tag{5.8}$$

This interaction gives rise to the surface depletion width (d1) which is an important parameter in the sensor design. The knowledge of surface depletion width can help the sensor designers while deciding on parameters such as channel thickness and doping concentrations, for maximizing sensor sensitivity. The interactions between gas molecules and semiconductor surface can be explained with the help of Wolkenstein adsorption theory. Wolkenstein adsorption theory gives a relationship between the electronic exchange between the gas and semiconductor surface. The qualitative understanding of the gas-surface electronic exchange can be obtained with the knowledge of surface parameters. Many a times the values of numerous parameters for a particular semiconductor are often not available in literature. Therefore, we have followed another approach, in which, the shift in pinch off voltages due to oxidizing gas exposure is used to calculate the depletion width (d_1). This relation is presented first. Further, with the help of model presented by Rothchild et al. [25], an expression is derived for estimating the surface potential and surface band bending.

The surface depletion width, which is due to the adsorption of gas molecules onto the semiconductor surface can be calculated by relating the shift in pinch off voltage. The surface depletion width can be written as,

$$d_1 = \zeta_1 - \sqrt{\zeta_2 + \zeta_3(V_{FB} - V_P)} \tag{5.9}$$

Where $\zeta_1 = \frac{(C_{ox}+2\varepsilon_{zno})T_{zno}+\varepsilon_{zno}W}{C_{ox}+4\varepsilon_{zno}}$

$\zeta_2 = \frac{\varepsilon_{zno}^2(W-2T_{zno})^2}{(C_{ox}+4\varepsilon_{zno})^2}$

$\zeta_3 = \frac{2C_{ox}\varepsilon_{zno}}{qN_d(C_{ox}+4\varepsilon_{zno})}$

The exposure of surface to the oxidizing gas will increase the surface depletion width (d_{1expo}) and a relation between the surface depletion width with no-exposure and with exposure can be written as,

$$d_{1expo} = d_{1noexpo} + \Delta \tag{5.10}$$

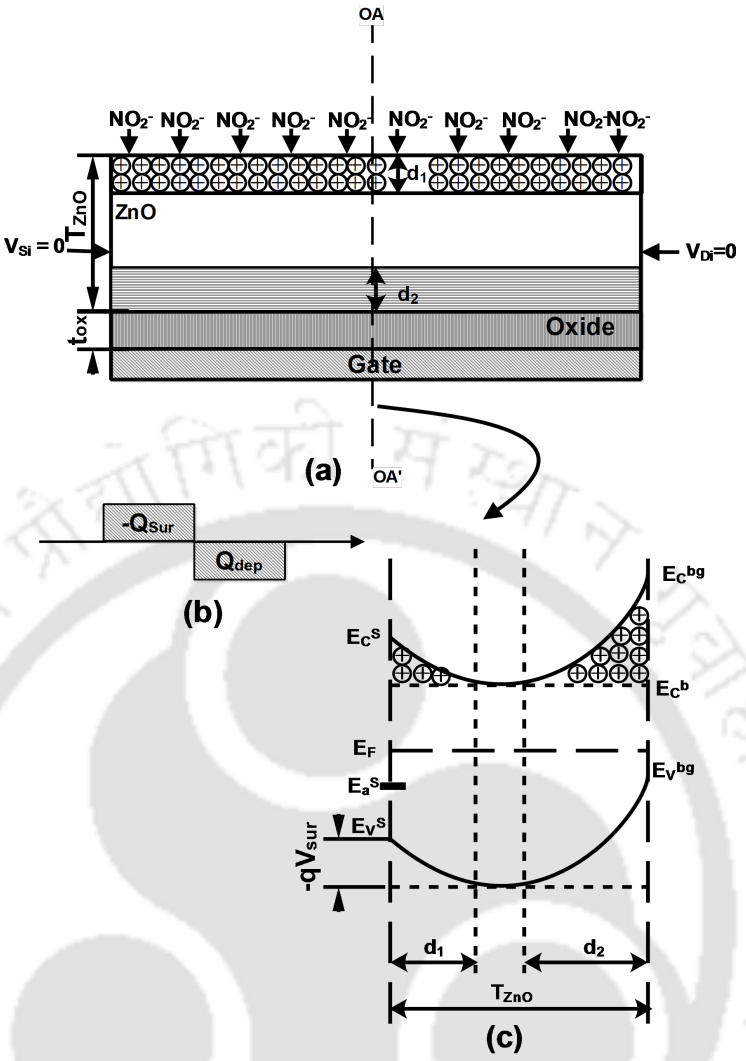

FIGURE 5.5: (a) FET Sensor under no biasing and with gas exposure (b) charge distribution on the surface and inside depletion width (c) energy-band diagram of channel along the cutline (OA – OA′) direction. E_C^S, E_a^S and E_V^S are the conduction band, surface state and valance band edge at the surface. E_C^{bg} and E_V^{bg} are the conduction band and valance band edges at the ZnO-oxide interface.

Where Δ is the increment in width due to gas exposure. After the determination of depletion width value, surface potential and surface bend banding can also be determined.

Fig 5.5b depicts the charge neutrality condition, i.e, under steady state, the charge acquired by the ionized gas molecules and charge in the depletion region (Q_{dep}) is equal, using this, the band bending can be calculated. Moreover, the electron exchange between oxidizing gas molecules and semiconductor surface can also be explained from the energy band diagram as shown in Fig. 5.5c. The gas-surface exchange will cause the band bending and the surface potential can be related to the surface depletion width by the following relation [25],

$$
\begin{aligned}
Q_{dep} &= \sqrt{2}qN_dL_d\left(\operatorname{sech}\left(\frac{E_g-\left(E_c^b-E_f\right)}{2}\right)\right. \\
&\quad \times\cosh\left(\left(\frac{E_g}{2}-\left(E_c^b-E_f\right)\right)+\frac{V_{sur}}{kT}\right) \\
&\quad \left.-\frac{V_{sur}}{kT}\tanh\left(\frac{E_g}{2}-\left(E_c^b-E_f\right)\right)-1\right)^{\frac{1}{2}} \qquad (5.11)\\
&= qN_dd_1 \qquad (5.12)
\end{aligned}
$$

where $L_d=\sqrt{\frac{\varepsilon_{zno}kT}{q^2N_d}}$ and $\left(E_c^b-E_f\right)=kT*\ln\left(\frac{3.12*10^{28}\left(\frac{2\pi m_e kT}{h^2}\right)^{\frac{1}{2}}}{N_d}\right)$

Surface potential (V_{sur}) can be calculated by solving Eq. 5.11. Once the value of surface potential known, the surface band bending ($(E_c^s-E_a^s)$) can be calculated using the relation [25],

$$
\left(E_c^s-E_a^s\right)=kT*\ln\left(\frac{-W_1W_2+\sqrt{4W_1W_2W_3+(W_1W_2-W_4)^2}+W_4}{2W_1W_3}\right) \qquad (5.13)
$$

with

$W_1=\frac{1}{g_{aw}}e^{\frac{V_{sur}-\left(E_c^b-E_f\right)}{KT}}$;

$W_2=-\beta_{0w}N^*P(g_{aw}e^{\frac{\left(E_c^b-E_f\right)-V_{sur}}{KT}})$;

$W_3=\beta_{0w}P(N^*+Q_{dep})$;

$W_4=W_3+Q_{dep}+(1+\frac{V^-}{g_{aw}V_{0w}}e^{\frac{V_{sur}-\left(E_c^b-E_f\right)}{KT}})Q_{dep}$;

$\beta_{0w}=\frac{\kappa_wS_{0w}e^{\frac{q_w}{KT}}}{(V_{0w}\sqrt{2\pi M_wKT})}$

Alternatively, it may be noted that with the knowledge of chemisorbed site occupancy (neutral and charged), similar procedure can be applied to find the surface potential first, and thereafter the surface depletion width.

TABLE 5.1: Device parameters used in the result verification [19, 22, 23]

Parameter	Value
Zinc Oxide bandgap (E_{g300})	3.37eV
Permittivity of ZnO nanowire (ϵ_{ZnO})	8.7
Permittivity of silicon oxide (ϵ_{ox})	3.9
Electron mobility(μ_n)	$42 \times 10^{-4} \frac{m^2}{Vs}$
Doping density (N_d)	$1.59 \times 10^{23} m^{-3}$
Nanowire diameter (T_{ZnO})	$120 \times 10^{-9} m$
Channel length (L)	$7 \times 10^{-6} m$
Channel width (W)	$120 \times 10^{-9} m$
Oxide thickness (t_{ox})	$500 \times 10^{-9} m$
Temperature (T)	300K
Effective mass of electrons ($\frac{m^*}{m_0}$)	0.27
Pinch-off voltage (V_{P0}) at no exposure	–7.9V
Pinch -off voltage (V_{P5}) at 5ppm NO_2 exposure	–5.2V

5.4 Model Verification

The surface depletion region under exposure to oxidizing gas can be calculated using Eq. 5.10 and the sensor current can be calculated by equating Eq. 5.5 and Eq. 5.7. Irrespective of biasing conditions, Schottky diode current must be equal to the FET current. The internal voltage V_{Di} and V_{Si} can be calculated by iteratively solving the FET current and Schottky diode current [20] and using ϕ_b as a fitting parameter [131]. The various device parameters used for the calculations are listed in Table 5.1. A comparison of developed model with reported experimental current characteristics is shown in Fig. 5.6 and typical errors are within 5%. As can be seen from Fig. 5.6, because of the positive drain bias, the electrons under the drain will be locally depleted and creates a pinch-off effect which restricts the current [138], leading to an asymmetrical $I_D - V_D$ curves. From sensing application point of view, the device under investigation has shown maximum sensitivity, when biased with negative drain voltage.

TABLE 5.2: Parameters used for surface potential and band bending estimation [24, 25]

Parameters	Value
Oscillation frequency of the charged chemisorbed state (V^-)	$1 \times 10^{13} s^{-1}$
Degeneracy factor for the chemisorption-induced states (g_{aw})	2
Oscillation frequency of the neutral chemisorbed state (V_{0w})	$1 \times 10^{13} s^{-1}$
Atmospheric pressure (P)	1
Density of chemisorption sites (N^*)	$1 \times 10^{19} m^2$
Sticking probability (κ_w)	1
Effective area of a chemisorbed adparticle (S_{0w})	$1 \times 10^{-11} m^2$
Adsorption heat for the neutral chemisorbed state (q_w)	0.1eV

The effect of gas exposure on the threshold voltage is evident from the $I_D - V_G$ characteristics when tested in argon ambient which represents 0 ppm of oxidizing gas and in 5ppm NO_2 ambient, which is shown in Fig. 5.7. The shift in the pinch-off voltage can be attributed to the channel thickness modulation caused by the change in the surface depletion width (d_1). Sensitivity analysis can be carried out for a given gate and drain-source voltage by solving Eq. 5.5 and Eq. 5.7 with no-exposure and exposure condition, the term sensitivity here is defined as,

$$\text{Senstivity} = \frac{I_{0ppm} - I_{5ppm}}{I_{0ppm}} \Big|_{V_D, V_G} \tag{5.14}$$

By employing Eq. 5.11 and 5.13, a correlation between gas exposure and its effect on the semiconductor surface can be estimated. Parameters required for the evaluations were taken from literature and their values are summarized in Table 5.2. Some parameters for ZnO were assumed as they were not available in literature. Under exposure to 5ppm of NO_2, the surface potential obtained is 40mV. The fermi is 0.08eV below conduction band and $(E_c^s - E_a^s) = 0.058$eV. This information can now be used to calculate the activation energy. The activation energy ($E_A = \left(E_c^b - E_f\right) + qV_{sur}$) for 5ppm NO_2 exposure is 120meV. From sensor design point of view, the activation energies of other gases can also be calculated in similar way. An comparison of these energies may help in predicting their selectivity to the given sensing material. In [19], experimentally

calculated activation energies were compared to explain the higher sensitivity of NO_2 over NH_3 ($E_{ANO_2} > E_{ANH_3}$).

5.5 Summary

This chapter identifies various routes for simulating and modeling a semiconducting FET gas sensor response. By employing one of the route, a modeling approach for gas sensor based on n-type nanowire transistor has been presented. In order to improve modeling accuracy, transistor equations were derived by taking width modulation and rectifying contact aspects into consideration. The surface depletion width in the presence of oxidizing gas is the cause which results in the sensing response. An equation for surface depletion width was derived and it relates effect of gas exposure on device characteristics. The depletion width can be calculated either from the knowledge of chemisorbed site occupancy (neutral and charged) or from the shift in pinch-off voltage. The obtained depletion width was used to find the surface band bending and the surface potential by applying Wolkenstein adsorption theory and charge neutrality principle. Alternatively, the surface depletion width can be calculated from the surface potential and band bending values. The model was verified against the experimental results, reported elsewhere and it matches closely with the experimentally reported current characteristics of single ZnO nanowire FET. Apart from aiding the sensor design and sensitivity analysis, the developed model can be used to predict the selectivity of sensor to different gases. For this, surface potential values for different oxidizing gases were used to calculate the activation energies, which were compared for predicting of selectivity of the sensor. The presented modeling approach is simple and can be easily extended to other metal oxide transistors also.

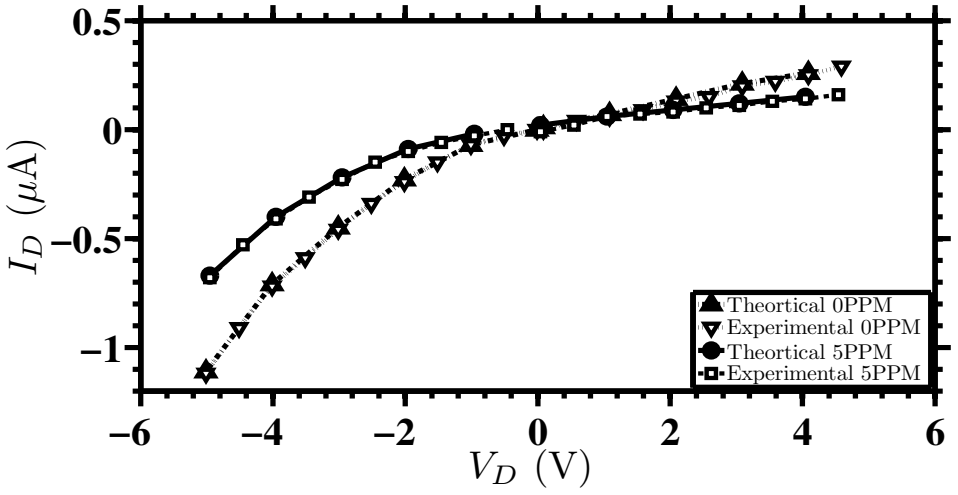

FIGURE 5.6: Comparison of theoretical and experimental current ($I_D - V_D$) characteristics obtained in argon ambient (which represents 0 ppm of oxidizing gas) and NO_2 (5 ppm) ambient. Gate bias is kept constant at 0V [19].

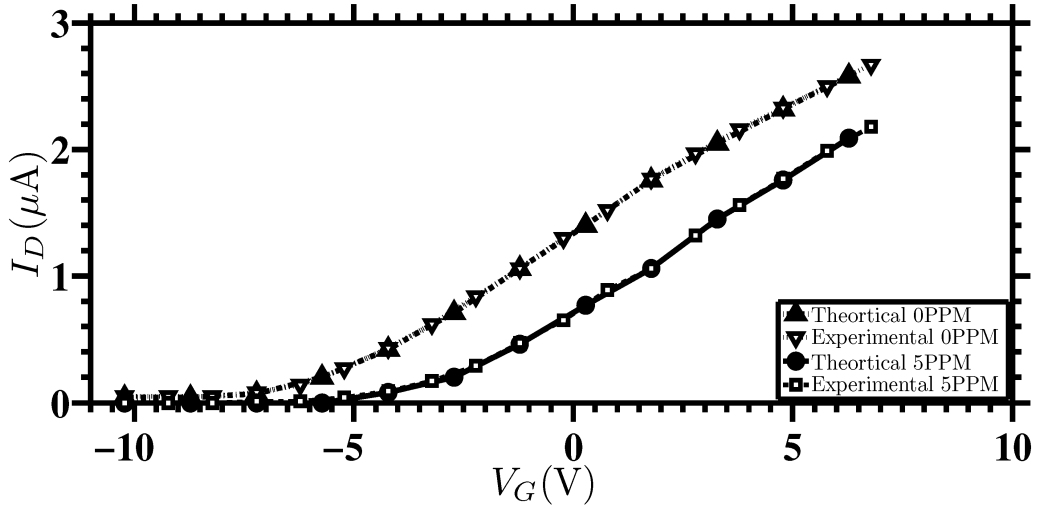

FIGURE 5.7: Comparison of theoretical and experimental current ($I_D - V_G$) characteristics obtained in argon ambient (which represents 0 ppm of oxidizing gas) and in NO_2 (5 ppm) ambient. Drain biasing is kept constant at –5V. [19]

6

Conclusion

SINCE the microhotplate is an essential component in various applications, improving their performance will increase the overall efficiency of their application domain. This thesis identifies various application domains of microhotplate and briefly explores the performance expectation of each domain. From microhotplate designer perspective, we have identified the major components of microhotplate and the tradeoff among the performance parameters. This will help the designer to focus on the microhotplate design, after identifying the key requirement of the application domain. In order to systematically identify various key design parameters, materials and dimensions to be employed, several simulation studies were carried out.

The aim of first study was to identify the contribution of individual components to the total heat loss and their region of dominance with respect to the temperature spectrum.

The identification of these loss mechanism is important for simplifying the simulation studies or analytical modeling. The convection loss mechanism has as much as 30% contribution of total heat losses. It has been found that the nitride layer, which is used for providing the electrical insulation has resulted in an additional 56.6% of power demand for a heater operating at 620K. This is a significant power intake for any battery operated, hand held devices for a continuous monitoring applications such as gas sensors or air quality monitors. We have utilized such information in choosing a particular loss component while developing subsequent simulations or analytical studies. For a microhotplate, Membrane to heater (MHR) ratio is another important parameter which influence the performance of microhotplate. The effect of MHR was systematically analyzed and the tradeoffs that exist among them were identified. With a large MHR value (MHR=7), improvements of 44% and 56.5% have been achieved in power and temperature uniformity, respectively. However, the vertical deflection has increased from 2.1 μm (with MHR=2) to 7.3 μm (with MHR=7). The time response has also been deteriorated with a large MHR value. The time response has increased from 0.37 ms (with MHR=2) to 2.5 ms (with MHR=7). The MHR value in the range of $4-5$ give a better balance with respect to power, temperature uniformity, displacement, and thermal time response. Hence, giving preference to power and temperature uniformity, an MHR value of 5 is utilized consistently in all subsequent simulations and analytical model development, unless otherwise specified.

While carrying out the literature survey, we have identified that though the blanket deposition of insulation layer is a common practice. However, it deteriorates the microhotplate performance. During simulation studies we have found that by employing an optimized insulation dimensions the performance of microhotplate improves, especially its temperature uniformity. Nevertheless, the improvement in the temperature uniformity was also accompanied by increased power consumption. An analytical model is developed for the optimization of the insulation nitride area. The model is compared with the Finite Element Method (FEM) simulations and the results are in close agreement, with errors within 5%. Because of the modular nature of the developed model, the thermal losses in the insulation layer are also estimated separately. Since, power consumption of the microhotplate depends on the thermal mass, an optimized dimensions

of heat spreader can bring multiple advantages such as better temperature uniformity, higher temperature and minimized power overhead. Compared to insulation nitride dimensions of 250 μm $\times$ 250 μm $\times$ 8 μm, for attaining a temperature of 550 K, an optimized insulation nitride dimension of 120 μm $\times$ 120 μm $\times$ 8 μm has improved the temperature uniformity by 40.1%, power consumption by 34.48% and maximum operating temperature by 28.45% when 2 V input voltage is applied. In order to analyze the effect of increase thermal mass, the model is compared with the FEM simulation results and is in close agreement, with a maximum error of 3.2% and 8% in transient response and power calculations, respectively. With 8 μm thick nitride layer, the time constant has increased by 72.95%. The strip approximation used while developing an analytical steady state model, underestimate the membrane area. A triangular approach is suggested to accurately estimate the area of the membrane, and the membrane area error was within 0.8% which was better compared to strip or circular approaches.

A square microhotplate with S-shape microheater is fabricated using the membrane materials and dimensions from the simulation studies, and its performance was evaluated using a simple testing setup. Choosing gas sensing as an application area of microhotplate, a modeling approach for n-type nanowire transistor based gas sensor has been presented. In order to improve modeling accuracy, transistor equations were derived by taking width modulation and rectifying contact aspects into consideration. The surface depletion width in the presence of oxidizing gas is the cause which results in the sensing response. An equation for surface depletion width is derived and it relates the device and the effect of gas exposure on its characteristics. The obtained depletion width was used to find the surface band bending and surface potential. The model matches closely with the experimentally reported current characteristics of single ZnO nanowire FET. The presented modeling approach is simple and can be easily extended to other metal oxide transistors also.

6.1 Future Directions

Though, the review chapter discusses about the materials employed in the fabrication and their compatibility with the CMOS/MEMS, a detailed method of fabrication may

be taken up in future. The mathematical model which was developed for insulation layer optimization can also be used for the optimization of MHR, quick estimation of power consumption in microhotplates with varying membrane area and different material composition. The convection coefficient values reported in literature vary in a wide range because of their dependence on the microhotplate size, shape, temperature and flow conditions. Since the convection conditions are not very well defined (especially for rayleigh number <200 (Ra)) in the literature. Therefore, for the sake of simplicity, the thesis have assumed natural convection at some place. However, an experimental study and CFD analysis of microhotplate would help in determining the convection heat transfer coefficient.

For the characterization of fabricated microhotplates, Infrared (IR) imaging can be employed for extracting the thermal profile of the microhotplate. A high performance microhotplate can bring additional advantages if one considers the practical aspects and performance tradeoff during design stage. Hence, the thickness of membrane should be as low as possible and silicon layer in the composite membrane has to be completely avoided because of its very large thermal conductivity. However, thin membrane are very fragile, especially for the larger membrane dimensions. Hence, the membrane length has to be reduced. Because of which, heater or the active area dimensions also has to be reduced, to minimize the thermal loss to the membrane edges. However, the active area dimensions are bounded by the design and minimum lithography dimensions. Hence, if design permits, a lower thickness of membrane can be achieved by using a laser written mask. Moreover, by employing wire bonding method rather than silver epoxy contacts, the current carrying capability to the microhotplate can be increased. In addition, wire bonding will also reduces the contact resistance and will allow the microhotplate to operate at even higher temperatures. In gas sensor modeling, to make the model more versatile, the effect of competitive adsorption, relative humidity etc, can be included in future.

Bibliography

[1] "http://samlab.epfl.ch/page-102923-en.html."

[2] R. Phatthanakun, P. Deekla, W. Pummara, C. Sriphung, C. Pantong, and N. Chomnawang, "Design and fabrication of thin-film aluminum microheater and nickel temperature sensor," in *Nano/Micro Engineered and Molecular Systems (NEMS), 2012 7th IEEE International Conference on*, March 2012, pp. 112 –115.

[3] L. Ruiqi, J. Chandrappan, K. Vaidyanathan, and S. S. Win, "Silicon micro heater based tagging module and the biocompatible packaging for capsule endoscope," in *Electronic Components and Technology Conference (ECTC), 2011 IEEE 61st*, June 2011, pp. 1300 –1307.

[4] G. Velmathi, N. Ramshanker, and S. Mohan, "Design, Electro-Thermal simulation and geometrical optimization of double spiral shaped microheater on a suspended membrane for gas sensing," in *Proceedings of the 36th Annual Conference on IEEE Industrial Electronics Society*, Nov. 2010, pp. 1258 –1262.

[5] S. Lee, D. Dyer, and J. Gardner, "Design and optimisation of a high-temperature silicon micro-hotplate for nanoporous palladium pellistors," *Microelectronics Journal*, vol. 34, no. 2, pp. 115 – 126, 2003. [Online]. Available: http://www.sciencedirect.com/science/article/pii/S0026269202001532

[6] S. Astie, A. Gue, E. Scheid, L. Lescouzeres, and A. Cassagnes, "Optimization of an integrated SnO2 gas sensor using a FEM simulator," *Sens. Actuators A*, vol. 69, no. 3, pp. 205–211, 1998.

[7] O. Sidek, M. Ishak, M. Khalid, M. Abu Bakar, and M. Miskam, "Effect of heater geometry on the high temperature distribution on a MEMS micro-hotplate," pp. 100–104, 2011.

[8] G. Saxena and R. Paily, "Simulation study of power loss components in a microheater," in *Power and Energy in NERIST (ICPEN), 2012 1st International Conference on*, 2012, pp. 1–5.

[9] J. Courbat, D. Briand, and N. De Rooij, "Reliability improvement of suspended platinum-based micro-heating elements," *Sens. Actuators A*, vol. 142, no. 1, pp. 284–291, 2008.

[10] H. Arata, Y. Rondelez, H. Noji, and H. Fujita, "Temperature alternation by an on-chip microheater to reveal enzymatic activity of β-galactosidase at high temperatures," *Anal. Chem.*, vol. 77, no. 15, pp. 4810–4814, 2005.

[11] L. Lam, S. Sakakihara, K. Ishizuka, S. Takeuchi, H. Arata, H. Fujita, and H. Noji, "Loop-mediated isothermal amplification of a single DNA molecule in polyacrylamide gel-based microchamber," *Biomedical Microdevices*, vol. 10, no. 4, pp. 539–546, 2008.

[12] Y. W. Lai and J.-Y. Lee, "In situ study of thermal deformation of metal resistive heater on silicon nitride membrane by digital holographic microscopy," in *Nano/Micro Engineered and Molecular Systems (NEMS), 2012 7th IEEE International Conference on*, March 2012, pp. 557 –561.

[13] T. Iwaki, J. Covington, F. Udrea, S. Ali, P. Guha, and J. Gardner, "Design and simulation of resistive SOI CMOS micro-heaters for high temperature gas sensors," vol. 15, p. 27, 2005.

[14] L. Xu, T. Li, and Y. Wang, "A novel three-dimensional microheater," *Electron Device Letters, IEEE*, vol. 32, no. 9, pp. 1284–1286, 2011.

[15] L. Mele, F. Santagata, E. Iervolino, M. Mihailovic, T. Rossi, A. Tran, H. Schellevis, J. Creemer, and P. Sarro, "A molybdenum MEMS microhotplate for high-temperature operation," *Sens. Actuators A*, vol. 188, no. 0, pp. 173 – 180, 2012. [Online]. Available: http://www.sciencedirect.com/science/article/pii/S0924424711006820

[16] L. Xu, T. Li, X. Gao, and Y. Wang, "Development of a reliable micro-hotplate with low power consumption," *Sensors Journal, IEEE*, vol. 11, no. 4, pp. 913 –919, April 2011.

[17] M. Baroncini, P. Placidi, A. Scorzoni, G. Cardinali, L. Dori, and S. Nicoletti, "Characterization of an embedded micro-heater for gas sensors applications," in *Proceedings of the International Symposium on VLSI Technology, Systems, and Applications.* IEEE, 2001, pp. 164–167.

[18] K. Supan, H. Ingley, R. Pohle, and D. Hahn, "A kinetic model for ammonia adsorption on a titanium nitride surface," *Sensors Journal, IEEE*, vol. 12, no. 5, pp. 843–848, May 2012.

[19] Z. Fan and J. G. Lu, "Gate-refreshable nanowire chemical sensors," *Appl. Phys.Lett.*, vol. 86, pp. 123 510–123 512, 2006.

[20] D. Kim, Y. Jung, M. Park, B. Kim, S. Hong, M. Choi, M. Kang, Y. Yu, D. Whang, and S. Hwang, "Electrical Characteristics of the Backgated Bottom-Up Silicon Nanowire FETs," *Nanotechnology, IEEE Transactions on*, vol. 7, no. 6, pp. 683–687, Nov 2008.

[21] "coventor.com," http://www.coventor.com/mems-solutions/products/coventorware/, 2013, [Online]. [April-2013].

[22] S.-J. Young, L.-W. Ji, S.-J. Chang, Y. Chen, and S. Peng, "Zno schottky diodes with iridium contact electrodes," *Semiconductor Science and Technology*, vol. 23, no. 8, p. 085016, 2008.

[23] Z. Y. Fan, D. W. Wang , P. C. Chang, W. Y. Tseng, J. G. Lu, "Zno nanowire field-effect transistor and oxygen sensing property," *Applied Physics Letters*, vol. 85, pp. 5923–5925, 2004.

[24] J. Guerin, M. Bendahan, and K. Aguir, "A dynamic response model for the WO3 based ozone sensors," *Sensors and Actuators B: Chemical*, vol. 128, no. 2, pp. 462–467, 2008.

[25] A. Rothschild, Y. Komem, and N. Ashkenasy, "Quantitative evaluation of chemisorption processes on semiconductors," *Journal of Applied Physics*, vol. 92, no. 12, pp. 7090–7097, 2002. [Online]. Available: http://link.aip.org/link/?JAP/92/7090/1

[26] J.-H. Yoon, B.-J. Kim, and J.-S. Kim, "Design and fabrication of micro hydrogen gas sensors using palladium thin film," *Mater. Chem. Phys.*, vol. 133, no. 2-3, pp. 987 – 991, 2012. [Online]. Available: http://www.sciencedirect.com/science/article/pii/S0254058412001551

[27] P. Ho and T. Kwok, "Electromigration in metals," *Rep. Prog. Phys.*, vol. 52, no. 3, pp. 301–348, 1989.

[28] F. Naumann, M. Ebert, J. Hildenbrand, E. Moretton, C. Peter, and J. Wollenstein, "Thermal and mechanical design optimisation of a micro machined mid-infrared emitter for optical gas sensing systems," in *Proceedings of the 10th International Conference on Thermal, Mechanical and Multi-Physics simulation and Experiments in Microelectronics and Microsystems*. IEEE, 2009, pp. 1–5.

[29] S. Mendoza-Acevedo and M. Reyes-Barranca, "Study for the micromachining optimization of micro hotplates used in MEMS-CMOS gas sensors," in *Proceedings of the 8th International Conference on Electrical Engineering Computing Science and Automatic Control (CCE)*. IEEE, 2011, pp. 1–6.

[30] J. Lee, C. M. Spadaccini, E. V. Mukerjee, W. P. King, "Suspended Membrane Single Crystal Silicon Micro Hotplate for Differential Scanning Calorimetry," in *Proceedings of the 22nd International Conference on Micro Electro Mechanical Systems*. IEEE, 2009, pp. 852–855.

[31] M. Afridi, J. Suehle, M. Zaghloul, D. Berning, A. Hefner, R. Cavicchi, S. Semancik, C. Montgomery, and C. Taylor, "A monolithic cmos microhotplate-based gas sensor system," *Sensors Journal, IEEE*, vol. 2, no. 6, pp. 644–655, Dec 2002.

[32] J. Kim, J. Chung, D. Lee, Y. Kim, J. Kim, S. Hwang, B. Ju, S. Yun, and H. Park, "Development of temperature feedback control system for piezo-actuated display package," *Sens. Actuators A*, vol. 151, no. 2, pp. 213–219, 2009.

[33] D. Briand, P. Pham, and N. De Rooij, "Reliability of freestanding polysilicon microheaters to be used as igniters in solid propellant microthrusters," *Sens. Actuators A*, vol. 135, no. 2, pp. 329–336, 2007.

[34] D. Yoon, Y.-K. Cho, K. Oh, S. Kim, Y. Kim, J. Han, and G. Lim, "A microfluidic gel valve device using reversible sol-gel transition of methyl cellulose for biomedical application," *Microsystem Technologies*, vol. 12, pp. 238–246, 2006.

[35] K. Visvanathan and Y. Gianchandani, "Microheaters based on ultrasonic actuation of piezoceramic elements," *Journal of Micromechanics and Microengineering*, vol. 21, p. 085030, 2011.

[36] A. Javed, S. M. Iqbal, and A. Jain, "Microheater platform for selective detachment of DNA," *Appl. Phys. Lett.*, vol. 101, no. 9, p. 093707, 2012. [Online]. Available: http://link.aip.org/link/?APL/101/093707/1

[37] A. Atabaki, E. Shah Hosseini, A. Eftekhar, S. Yegnanarayanan, and A. Adibi, "Optimization of metallic microheaters for high-speed reconfigurable silicon photonics," *Optics express*, vol. 18, no. 17, pp. 18 312–18 323, 2010.

[38] F. Niklaus, C. Vieider, and H. Jakobsen, "MEMS-based uncooled infrared bolometer arrays: a review," *Proc. SPIE*, vol. 6836, pp. 68 360D–68 360D–15, 2007. [Online]. Available: http://dx.doi.org/10.1117/12.755128

[39] I. Simon, N. Barsan, M. Bauer, and U. Weimar, "Micromachined metal oxide gas sensors: opportunities to improve sensor performance," *Sensors and Actuators B: Chemical*, vol. 73, no. 1, pp. 1 – 26, 2001. [Online]. Available: http://www.sciencedirect.com/science/article/pii/S0925400500006390

[40] E. Comini, G. Faglia, and G. Sberveglieri, *Solid state gas sensing*. Springer, 2009, vol. 20.

[41] N. Nguyen, "Micromachined flow sensors–a review," *Flow measurement and Instrumentation*, vol. 8, no. 1, pp. 7–16, 1997.

[42] H. San, C. Li, X. Chen, R. Chen, and Q. Zhang, "Silicon-Based Micro-Machined Infrared Emitters With a Micro-Bridge and a Self-Heating Membrane Structure," *Photonics Technology Letters, IEEE*, vol. 25, no. 11, pp. 1014–1016, 2013.

[43] J. Hildenbrand, J. Korvink, J. Wollenstein, C. Peter, A. Kurzinger, F. Naumann, M. Ebert, and F. Lamprecht, "Micromachined mid-infrared emitter for fast transient temperature operation for optical gas sensing systems," *Sensors Journal, IEEE*, vol. 10, no. 2, pp. 353–362, 2010.

[44] L. A. S. Lai, "MEMS-based scanning calorimeter for thermodynamic properties of nanostructures," *Microscale Thermophysical Engineering*, vol. 2, no. 1, pp. 11–19, 1998.

[45] K. D. Hurley, B. G. Frederick, W. J. DeSisto, A. R. van Heiningen, and M. C. Wheeler, "Catalytic reaction characterization using micromachined nanocalorimeters," *Applied Catalysis A: General*, vol. 390, no. 1-2, pp. 84 – 93, 2010. [Online]. Available: http://www.sciencedirect.com/science/article/pii/S0926860X10006897

[46] U. Dillner, E. Kessler, and H.-G. Meyer, "Figures of merit of thermoelectric and bolometric thermal radiation sensors," *Journal of Sensors and Sensor Systems*, vol. 2, no. 1, pp. 85–94, 2013. [Online]. Available: http://www.j-sens-sens-syst.net//2/85/2013/

[47] F. Forsberg, N. Roxhed, A. C. Fischer, B. Samel, P. Ericsson, N. Hoivik, A. Lapadatu, M. Bring, G. Kittilsland, G. Stemme, and F. Niklaus, "Very large scale heterogeneous integration (VLSHI) and wafer-level vacuum packaging for infrared bolometer focal plane arrays ," *Infrared Physics & Technology*, vol. 60, no. 0, pp. 251 – 259, 2013. [Online]. Available: http://www.sciencedirect.com/science/article/pii/S1350449513001084

[48] C. Tao, C. Yin, M. He, and S. Tu, "Thermal analysis and design of a micro-hotplate for Si-substrated micro-structural gas sensor," in *Nano/Micro Engineered and Molecular Systems, 2008. NEMS 2008. 3rd IEEE International Conference on.* IEEE, 2008, pp. 284–287.

[49] C. Tsamis, A. Nassiopoulou, and A. Tserepi, "Thermal properties of suspended porous silicon micro-hotplates for sensor applications," *Sens. Actuators B*, vol. 95, no. 1-3, pp. 78 – 82, 2003. [Online]. Available: http://www.sciencedirect.com/science/article/pii/S092540050300409X

[50] D. Tengeri, A. Pullmannova, I. Hotovy, V. Rehacek, S. Hascik, and T. Lalinsky, "Preparation and properties of micro-hotplates for gas sensors based on GaAs," in *Advanced Semiconductor Devices and Microsystems, 2008. ASDAM 2008. International Conference on.* IEEE, 2008, pp. 323–326.

[51] S. Ghosh, S. Chatterjee, A. Kundu, S. Maity, and H. Saha, "Thermal analysis of cantilever MEMS based Low power microheater array for the selective detection of explosive and toxic gases," in *Physics and Technology of Sensors (ISPTS), 2012 1st International Symposium on*, March 2012, pp. 290 –293.

[52] J. Courbat, M. Canonica, D. Briand, N. de Rooij, D. Teyssieux, L. Thiery, and B. Cretin, "Thermal simulation and characterization for the design of ultra-low power micro-hotplates on flexible substrate," in *Proceedings of the IEEE Sensors.* IEEE, 2008, pp. 74–77.

[53] H. Lee, S. Moon, S. Park, J. Lee, K. Park, and J. Kim, "Micro-machined resistive micro-heaters for high temperature gas sensing applications," *Electronics Letters*, vol. 44, no. 25, pp. 1460–1461, 2008.

[54] J. Lee, H. Lee, S. Moon, J. Kwak, S. Park, J. Park, K. Park, and J. Kim, "Fabrication and characterization of surface-micromachined compact microheater for gas sensing applications," in *Nanotechnology, 2008. NANO'08. 8th IEEE Conference on.* IEEE, 2008, pp. 476–479.

[55] A. Gao, T. Li, and X. Liu, "Study of droplets motion on a chip driven by thermal gradient," in *Nano/Micro Engineered and Molecular Systems (NEMS), 2011 IEEE International Conference on*, Feb. 2011, pp. 241 –244.

[56] L. Mele, T. Rossi, M. Riccio, E. Iervolino, F. Santagata, A. Irace, G. Breglio, J. Creemer, and P. Sarro, "Electro-thermal analysis of MEMS microhotplates for the optimization of temperature uniformity," *Procedia Engineering*, vol. 25, no. 0, pp. 387 – 390, 2011. [Online]. Available: http://www.sciencedirect.com/science/article/pii/S1877705811057651

[57] U. Khan and C. Falconi, "Micro-hot-plates without simply connected hot-spots and with almost-circular temperature distribution," *Sensors and Actuators B: Chemical*, vol. 185, no. 0, pp. 274 – 281, 2013. [Online]. Available: http://www.sciencedirect.com/science/article/pii/S092540051300539X

[58] P. Hille and H. Strack, "A heated membrane for a capacitive gas sensor," *Sens. Actuators A*, vol. 32, no. 1-3, pp. 321 – 325, 1992. [Online]. Available: http://www.sciencedirect.com/science/article/pii/092442479280006O

[59] S. Ali, P. Guha, C. Lee, F. Udrea, W. Milne, T. Iwaki, J. Covington, and J. Gardner, "High Temperature SOI CMOS Tungsten Micro-Heaters," in *Sensors, 2006. 5th IEEE Conference on*, Oct. 2006, pp. 847 –850.

[60] U. Khan and C. Falconi, "Temperature distribution in membrane-type micro-hot-plates with circular geometry," *Sens. Actuators B*, vol. 177, no. 0, pp. 535 – 542, 2013. [Online]. Available: http://www.sciencedirect.com/science/article/pii/S0925400512011860

[61] J. Laconte, C. Dupont, D. Flandre, and J.-P. Raskin, "SOI CMOS compatible low-power microheater optimization for the fabrication of smart gas sensors," *Sensors Journal, IEEE*, vol. 4, no. 5, pp. 670 – 680, Oct. 2004.

[62] N. Najafi, K. Wise, R. Mechant, and J. Schwank, "An integrated multi-element ultra-thin-film gas analyzer," in *Solid-State Sensor and Actuator Workshop, 1992. 5th Technical Digest., IEEE*, Jun 1992, pp. 19 –22.

[63] J. Suehle, R. Cavicchi, M. Gaitan, and S. Semancik, "Tin oxide gas sensor fabricated using CMOS micro-hotplates and in-situ processing," *Electron Device Letters, IEEE*, vol. 14, no. 3, pp. 118 –120, March 1993.

[64] J. Creemer, W. van der Vlist, C. de Boer, H. Zandbergen, P. Sarro, D. Briand, and N. de Rooij, "MEMS hotplates with TiN as a heater material," in *Sensors, 2005 IEEE*, Nov. 2005, p. 4.

[65] S. Ali, F. Udrea, W. Milne, and J. Gardner, "Tungsten-Based SOI Microhotplates for Smart Gas Sensors," *Microelectromechanical Systems, Journal of*, vol. 17, no. 6, pp. 1408 –1417, Dec. 2008.

[66] S. Ali, W. Gonzalez, J. Gardner, and F. Udrea, "Analysis of high temperature SOI micro-hotplates," in *Semiconductor Conference, 2004. CAS 2004 Proceedings. 2004 International*, vol. 2, Oct. 2004, pp. 351 – 354.

[67] F. Solzbacher, C. Imawan, H. Steffes, E. Obermeier, and H. Moller, "A modular system of SiC-based microhotplates for the application in metal oxide gas sensors," *Sens. Actuators B*, vol. 64, no. 1-3, pp. 95 – 101, 2000. [Online]. Available: http://www.sciencedirect.com/science/article/pii/S0925400599004906

[68] G.-S. Chung and J.-M. Jeong, "Fabrication of micro heaters on polycrystalline 3C-SiC suspended membranes for gas sensors and their characteristics," *Microelectron. Eng.*, vol. 87, no. 11, pp. 2348 – 2352, 2010. [Online]. Available: http://www.sciencedirect.com/science/article/pii/S0167931710001309

[69] S. Firebaugh, K. Jensen, and M. Schmidt, "Investigation of high-temperature degradation of platinum thin films with an in situ resistance measurement apparatus," *Microelectromechanical Systems, Journal of*, vol. 7, no. 1, pp. 128–135, 1998.

[70] J. Chaston, "Reactions of oxygen with the platinum metals," *Platin Met Rev*, vol. 9, no. 2, pp. 51–56, 1965.

[71] R. Tiggelaar, "Silicon-technology based microreactors for high-temperature heterogeneous partial oxidation reactions." Wöhrmann Print Service, Zutphen, 2004.

[72] R. Tiggelaar, R. Sanders, A. Groenland, and J. Gardeniers, "Stability of Thin Platinum Films Implemented in High Temperature Microdevices," *Sens. Actuators A*, vol. 152, no. 1, pp. 39 – 47, 2009. [Online]. Available: http://www.sciencedirect.com/science/article/pii/S0924424709001551

[73] L. Mele, F. Santagata, E. Iervolino, M. Mihailovic, T. Rossi, A. Tran, H. Schellevis, J. Creemer, and P. Sarro, "Sputtered molybdenum as conductive material for high-temperature microhotplates," in *Solid-State Sensors, Actuators and Microsystems Conference (TRANSDUCERS), 2011 16th International*, June 2011, pp. 2690 – 2693.

[74] O. Kubaschewski and B. Hopkins, "Oxidation mechanisms of niobium, tantalum, molybdenum and tungsten," *Journal of the Less Common Metals*, vol. 2, no. 2-4, pp. 172–180, 1960. [Online]. Available: http://www.sciencedirect.com/science/article/pii/0022508860900126

[75] M. Ehmann, P. Ruther, M. von Arx, and O. Paul, "Operation and short-term drift of polysilicon-heated CMOS microstructures at temperatures up to 1200 K," *Journal of micromechanics and microengineering*, vol. 11, no. 4, p. 397, 2001.

[76] O. Grudin, R. Marinescu, L. Landsberger, D. Cheeke, and M. Kahrizi, "Microstructure release and test techniques for high-temperature micro hotplate," in *Electrical and Computer Engineering, 1999 IEEE Canadian Conference on*, vol. 3, May 1999, pp. 1610 –1615.

[77] M. Mihailovic, "MEMS monocrystalline-silicon based thermal devices for chemical and microfluidic applications," Ph.D. dissertation, Delft University of Technology, Microelectronics & Computer Engineering Department, June 2011.

[78] M. Mihailovic, J. F. Creemer, and P. M. Sarro, "Monocrystalline silicon microhotplate heater," in *EUROSENSORS XXII*, 2008, pp. 1611–1614.

[79] T. Iwaki, J. Covington, J. Gardner, F. Udrea, C. Blackman, and I. Parkin, "SOI-CMOS based single crystal silicon micro-heaters for gas sensors," in *Proceedings of the 5th IEEE Conference on Sensors*. IEEE, 2006, pp. 460–463.

[80] J. Spannhake, O. Schulz, A. Helwig, A. Krenkow, G. Muller, and T. Doll, "High-temperature MEMS Heater Platforms: Long-term Performance of Metal and Semiconductor Heater Materials," *Sensors*, vol. 6, no. 4, pp. 405–419, 2006. [Online]. Available: http://www.mdpi.com/1424-8220/6/4/405

[81] D. Briand, S. Colin, J. Courbat, S. Raible, J. Kappler, and N. de Rooij, "Integration of MOX gas sensors on polyimide hotplates," *Sens. Actuators B*, vol. 130, no. 1, pp. 430 – 435, 2008. [Online]. Available: http://www.sciencedirect.com/science/article/pii/S0925400507007204

[82] C. Rossi, P. Temple-Boyer, and D. Estève, "Realization and performance of thin SiO2/SiNx membrane for microheater applications," *Sens. Actuators A*, vol. 64, no. 3, pp. 241 – 245, 1998. [Online]. Available: http://www.sciencedirect.com/science/article/pii/S0924424797016270

[83] N. Swart and A. Nathan, "Design optimisation of integrated microhotplates," *Sens. Actuators A*, vol. 43, no. 1-3, pp. 3–10, 1994.

[84] D. Briand, "Thermally isolated microelectronic devices for gas sensing applications," Ph.D. dissertation, University of Neuchâtel, 2001.

[85] A. Pike and J. W. Gardner, "Thermal modelling and characterisation of micropower chemoresistive silicon sensors," *Sens. Actuators B*, vol. 45, no. 1, pp. 19 – 26, 1997.

[86] Y. Mo, Y. Okawa, K. Inoue, and K. Natukawa, "Low-voltage and low-power optimization of micro-heater and its on-chip drive circuitry for gas sensor array," *Sens. Actuators A*, vol. 100, no. 1, pp. 94 – 101, 2002. [Online]. Available: http://www.sciencedirect.com/science/article/pii/S0924424702001450

[87] B. Tang and K. Sato, *Microelectromechanical Systems and Devices*, N. Islam, Ed. InTech, 2012.

[88] P. Pal, K. Sato, M. Gosalvez, and M. Shikida, "An improved anisotropic wet etching process for the fabrication of silicon MEMS structures using a single etching mask," in *Micro Electro Mechanical Systems, 2008. MEMS 2008. IEEE 21st International Conference on*, 2008, pp. 327–330.

[89] D. Briand, S. Colin, A. Gangadharaiah, E. Vela, P. Dubois, L. Thiery, and N. de Rooij, "Micro-hotplates on polyimide for sensors and actuators," *Sens. Actuators A*, vol. 132, no. 1, pp. 317 – 324, 2006. [Online]. Available: http://www.sciencedirect.com/science/article/pii/S0924424706003992

[90] C. Tsamis, A. Tserepi, and A. Nassiopoulou, "Fabrication of suspended porous silicon micro-hotplates for thermal sensor applications," *physica status solidi (a)*, vol. 197, no. 2, pp. 539–543, 2003.

[91] F. Solzbacher, C. Imawan, H. Steffes, E. Obermeier, and M. Eickhoff, "A new SiC/HfB2 based low power gas sensor," *Sens. Actuators B*, vol. 77, no. 1-2, pp. 111–115, 2001.

[92] A. Vasiliev, R. Pavelko, S. Y. Gogish-Klushin, D. Y. Kharitonov, O. Gogish-Klushina, A. Sokolov, A. Pisliakov, and N. Samotaev, "Alumina MEMS platform for impulse semiconductor and IR optic gas sensors," *Sensors and Actuators B: Chemical*, vol. 132, no. 1, pp. 216 – 223, 2008. [Online]. Available: http://www.sciencedirect.com/science/article/pii/S0925400508000671

[93] J. Kita, F. Rettig, R. Moos, K.-H. Drüe, and H. Thust, "Hot plate gas sensors-are ceramics better?" *Int. J. Appl. Ceram. Technol.*, vol. 2, no. 5, pp. 383–389, 2005. [Online]. Available: http://dx.doi.org/10.1111/j.1744-7402.2005.02037.x

[94] C. Patel, A. Jadhav, S. Lone, V. Rane, V. Chaware, V. Giramkar, and G. Phatak, "Miniaturization of LTCC based hot plates for gas sensors application," in *Physics and Technology of Sensors (ISPTS), 2012 1st International Symposium on*, 2012, pp. 83–86.

[95] F. Udrea and J. W. Gardner, "Design of a silicon microsensor array device for gas analysis," *Microelectronics Journal*, vol. 27, no. 6, pp. 449 – 457, 1996. [Online]. Available: http://www.sciencedirect.com/science/article/pii/0026269295001123

[96] A. Kozlov and D. Randjelovic, "Modelling of temperature distribution in thermal microsensors on sandwich thermally isolated structures," in *Thermal, Mechanical and Multi-Physics Simulation and Experiments in Microelectronics and Microsystems (EuroSimE), 2012 13th International Conference on*, April 2012, pp. 1/5 –5/5.

[97] M. Aslam, C. Gregory, and J. Hatfield, "Polyimide membrane for micro-heated gas sensor array," *Sensors and Actuators B: Chemical*, vol. 103, no. 1-2, pp. 153 – 157, 2004. [Online]. Available: http://www.sciencedirect.com/science/article/pii/S0925400504002278

[98] P. Maccagnani, R. Angelucci, P. Pozzi, A. Poggi, L. Dori, G. Cardinali, and P. Negrini, "Thick oxidized porous silicon layer as thermo-insulating material for high temperature operating thin and thick film gas sensors," in *Solid State Sensors and Actuators, 1997. TRANSDUCERS '97 Chicago., 1997 International Conference on*, vol. 1, Jun 1997, pp. 213 –216.

[99] R. Triantafyllopoulou, X. Illa, O. Casals, S. Chatzandroulis, C. Tsamis, A. Romano-Rodriguez, and J. Morante, "Nanostructured oxides on porous silicon microhotplates for NH3 sensing," *Microelectron. Eng.*, vol. 85, no. 5-6, pp. 1116 – 1119, 2008. [Online]. Available: http://www.sciencedirect.com/science/article/pii/S0167931707008234

[100] R. Triantafyllopoulou, C. Tsamis, S. Chatzandroulis, T. Speliotis, J. Parthenios, K. Papagelis, and C. Galiotis, "Thermal characterization of porous silicon microhotplates using ir thermography," in *Solid-State Sensors, Actuators and Microsystems Conference, 2007. TRANSDUCERS 2007. International*. IEEE, 2007, pp. 2271–2274.

[101] D. Papadimitriou, C. Tsamis, and A. Nassiopoulou, "The influence of thermal treatment on the stress characteristics of suspended porous silicon membranes on silicon," *Sens. Actuators B*, vol. 103, no. 1-2, pp. 356 – 361, 2004. [Online]. Available: http://www.sciencedirect.com/science/article/pii/S0925400504002576

[102] P. Maccagnani, R. Angelucci, P. Pozzi, A. Poggi, L. Dori, G. Cardinali, and P. Negrini, "Thick oxidised porous silicon layer as a thermo-insulating membrane for high-temperature operating thin- and thick-film gas sensors," *Sens. Actuators B*, vol. 49, no. 1-2, pp. 22 – 29, 1998. [Online]. Available: http://www.sciencedirect.com/science/article/pii/S0925400597003377

[103] F. Solzbacher, C. Imawan, H. Steffes, E. Obermeier, and M. Eickhoff, "A highly stable SiC based microhotplate NO2 gas-sensor," *Sens. Actuators B*, vol. 78, no. 1-3, pp. 216 – 220, 2001. [Online]. Available: http://www.sciencedirect.com/science/article/pii/S0925400501008152

[104] G. Saxena and R. Paily, "Effect of membrane to heater ratio on the performance of square microhotplate," in *Emerging Research Areas and 2013 International Conference on Microelectronics, Communications and Renewable Energy (AICERA/ICMiCR), 2013 Annual International Conference on*, 2013, pp. 1–5.

[105] A. Götz, I. Gràcia, C. Cané, and E. Lora-Tamayo, "Thermal and mechanical aspects for designing micromachined low-power gas sensors," *Journal of Micromechanics and Microengineering*, vol. 7, p. 247, 1997.

[106] J. Dennis, A. Ahmed, and N. Mohamad, "Design, simulation and modeling of a micromachined high temperature microhotplate for application in trace gas detection," *International Journal of Engineering and Technology*, vol. 10, no. 02, pp. 89–96, 2010.

[107] G. Saxena and R. Paily, "Choice of insulation materials and its effect on the performance of square microhotplate," *Microsystem Technologies*, pp. 1–7, 2013. [Online]. Available: http://dx.doi.org/10.1007/s00542-013-2022-6

[108] T. Neda, K. Nakamura, and T. Takumi, "A polysilicon flow sensor for gas flowmeters," in *Solid-State Sensors and Actuators, 1995 and Eurosensors IX.. Transducers '95. The 8th International Conference on*, vol. 1, Jun 1995, pp. 548 –551.

[109] G. Saxena and R. Paily, "Analytical modeling of square microhotplate for gas sensing application," *Sensors Journal, IEEE*, vol. 13, no. 12, pp. 4851–4859, 2013.

[110] ——, "Transient analysis of bridge microhotplate," in *Advanced Electronic Systems (ICAES), 2013 International Conference on*, Sept 2013, pp. 328–330.

[111] D. G. Cahill, K. Goodson, and A. Majumdar, "Thermometry and thermal transport in micro/nanoscale solid-state devices and structures," *Journal of Heat Transfer*, vol. 124, no. 2, pp. 223–241, 2002. [Online]. Available: http://link.aip.org/link/?JHR/124/223/1

[112] M. Z. Ansari and C. Cho, "A conduction-convection model for self-heating in piezoresistive microcantilever biosensors," *Sens. Actuators A*, vol. 175, no. 0, pp. 19 – 27, 2012. [Online]. Available: http://www.sciencedirect.com/science/article/pii/S0924424711007126

[113] X. J. Hu, A. Jain, and K. E. Goodson, "Investigation of the natural convection boundary condition in microfabricated structures," *International Journal of Thermal Sciences*, vol. 47, no. 7, pp. 820 – 824, 2008. [Online]. Available: http://www.sciencedirect.com/science/article/pii/S1290072907001731

[114] W. Johnston and G. Lindberg, "Stability and calibration of miniature platinum resistance thermometers," *Rev. Sci. Instrum.*, no. 12, pp. 1925–1928, 1968.

[115] http://spectra.phy.bris.ac.uk/facilities_Infrascope.asp, 2013, [August-2013].

[116] http://samlab.epfl.ch/page-15536-en.html, 2011, [August-2013].

[117] B. D. Boudreau, J. Raja, R. J. Hocken, S. R. Patterson, and J. Patten, "Thermal imaging with near-field microscopy," *Review of Scientific Instruments*, vol. 68, no. 8, pp. 3096–3098, 1997. [Online]. Available: http://link.aip.org/link/?RSI/68/3096/1

[118] M. A. Cahill DG, Goodson K, "Thermometry and thermal transport in micro/-nanoscale solid-state devices and structures," *J. Heat Transfer.*, vol. 124(2), pp. 223–241, 2001.

[119] A. Helwig, J. Spannhake, G. Muller, N. Rosman, and T. Pagnier, "Temperature characterization of silicon substrates for gas sensors by Raman spectroscopy ," *Sensors and Actuators B: Chemical*, vol. 126, no. 1, pp. 240 – 244, 2007. [Online]. Available: http://www.sciencedirect.com/science/article/pii/S0925400506008070

[120] Y. Lai, N. Koukourakis, N. Gerhardt, M. Hofmann, R. Meyer, S. Hamann, M. Ehmann, K. Hackl, E. Darakis, and A. Ludwig, "Integrity of micro-hotplates during high-temperature operation monitored by digital holographic microscopy," *Microelectromechanical Systems, Journal of*, vol. 19, no. 5, pp. 1175 –1179, Oct. 2010.

[121] M. Baroncini, P. Placidi, G. Cardinali, and A. Scorzoni, "Thermal characterization of a microheater for micromachined gas sensors," *Sens. Actuators A*, vol. 115, no. 1, pp. 8–14, 2004.

[122] F. Rettig and R. Moos, "Ceramic meso hot-plates for gas sensors," *Sensors and Actuators B: Chemical*, vol. 103, no. 1-2, pp. 91– 97, 2004. [Online]. Available: http://www.sciencedirect.com/science/article/pii/S0925400504002175

[123] D. Briand, S. Heimgartner, M. Grétillat, B. Schoot, and N. Rooij, "Thermal optimization of micro-hotplates that have a silicon island," *Journal of Micromechanics and Microengineering*, vol. 12, p. 971, 2002.

[124] N. Ravindra, S. Abedrabbo, W. Chen, F. Tong, A. Nanda, and A. Speranza, "Temperature-dependent emissivity of silicon-related materials and structures," *Semiconductor Manufacturing, IEEE Transactions on*, vol. 11, no. 1, pp. 30–39, 1998.

[125] T. Li, L. Wu, Y. Liu, L. Wang, Y. Wang, and Y. Wang, "Micro-heater on membrane with large uniform-temperature area," in *Sensors, 2006. 5th IEEE Conference on*, Oct. 2006, pp. 571–575.

[126] F. Solzbacher, "A new sic/hfb2 based micro hotplate for metal oxide gassensors," Ph.D. dissertation, 2003.

[127] C. Yang, F. Mess, K. Skenes, S. Melkote, and S. Danyluk, "On the residual stress and fracture strength of crystalline silicon wafers," *Appl. Phys. Lett.*, vol. 102, no. 2, pp. 021 909–021 909, 2013.

[128] E. Comini, C. Baratto, I. Concina, G. Faglia, M. Falasconi, M. Ferroni, V. Galstyan, E. Gobbi, A. Ponzoni, A. Vomiero, D. Zappa, V. Sberveglieri, and G. Sberveglieri, "Metal oxide nanoscience and nanotechnology for chemical sensors," *Sensors and Actuators B: Chemical*, vol. 179, no. 0, pp. 3 – 20, 2013, a Special Issue in Honour of Professor A. D'Amico. [Online]. Available: http://www.sciencedirect.com/science/article/pii/S0925400512010519

[129] J. Xiao, P. Liu, Y. Liang, H. B. Li, and G. W. Yang, "High aspect ratio beta-MnO2 nanowires and sensor performance for explosive gases," *Journal of Applied Physics*, vol. 114, no. 7, 2013. [Online]. Available: http://scitation.aip.org/content/aip/journal/jap/114/7/10.1063/1.4819218

[130] N. Van Hieu, P. Thi Hong Van, L. Tien Nhan, N. Van Duy, and N. Duc Hoa, "Giant enhancement of H2S gas response by decorating n-type SnO2 nanowires with p-type NiO nanoparticles," *Applied Physics Letters*, vol. 101, no. 25, 2012. [Online]. Available: http://scitation.aip.org/content/aip/journal/apl/101/25/10.1063/1.4772488

[131] A. Soares and R. Perry, "Modeling and simulation of a single tin dioxide nanobelt fet for chemical sensors," *Sensors Journal, IEEE*, vol. 10, no. 2, pp. 235 –242, Feb. 2010.

[132] A. Rothschild and Y. Komem, "Numerical computation of chemisorption isotherms for device modeling of semiconductor gas sensors," *Sensors and Actuators B: Chemical*, vol. 93, no. 1-3, pp. 362–369, 2003.

[133] Y. Zhang, A. Kolmakov, Y. Lilach, and M. Moskovits, "Electronic control of chemistry and catalysis at the surface of an individual tin oxide nanowire," *The Journal of Physical Chemistry B*, vol. 109, no. 5, pp. 1923–1929, 2005.

[134] R. Gautam, M. Saxena, R. Gupta, and M. Gupta, "Gate-all-around nanowire mosfet with catalytic metal gate for gas sensing applications," *Nanotechnology, IEEE Transactions on*, vol. 12, no. 6, pp. 939–944, Nov 2013.

[135] P. Andrei, L. Fields, J. Zheng, Y. Cheng, and P. Xiong, "Modeling and simulation of single nanobelt SnO2 gas sensors with FET structure," *Sensors and Actuators B: Chemical*, vol. 128, no. 1, pp. 226 – 234, 2007. [Online]. Available: http://www.sciencedirect.com/science/article/pii/S0925400507004091

[136] B. G. Streetman and S. Banerjee, *Solid state electronic devices*. Prentice Hall Englewood Cliffs, NJ, 1995, vol. 4.

[137] H.-Y. Cha, H. Wu, M. Chandrashekhar, Y. Choi, S. Chae, G. Koley, and M. Spencer, "Fabrication and characterization of pre-aligned gallium nitride nanowire field-effect transistors," *Nanotechnology*, vol. 17, no. 5, p. 1264, 2006.

[138] Z. Y. Fan, J. G. Lu, "Chemical Sensing With ZnO Nanowire Field-Effect Transistor," *IEEE Transactions on Nanotechnology*, vol. 5, pp. 393–396, 2006.

List of Publications

National and International Conferences

- **G. Saxena** and R. Paily, "**Design of microhotplate with uniform thermal profile for gas sensing application**," ISSS National Conference on MEMS, Smart Materials, Structures and Systems September 2012.
- **G. Saxena** and R. Paily, "**Simulation study of power loss components in a micro-heater**," IEEE International Conference on Power and Energy in NERIST (ICPEN), pp. 1–5, 2012.
- **G. Saxena** and R. Paily, "**Effect of membrane to heater ratio on the performance of square microhotplate**," IEEE International Conference on Emerging Research Areas and International Conference on Microelectronics, Communications and Renewable Energy (AICERA/ICMiCR), pp. 1 –5 , 2013.
- **G. Saxena** and R. Paily, "**Transient analysis of bridge microhotplate**," IEEE International Conference on Advanced Electronic Systems (ICAES), 2013 , pp. 328–330, 2013.

International Journals

- **G. Saxena** and R. Paily, "**Analytical modeling of square microhotplate for gas sensing application**," Sensors Journal, IEEE, vol. 13, no. 12, pp. 4851–4859, 2013.
- **G. Saxena** and R. Paily, "**Choice of insulation materials and its effect on the performance of square microhotplate**," Microsystem Technologies, Springer, pp. 1 –7 , 2013.
- **G. Saxena** and R. Paily, "**Performance Improvement of Square Microhotplate with Insulation Layer and Heater Geometry**," Microsystem Technologies, Springer, pp. 1 –7 , 2014.
- **G. Saxena** and R. Paily, "**Analysis of nanowire transistor based nitrogen dioxide gas sensor –A simulation study**," Sensing and Bio–Sensing Research, Elsevier, vol. 4, pp. 57–60, 2015.

Manuscript Under Preparation

- **G. Saxena** and R. Paily, "**A Review of Microhotplates**," To be communicated
- **G. Saxena** and R. Paily, "**Performance of Square Microhotplate with Non-CMOS Membrane Materials**," To be communicated
- **G. Saxena** and R. Paily, "**Wide Bandgap Zinc Oxide Thin Films Prepared by RF Magnetron Sputtering at Room Temperature**," To be communicated
- **G. Saxena** and R. Paily, "**Modeling of Square Microhotplate and its Validation with Experimental Results**," To be communicated
- **G. Saxena** and R. Paily, "**Model for Selectivity and Sensitivity of Nanowire Transistor Based Gas Sensors**," To be communicated

Awards/Honor/Talks

- **Secured 1st position** in Techscribe-Technical Paper Presentation organized by Techniche-The Annual Techno-Management Festival , IIT Guwahati– 2013. Paper Title: Microhotplates Performance Improvement with Selective Deposition of Silicon Carbide Layer
- **Secured 2nd position** in M V Chauhan All India Student Paper Contest 2013. Paper Title: Design, Fabrication and Characterization of Square Microhotplate
- **Speaker** in TechEvince 1.0, annual research exhibition on the topic Design, Modeling and Fabrication of Gas Sensors organized at Indian Institute of Technology (Nov. 10, 2013). Guwahati.
- **Speaker** in IEEE workshop on Micro-Electro-Mechanical Systems (MEMS) and Very-Large-Scale Integration (VLSI) Digital Design Flow (February 8-9, 2014) at Indian Institute of Technology Guwahati.

Author's Biography

Gaurav Saxena received the B.Tech. degree in electronics and telecommunication engineering from Uttar Pradesh Technical University, Lucknow, India, in 2007, and the M.Tech. degree in VLSI design from the National Institute of Technology, Hamirpur, India, in 2009. He joined the Indian Institute of Technology Guwahati, Guwahati, India, for PhD program in 2009, in the Department of Electronics and Electrical Engineering. His research interests include the design, modeling and fabrication of organic and inorganic semiconductor device and thermal analysis of microhotplates for biological and chemical sensing.